

Nanostructured Apatites as Orthopedic Biomaterials

by

Edward Sun Ahn

M. S. Chemical Engineering Practice
Massachusetts Institute of Technology, 1997

B. S., Chemical Engineering
Stanford University, 1994

Submitted to the Department of Chemical Engineering in Partial Fulfillment
of the Requirements for the Degree of


Doctor of Philosophy in Chemical Engineering

at the

MASSACHUSETTS INSTITUTE OF TECHNOLOGY

June 2001

© Massachusetts Institute of Technology 2001. All rights reserved.



Author: _____

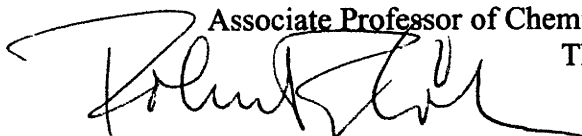
Department of Chemical Engineering
May 21, 2001

Certified by: _____

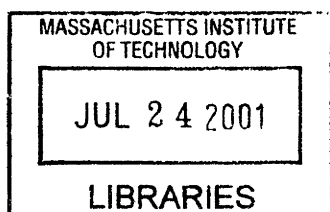


Professor Jackie Y. Ying
Associate Professor of Chemical Engineering
Thesis Supervisor

Accepted by: _____



Professor Robert E. Cohen
St. Laurent Professor of Chemical Engineering
Chairman, Committee for Graduate Studies



ARCHIVES

Nanostructured Apatites as Orthopedic Biomaterials

by

Edward Sun Ahn

M. S. Chemical Engineering Practice
Massachusetts Institute of Technology, 1997

B. S., Chemical Engineering
Stanford University, 1994

Submitted to the Department of Chemical Engineering
on May 2, 2001 in Partial Fulfillment of the Requirements for
the Degree of Doctor of Philosophy in Chemical Engineering

Abstract

Historically, using suitable mechanical replacements for bone has been a priority in designing permanent, load-bearing orthopedic implants. As a result, the biomaterials used in these implants have been largely limited to bioinert titanium-based alloys, as well as to polycrystalline alumina and zirconia ceramics. However, analysis of implants incorporating these traditional biomaterials indicated that most failures involved an unstable implant-tissue interface and/or a mismatch of the mechanical behavior of the implant with the surrounding tissues. As a result, up to 20% of patients receiving permanent, load-bearing implants may undergo a revision operation. The objective of this research was to develop an alternative biomaterial that combined both mechanical resilience and an osteoconductive surface to provide a stable interface with the surrounding connective tissue so that the need for revision operations may be significantly reduced.

In the effort to address the issue of mechanical strength and bioactivity simultaneously, hydroxyapatite (HAP) has generated considerable interest. Though a commonly used bioceramic, HAP has been limited by its processability. This material is sensitive to non-stoichiometry and impurities during synthesis and processing due to its complex composition and crystal structure ($\text{Ca}_{10}(\text{PO}_4)_6(\text{OH})_2$, $\text{P6}_3/\text{m}$). Consequently, conventionally processed HAP materials lack phase purity and homogeneity. Densification of HAP requires high temperatures that result in grain growth and decomposition into undesired phases with poor mechanical and chemical stability. To circumvent densification at high temperatures, glassy additives have been introduced to promote liquid-phase sintering at a lower temperature. However, the presence of a secondary glassy phase gave rise to poor mechanical characteristics. Hence, clinical applications of HAP have been limited to powders, coatings, porous bodies, and non-load-bearing implants.

To overcome the deficiencies of conventionally processed HAP, nanostructure processing was applied, which allowed for materials design from the molecular level. By using an aqueous chemical precipitation technique, a fully dense, transparent, nanostructured HAP-based bioceramic that exhibited superior mechanical properties and enhanced tissue bonding was obtained. Processing parameters affecting the molecular and structural development of HAP were used to tailor HAP stoichiometry, crystallite size, morphology and surface chemistry for

optimal thermal stability and sinterability. Unlike conventionally processed HAP, the stoichiometric, equiaxed, nanocrystalline HAP powders demonstrated significantly enhanced sinterability by fully densifying at a remarkably low temperature of 900°C with pressure-assisted sintering. Furthermore, high-resolution electron micrographs illustrated that the sintered compact possessed a uniform and ultrafine microstructure with an average grain size of ~100 nm, with no glassy or amorphous interfaces along the grain boundaries. The crystallinity of the HAP grains and grain boundaries and the minimal flaw sizes could be credited for the superior strength of nanostructured HAP compared to conventional HAP. Compared to polycrystalline HAP, nanocrystalline HAP also provided greater osteoblast function. *In vitro* experiments indicated that nanocrystalline HAP surfaces enhanced cell attachment, proliferation and mineralization. The larger grain boundary volume resulting from the ultrafine microstructure might have enhanced protein adsorption, improving the osteoblast's ability to bind to and interact with the nanocrystalline surface.

To further increase the fracture resistance of our HAP matrix against crack initiation and propagation, highly dispersed crystallites of zirconia were introduced into a HAP matrix using a colloidal addition technique. The resulting HAP-zirconia nanocomposites possessed an excellent bending strength of 240 MPa. With only 3 wt% zirconia addition, a high fracture toughness of 2.0 MPa·m^{1/2} was obtained with the HAP-based nanocomposite. Nanocomposite engineering was also developed for the HAP-silver system. Intimate mixing between the HAP and silver particles also yielded uniform, ultrafine microstructures with excellent mechanical properties.

The site and extent of substitution of carbonate ions into apatitic lattice were tailored by the nanostructure processing of synthetic carbonated apatites. Carbonated apatites are similar in composition to native bone mineral and are of interest as resorbable implant materials. By controlling synthesis conditions and the crystallinity of the system, the rate of resorption of carbonated apatites can be tuned.

Through nanostructure processing and nanocomposite engineering, HAP-based systems with significantly increased mechanical strength and bioactivity for implant applications have been developed. The nanocrystalline HAP, HAP-zirconia, HAP-silver and carbonated apatite systems investigated in this thesis may have potentially exciting applications as bone graft substitutes, intervertebral devices, internal fixation devices, and connective tissue attachments.

Thesis Supervisor: Jackie. Y. Ying

Title: Associate Professor of Chemical Engineering

Acknowledgments

I wish to thank Prof. Jackie Ying for being my advisor, mentor and friend. She was instrumental in my personal and professional development. I would also like to acknowledge the members of my thesis committee, Prof. Douglas Lauffenburger, Prof. Edward Merrill, and Prof. Myron Spector, for their advice and guidance over the course of my graduate studies. In particular, I would like to acknowledge Prof. Spector for opening the doors to his laboratory and teaching me biomaterials science.

I would also like to acknowledge my colleagues in the Nanostructured Materials Research Laboratory (NMRL) with whom I have thoroughly enjoyed working. I had the great pleasure of working with the first doctoral students of NMRL, Dr. Ken Bryden, Dr. Doron Levin, Dr. Darren Castro, and Dr. Lei Zhang, and I thank them for all their help. Next, I thank Dr. Michael Wong, Dr. Mark Fokema, and Dr. Larry Panchula for their friendship and support. I spent the most time with these people, and I look forward to continuing our lifetime friendship. I want to acknowledge the six MIT undergraduates who worked under my supervision, Wanwipa Siriawatwechakul, Nathaniel Gleason, Reginald Rogers, Jr., Eugene Chiu, Alice Choi, and Tamara Oei. They contributed greatly to my thesis work and were a joy to teach and to work with. I also thank the current members of NMRL for tolerating me with great humor and for creating a memorable environment to think, work, and live in for the past several years. Thank you, Dr. Tao Sun, Dr. Christian Mehnert, Dr. Jinsuo Xu, Dr. Dejian Huang, Ruma Chakravorty, John Lettow, Neeraj Sangar, Duane Myers, Jason Sweeney, Justin McCue, Suniti Moudgil, Yee Su, Steve Weiss, Tom Lancaster, Todd Zion, and Pemakorn Pitukmanorom.

I would like to thank Mike Frongillo for his friendship and for teaching me the ways of electron microscopy. I thank other staff members of the MIT CMSE, Dr. Tony Garratt-Reed, Libby Shaw, and Yin Lin Xie, as well as Nicki Watson of the Whitehead Institute for their expertise and assistance with various characterization techniques. I would like to thank Dr. Lou Gerstenfeld of Boston University for donating his cell line to initiate our cell culture studies and Dr. Xiuying Zhang and Sandra Taylor of the Brigham and Women's Hospital for being so generous with their knowledge and time. I thank Ellen Weene, Arline Benford, Joan Chisholm, and Carol Phillips for their support and friendship, and especially Linda Mousseau, for taking care of the group. I thank Janet Fischer and Elaine Aufiero for their help throughout my years in the Department, and Suzanne Easterly and Anne Fowler during the last few months prior to the conclusion of my thesis. Financial support from the Packard Foundation and the Office of Naval Research for my research is greatly appreciated.

For most of my graduate career, my wife, Angela, has been a central figure. She has always supported and encouraged me to be my best and struggled to balance my life. I thank her for all her love, support, and patience. Hee-Sook Chung, my mother-in-law, and Eric Chung, my brother-in-law, have also always been demonstrative in their love and support. Their constant kindness has made these past few years a wonderful experience. I dedicate this thesis to my wife and "Baby" Ahn. This thesis will always be a constant reminder of "Baby" Ahn. As Angela and I end this chapter of our lives, we are very eager to meet "Baby" Ahn and begin the next chapter.

Contents

| | |
|---|-----------|
| Chapter 1 – Research Motivation and Objectives | 12 |
| 1.1. Conventional Orthopedic Biomaterials | 12 |
| 1.2. Research Objectives | 14 |
| 1.2.1. Bone as a Nanocomposite Material..... | 15 |
| 1.2.2. Nanostructure Processing of Hydroxyapatite..... | 16 |
| 1.2.2.1. <i>The Effect of Microstructure on Flaw Size and Mechanical Strength</i> | 18 |
| 1.2.2.2. <i>The Effect of Microstructure on Osteoblast Behavior</i> | 18 |
| 1.2.2.3. <i>The Effect of Composition on Flaw Tolerance and Strength</i> | 18 |
| 1.2.2.4. <i>Synthetic Bone Mineral through Nanostructure Processing</i> | 18 |
| 1.3. References | 19 |
| Chapter 2 – Nanocrystalline Hydroxyapatite | 21 |
| 2.1. Introduction | 21 |
| 2.2. Experimental..... | 22 |
| 2.2.1. Hydroxyapatite Synthesis..... | 22 |
| 2.2.2. Characterization of Hydroxyapatite Powders | 22 |
| 2.2.3. Ceramics Sintering and Microstructural Studies..... | 23 |
| 2.2.4. Mechanical Testing of Dense Hydroxyapatite..... | 23 |
| 2.2.5. Cell Culture Studies on Dense Hydroxyapatite | 24 |
| 2.2.5.1. <i>Substrate Preparation</i> | 24 |
| 2.2.5.2. <i>Characterization of Dense Hydroxyapatite Surfaces</i> | 24 |
| 2.2.5.3. <i>Cell Attachment Assay</i> | 25 |
| 2.2.5.4. <i>Cell Adhesion Assay</i> | 25 |
| 2.2.5.5. <i>Cell Proliferation Assay</i> | 26 |
| 2.2.5.6. <i>Mineralization Assay</i> | 26 |
| 2.2.5.7. <i>Statistical Analysis</i> | 27 |
| 2.3. Results and Discussion | 27 |
| 2.3.1. Effect of Processing Conditions on the Precipitation and Sintering of HAP..... | 27 |
| 2.3.1.1. <i>Effect of Aging Time</i> | 28 |
| 2.3.1.2. <i>Effect of Initial Solution pH</i> | 31 |
| 2.3.1.3. <i>Effect of Aging Temperature</i> | 34 |
| 2.3.2. Sintering Behavior of Nanostructured Hydroxyapatite..... | 36 |

| | |
|--|-----------|
| 2.3.3. Mechanical Properties of Nanostructured Hydroxyapatite | 41 |
| 2.3.4. Cell Culture Studies | 42 |
| 2.3.4.1. <i>Surface Characterization of Dense Hydroxyapatite</i> | 42 |
| 2.3.4.2. <i>Osteoblast Attachment to Nanostructured Hydroxyapatite</i> | 43 |
| 2.3.4.3. <i>Osteoblast Adhesion on Nanostructured Hydroxyapatite</i> | 44 |
| 2.3.4.4. <i>Osteoblast Proliferation on Nanostructured Hydroxyapatite</i> | 46 |
| 2.3.4.5. <i>Osteoblast Mineralization on Nanostructured Hydroxyapatite</i> | 47 |
| 2.4. Conclusions | 50 |
| 2.5. References | 50 |
| Chapter 3 – Hydroxyapatite-based Nanocomposites | 53 |
| 3.1. Background and Motivation..... | 53 |
| 3.2. Experimental..... | 54 |
| 3.2.1. Preparation of Hydroxyapatite-Zirconia Nanocomposite Powders | 54 |
| 3.2.1.1. <i>Zirconia Synthesis</i> | 54 |
| 3.2.1.2. <i>HAP-Zirconia Nanocomposite Synthesis by a Colloidal Addition Technique</i> | 54 |
| 3.2.1.3. <i>HAP-Zirconia Nanocomposite Synthesis by a Gel Mixing Technique</i> | 55 |
| 3.2.2. Preparation of HAP-Silver Nanocomposite Powders | 55 |
| 3.2.3. Characterization of Nanocomposite Powders | 56 |
| 3.2.4. Sintering Studies and Microstructure Characterization | 56 |
| 3.2.5. Mechanical Testing of Nanocomposites | 57 |
| 3.3. Results and Discussion | 57 |
| 3.3.1. HAP-Zirconia Nanocomposites | 57 |
| 3.3.1.1. <i>Effect of Synthesis Method on Sintering and Microstructure</i> | 57 |
| 3.3.1.2. <i>Effect of Zirconia Loading on Sintering and Microstructure</i> | 59 |
| 3.3.1.3. <i>Effect of Zirconia Loading on Mechanical Properties</i> | 61 |
| 3.3.2. HAP-Silver Nanocomposites | 64 |
| 3.4. Conclusions | 67 |
| 3.5. References | 67 |
| Chapter 4 – Carbonated Apatite Nanocrystals | 69 |
| 4.1. Introduction | 69 |
| 4.2. Experimental..... | 70 |
| 4.2.1. Synthesis of Carbonated Apatite..... | 70 |
| 4.2.2. Characterization of Carbonated Apatite..... | 72 |

| | |
|---|-----------|
| 4.3. Results and Discussion | 72 |
| 4.3.1. Effect of Aging Time on Apatite Chemistry and Phase Stability | 72 |
| 4.3.2. Effect of Aging Temperature on Apatite Chemistry and Phase Stability | 75 |
| 4.3.3. Effect of Ammonium Carbonate Concentration on Carbonate Substitution | 79 |
| 4.4. Conclusions | 88 |
| 4.5. References | 89 |
| Chapter 5 – Recommendations for Future Work..... | 91 |
| Chapter 6 – Conclusions..... | 93 |

List of Figures

| | |
|--|----|
| Figure 1.1. Open tibial fracture of a 46-year-old male (a) before surgery, (b) after insertion of titanium internal fixation devices, and (c) after removal of the fixation devices [1]. | 12 |
| Figure 1.2. Hierarchical structure of human femur [11]. | 16 |
| Figure 1.3. A representative stress-strain curve for human compact bone, illustrating a mechanical behavior that is strain rate sensitive [3]. | 16 |
| Figure 1.4. Simplified crystal structure of hydroxyapatite. | 17 |
| Figure 2.1. TEM micrographs illustrating 550°C-calcined HAP particles that were aged for (a) 0 hr, (b) 10 hr, (c) 50 hr, and (d) 100 hr. | 29 |
| Figure 2.2. PA-FTIR spectra of 550°C-calcined HAP nanocrystals that were aged for (a) 0 hr, (b) 10 hr, (c) 50 hr, and (d) 100 hr. | 29 |
| Figure 2.3. SEM micrographs of HAP samples (a) A, (b) B, (c) C and (d) D after pressure-assisted sintering at 900°C and 100 MPa. | 30 |
| Figure 2.4. PA-FTIR spectra of 550°C-calcined HAP samples (a) E, (b) D and (c) F. | 32 |
| Figure 2.5. SEM micrographs of HAP samples (a) E, (b) D and (c) F after pressure-assisted sintering at 900°C and 100 MPa. | 33 |
| Figure 2.6. TEM micrographs illustrating 550°C-calcined HAP particles that were aged at (a) 0°C, (b) 25°C and (c) 80°C. | 35 |
| Figure 2.7. PA-FTIR spectra of 550°C-calcined HAP particles that were aged at (a) 0°C, (b) 25°C and (c) 80°C. | 35 |
| Figure 2.8. SEM micrographs of HAP samples (a) G, (b) D and (c) H after pressure-assisted sintering at 900°C and 100 MPa. | 36 |
| Figure 2.9. Effect of sintering temperature on (a) densification and grain size measured by SEM, and (b) XRD phase composition of HAP sample D in pressure-assisted sintering at 100 MPa. | 38 |
| Figure 2.10. SEM micrographs of polished cross-sections of (a,b) commercial HAP and (c,d) nanocrystalline HAP (sample D), after pressure-assisted sintering at 900°C and 100 MPa. | 39 |
| Figure 2.11. Effect of pressureless sintering temperature on (a) densification of nanocrystalline HAP (sample D) and literature HAP samples [11, 23], and (b) XRD phase composition of nanocrystalline HAP (sample D). | 40 |
| Figure 2.12. SEM micrographs comparing the microstructures of (a) Nano HAP and (b) Poly HAP. | 43 |
| Figure 2.13. Attachment of primary human osteoblasts on different substrates. Values are mean \pm standard error of the mean. * P < 0.05 compared to Poly HAP. † P < 0.05 compared to nTCPS. ‡ P < 0.05 compared to TCPS. | 44 |
| Figure 2.14. MC3T3 osteoblast cell adhesion on different substrates after 24 hr of incubation. Values are mean \pm standard error of the mean. * P < 0.05 compared to Poly HAP. † P < 0.05 compared to nTCPS. ‡ P < 0.05 compared to TCPS. | 45 |

| | |
|--|----|
| Figure 2.15. SEM micrographs of MC3T3 osteoblasts on (a) nTCPS, (b) Nano HAP, (c) Poly HAP, and (d) TCPS after 24 hr of incubation..... | 46 |
| Figure 2.16. Proliferation of primary human osteoblasts on different substrates. Values are mean \pm standard error of the mean. * P < 0.05 compared to Poly HAP. † P < 0.05 compared to nTCPS. ‡ P < 0.05 compared to TCPS. | 47 |
| Figure 2.17. Osteocalcin concentration in the mineralizing medium for primary human osteoblasts incubated on different substrates. Values are mean \pm standard error of the mean. * P < 0.05 compared to Poly HAP. † P < 0.05 compared to nTCPS. ‡ P < 0.05 compared to TCPS. | 48 |
| Figure 2.18. Laser scanning confocal micrographs of cell layers on HAP substrates at 28 d, where collagen I, F-actin, and mineralized deposits have been fluorescently labeled in (a) Nano HAP and (c) Poly HAP, and where only collagen I and mineralized deposits have been fluorescently labeled in (b) Nano HAP and (d) Poly HAP. Mineralized regions were contained within the white circles..... | 49 |
| Figure 3.1. TEM micrographs of HAP-zirconia (3 wt%) nanocomposite powders prepared by gel mixing with (a) amorphous zirconium hydroxide and (b) crystalline zirconia, and (c) by colloidal addition of crystalline zirconia..... | 58 |
| Figure 3.2. Backscattered SEM micrographs of HAP-zirconia (3 wt%) nanocomposites after pressure-assisted sintering at 1000°C and 50 MPa. The samples were prepared by gel mixing with (a) amorphous zirconium hydroxide and (b) crystalline zirconia, and (c,d) by colloidal addition of crystalline zirconia..... | 59 |
| Figure 3.3. Sintering curves of HAP-zirconia nanocomposites with (a) 0, (b) 3 and (c) 15 wt% zirconia, prepared by colloidal addition..... | 60 |
| Figure 3.4. Backscattered SEM micrographs of HAP-zirconia nanocomposites pressure-assisted sintered at 1000°C and 50 MPa. The samples have zirconia loadings of (a) 0, (b) 3, (c) 8 and (d) 15 wt%..... | 60 |
| Figure 3.5. Vickers hardness of HAP-zirconia nanocomposites as a function of (a) TZ and (b) YSZ loadings..... | 62 |
| Figure 3.6. Thin-section high-resolution TEM micrographs of pressure-assisted sintered nanocrystalline (a,b) HAP and (c,d) HAP-zirconia (3 wt%). | 63 |
| Figure 3.7. Bending strength of HAP-silver nanocomposites as a function of silver loading..... | 65 |
| Figure 3.8. Compressive strength of HAP-silver nanocomposites as a function of silver loading. | 65 |
| Figure 3.9. Backscattered SEM micrographs of sintered HAP-silver nanocomposites with (a) 1, (b) 5, (c) 20 and (d) 30 vol% silver. The bright pixels in the micrographs corresponded to silver..... | 66 |
| Figure 4.1. The XRD phase behavior of calcium phosphate precipitates aged at 25°C for (a) 24 and (b) 100 hr..... | 73 |
| Figure 4.2. XRD patterns of calcium phosphate precipitates aged for 24 hr at 25°C with a precursor Ca/P ratio of 1.67 and (a) 0, (b) 0.3 and (c) 2.0 M NHC in the reaction medium. All peaks corresponded to the apatitic phase. | 74 |

| | |
|--|----|
| Figure 4.3. XRD patterns of calcium phosphate precipitates aged for 24 hr at 25°C with a precursor Ca/P ratio of 3.33 and (a) 0, (b) 0.3 and (c) 2.0 M NHC in the reaction medium. Peaks in (a) corresponded to the apatitic phase. Peaks in (b) corresponded to calcium carbonate. Peaks in (c) corresponded to an amorphous phase..... | 74 |
| Figure 4.4. The XRD phase behavior of calcium phosphate precipitates aged for 24 hr at (a) 25°C and (b) 80°C..... | 76 |
| Figure 4.5. XRD patterns of calcium phosphate precipitates synthesized with a precursor Ca/P ratio of 1.67 and (a) 0, (b) 0.1 and (c) 0.3 M NHC in the reaction medium, and aged at 80°C for 24 hr. All peaks corresponded to the apatitic phase..... | 76 |
| Figure 4.6. The XRD phase behavior of calcium phosphate precipitates aged for 100 hr at (a) 25°C and (b) 120°C..... | 77 |
| Figure 4.7. XRD patterns of calcium phosphate precipitates synthesized with a precursor Ca/P ratio of 1.67 and (a) 0, (b) 0.3 (c) 0.9 M NHC in the reaction medium, and aged at 120°C for 100 hr. All peaks corresponded to the apatitic phase..... | 78 |
| Figure 4.8. The effect of NHC concentration on the measured Ca/P ratio of carbonated apatites synthesized with a precursor Ca/P ratio of (◆) 1, (■) 1.67, (▲) 3.33 and (●) 5, and aged at 120°C for 100 hr. All samples were of an apatitic phase..... | 79 |
| Figure 4.9. TEM micrographs of carbonated apatites prepared with a precursor Ca/P ratio of 1.67, and (a) 0, (b) 0.3 and (c) 2.0 M NHC with aging at 25°C for 24 hr, and (d) 0, (e) 0.3 and (f) 0.9 M NHC with hydrothermal aging at 120°C for 100 hr..... | 80 |
| Figure 4.10. PA-FTIR spectra of poorly crystalline carbonated apatites synthesized with a precursor Ca/P ratio of 1.67 and (a) 0, (b) 0.3 and (c) 2.0 M NHC, with aging at 25°C for 24 hr..... | 81 |
| Figure 4.11. PA-FTIR spectra of highly crystalline carbonated apatites synthesized with a precursor Ca/P ratio of 1.67 and (a) 0, (b) 0.1, (c) 0.3 and (d) 0.9 M NHC, with aging at 120°C for 100 hr..... | 82 |
| Figure 4.12. PA-FTIR spectra of poorly crystalline carbonated apatites synthesized with a precursor Ca/P ratio of 1.67 and (a) 0, (b) 0.3 and (c) 2.0 M NHC, with aging at 25°C for 24 hr..... | 83 |
| Figure 4.13. PA-FTIR spectra of highly crystalline carbonated apatites synthesized with a precursor Ca/P ratio of 1.67 and (a) 0, (b) 0.1 (c) 0.3 and (d) 0.9 M NHC, with aging at 120°C for 100 hr..... | 84 |
| Figure 4.14. TGA-MS analysis showing (a) weight loss and (b) CO ₂ concentration evolved during the heat treatment of poorly crystalline carbonated apatites synthesized with a precursor Ca/P ratio of 1.67 and (i) 0, (ii) 0.1, (iii) 0.3 and (iv) 2.0 M NHC with aging at 25°C for 24 hr..... | 86 |
| Figure 4.15. TGA-MS analysis showing (a) weight loss and (b) CO ₂ concentration evolved during the heat treatment of highly crystalline carbonated apatites synthesized with a precursor Ca/P ratio of 1.67 and (i) 0, (ii) 0.1 and (iii) 0.9 M NHC, with aging at 120°C for 100 hr..... | 88 |

List of Tables

| | |
|--|----|
| Table 2.1. Synthesis conditions for HAP samples..... | 22 |
| Table 2.2. Effect of aging time on HAP calcined at 550°C..... | 28 |
| Table 2.3. Effect of aging time on pressure-assisted sintered HAP..... | 30 |
| Table 2.4. Effect of initial solution pH on HAP calcined at 550°C..... | 31 |
| Table 2.5. Effect of initial solution pH on pressure-assisted sintered HAP. | 33 |
| Table 2.6. Effect of aging temperature on HAP calcined at 550°C..... | 34 |
| Table 2.7. Effect of aging temperature on pressure-assisted sintered HAP..... | 36 |
| Table 2.8. Mechanical properties of nanostructured HAP (sample D) compared to conventional HAP, dental enamel, and compact bone. | 41 |
| Table 2.9. Surface properties of Nano and Poly HAP. | 42 |
| Table 2.10. Mineralized areas on Nano and Poly HAP substrates. | 50 |
| Table 3.1. Conditions for the synthesis of HAP-YSZ nanocomposites..... | 55 |
| Table 3.2. Conditions for the synthesis of HAP-TZ nanocomposites. | 55 |
| Table 3.3. Bending strengths of HAP-TZ and HAP-YSZ nanocomposites. | 63 |
| Table 3.4. Mechanical properties of various materials and HAP-zirconia nanocomposite..... | 64 |
| Table 3.5. Mechanical properties of various materials and HAP-silver nanocomposite..... | 67 |
| Table 4.1. Synthesis conditions for carbonated apatite precipitation. | 71 |
| Table 4.2. Hydrothermal treatment conditions for carbonated apatite. | 71 |
| Table 4.3. Effect of aging time and NHC concentration on the Ca/P molar ratio of carbonated apatite aged at 25°C. | 75 |
| Table 4.4. Effect of aging temperature and NHC concentration on the Ca/P molar ratio of carbonated apatite aged for 24 hr. | 77 |
| Table 4.5. Effect of aging temperature and NHC concentration on the Ca/P molar ratio of carbonated apatite aged for 100 hr. | 78 |
| Table 4.6. Chemical formulas of carbonated apatites prepared with a precursor Ca/P ratio of 1.67 and aged at 25°C for 24 hr. | 83 |
| Table 4.7. Quantitative analysis of PA-FTIR carbonate peak areas located at 850–900 cm ⁻¹ for carbonated apatites prepared with a precursor Ca/P ratio of 1.67 and aged at 120°C for 100 hr. | 87 |

Chapter 1 – Research Motivation and Objectives

1.1. Conventional Orthopedic Biomaterials

The skeletal system is remarkable in that it can recover from a wide variety of injuries with minimal medical intervention. However, in certain cases, such as that illustrated in Figure 1.1, orthopedic surgery is required to rebuild the damaged bone. This 46-year-old male patient has shattered his tibia in Figure 1.1(a); because of the extensive damage, the orthopedic surgeon has had to insert metallic pins and screws for internal fixation and an extracorporeal stabilization device to reconstruct the tibia (Figure 1.1(b)). After the body has reconstituted the shattered elements into a single body, the surgeon performs another operation to remove the metallic devices, introducing further defects into the tibia. Though the tibia has been fused into a single piece, the morphology of the tibia after healing (Figure 1.1(c)) has not been restored to its pre-fractured state [1]. Consequently, this patient will experience chronic pain from the use of metallic fixation devices and an increased susceptibility to reinjury of the weakened tibia.

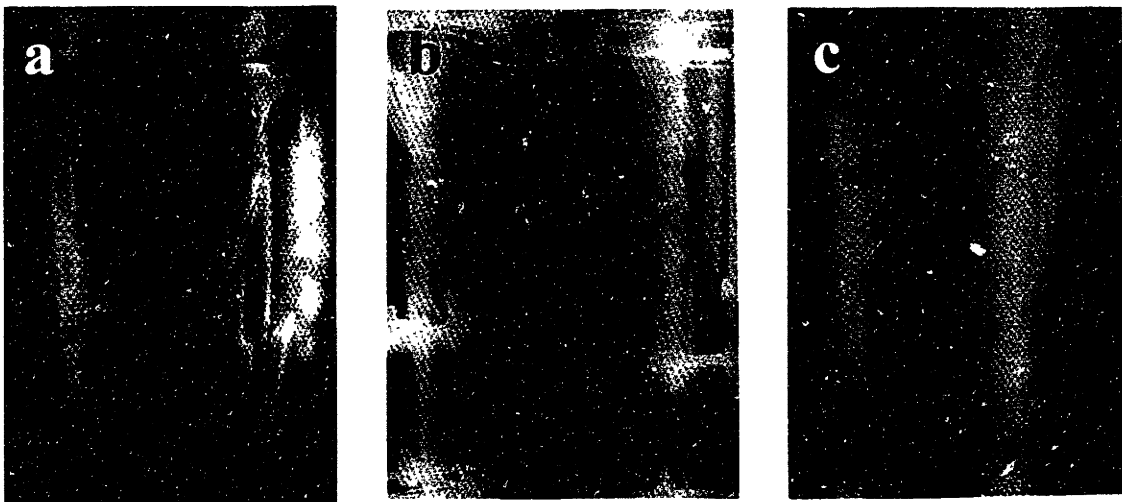


Figure 1.1. Open tibial fracture of a 46-year-old male (a) before surgery, (b) after insertion of titanium internal fixation devices, and (c) after removal of the fixation devices [1].

Historically, bone bonding has been sacrificed for mechanical strength in materials selection for load-bearing orthopedic applications in joint reconstruction, spinal fusion, internal fixation, and craniomaxillofacial implants. Bone bonding was considered undesirable for internal fixation because the fixation devices were often retrieved as shown in Figure 1.1. As a result, the materials used in these implants have largely been limited to bioinert titanium-based and cobalt-based alloys. Although metallic implants have been clinically successful, there are

major problems associated with stress shielding, corrosion, implant-tissue interfacial stability, and post-surgical recovery of the bony tissue [2-4]. As a result, up to 20% of patients receiving joint reconstruction implants must undergo a revision operation [3, 5, 6]. Thus, a need exists for a biomaterial for permanent internal fixation devices and to prevent revision surgeries. Such a material would ideally combine both structural resilience with mechanical properties more similar to bone and a bone-bonding surface to provide a stable interface with the surrounding connective tissue.

Different implant architectures and biomaterials have been attempted to achieve mechanical resilience and bone bonding. The first approach examines alumina and zirconia as possible substitutes for metallic alloys, but clinical results indicate that they induce stress shielding and do not bond with bone.

The second approach focuses on porous implant architectures to enhance mechanical interlocking by increasing the surface area available to bone bonding. Although increasing the interfacial area is expected to reduce implant movement, pore sizes must be greater than 100–150 μm to maintain healthy and viable tissue. These large pores compromise the overall mechanical integrity of the implant. Furthermore, if micromovement does occur, the ingrown tissue is likely to be damaged, inducing inflammation and destroying interfacial stability. Thus, porous implants have been limited to non-load-bearing clinical applications.

The third approach focuses on bioactive materials that elicit a specific biological response at the material interface, causing the formation of a bond between the material and its surrounding tissue [2, 4]. The degree of bioactivity is measured in terms of the rate of bone formation, bonding strength, and thickness of the bonding layer [2, 4]. Common bioactive orthopedic materials are Bioglass®, glass-ceramics, β -tricalcium phosphate ($\beta\text{-Ca}_3(\text{PO}_4)_2$ or β -TCP), calcium sulfate, and hydroxyapatite. Although Bioglass® can rapidly bond to bone, it is limited in strength. The low bending strength of glass-ceramics limits their use to spinal fusion [2, 4]. β -TCP and calcium sulfate are designed to be resorbed, so that the surrounding host tissue replaces the implant. Problems associated with these resorbable systems include the low initial strength, maintenance of strength as the biomaterial degrades, instability of the interface, and mismatching between the resorption rate and the host tissue regeneration rate [2, 4].

Of the bioactive orthopedic materials, hydroxyapatite (HAP) is promising as it is a synthetic analog to native bone mineral and is osteoconductive, with the potential of addressing the issues of mechanical strength and bone-bonding [2]. However, clinical applications, such as cements, coatings, porous bodies, and non-load-bearing implants, have solely focused on the osteoconductivity of HAP [3]. To be used as a load-bearing orthopedic implant, HAP powder must be formed into a high-strength bulk material via a high-temperature densification process. Conventionally processed HAP lacks phase purity and chemical homogeneity. Since HAP is sensitive to impurities and nonstoichiometries [7, 8], conventional HAP decomposes into undesired phases during high-temperature sintering, resulting in incomplete densification, poor mechanical strength, and high dissolution rates [9, 10].

The most clinically successful approach to achieving strength and bone bonding is obtained by plasma or thermal spraying “porous” hydroxyapatite onto titanium alloy implants. The titanium implant provides mechanical strength, while the hydroxyapatite coating shields the body from the implant and provides a surface for bone attachment. Plasma and thermal spraying can create a roughened/porous surface, increasing the interfacial surface area. These techniques involve feeding hydroxyapatite particles into an electric arc plasma at 10,000-30,000°C. Hydroxyapatite decomposes at these high temperatures, undergoing phase transformation to amorphous calcium phosphate ($\text{Ca}_x(\text{PO}_4)_y$ or ACP), α -TCP, β -TCP, tetracalcium phosphate ($\text{Ca}_4\text{P}_2\text{O}_9$ or TTCP), and CaO. These phases often result in a coating that degrades too rapidly to form a bond with bone.

1.2. Research Objectives

Compared to conventional orthopedic biomaterials, bone is a structurally and biologically complex multifunctional tissue. It provides a structural support for our bodies and encases a thriving population of cells and a blood supply. This dynamic tissue responds to biochemical, mechanical, and electrical signals by remodeling itself so that maximum strength and toughness are along the lines of the greatest applied stress; whereas conventional biomaterials respond to the physiological environment either passively or negatively. The ideal orthopedic biomaterial should mimic the mechanical properties of bone, sustain a cell population on its surface, and respond to stimuli. The objective of this research is to develop an orthopedic biomaterial that

emulates the microstructural elements and compositions of bone to obtain the desired characteristics.

1.2.1. Bone as a Nanocomposite Material

Bone is an organic-inorganic nanocomposite composed of (i) collagen (35 dry wt%) for flexibility and toughness, (ii) carbonated apatite (65 dry wt%) for structural reinforcement and stiffness, and (iii) bone matrix for support of cellular functions [11, 12]. Its microstructure is further organized three-dimensionally along multiple length scales so that maximum strength and toughness are along the lines of the applied stress [12, 13]. For example, the femur consists of a dense shell of cortical bone at the center, and a porous trabecular bone to optimize weight transfer and minimize friction in the articulating joints (see Figure 1.2). The dense cortical bone and trabecular struts are composed of mineralized collagen fibrils that are stacked in parallel to form layers and then assembled in a $\pm 45^\circ$ fashion. Each of the collagen fibrils consists of bundles of microfibrils that in turn contain bundles of collagen molecules. The collagen molecules are arranged with a periodicity of 67 nm; where two ends meet, there is a small gap of 40 nm, or hole zone, where most of the 35 nm x 25 nm plates of bone mineral are located.

Bone behaves as a tough material at low strain rates (0.001/s), but as a brittle material at high strain rates (1500/s) (see Figure 1.3) [3]. As the fundamental structure of bone involves the coordination of bone mineral nanocrystals and collagen, the number and sizes of flaws are minimized to yield unusual mechanical properties. Bone's microstructure further acts as a scaffold for cell regulation. The surface features that these cells encounter are mostly nanometer in dimension, suggesting that this length scale is critical in regulating cell behavior.

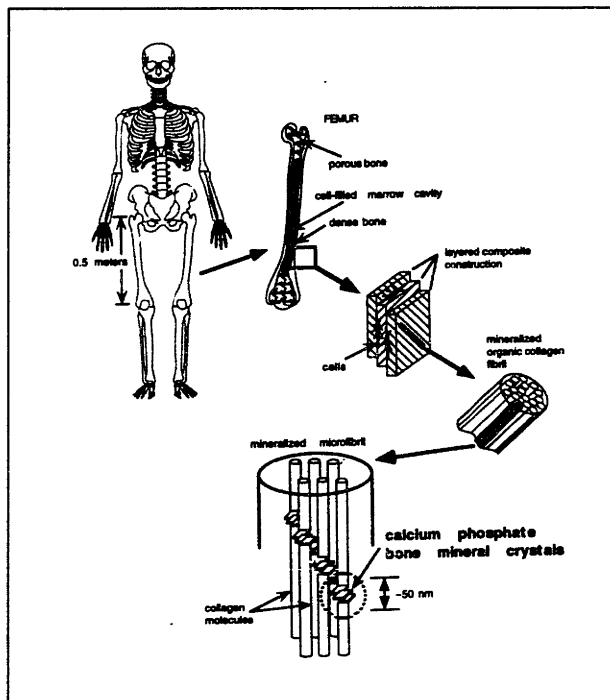


Figure 1.2. Hierarchical structure of human femur [11].

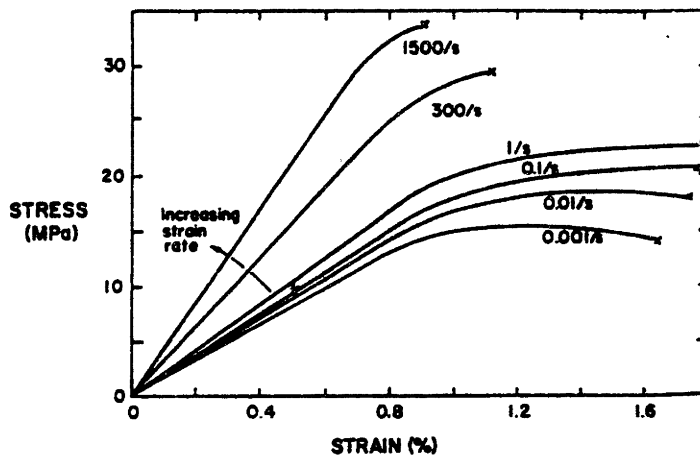


Figure 1.3. A representative stress-strain curve for human compact bone, illustrating a mechanical behavior that is strain rate sensitive [3].

1.2.2. Nanostructure Processing of Hydroxyapatite

HAP is tolerant of vacancies and substitutions because of its complex composition ($\text{Ca}_{10}(\text{PO}_4)_6(\text{OH})_2$) and crystal structure ($P6_3/m$) (see Figure 1.4). For example, stoichiometric HAP has a Ca/P ratio of 1.67, but nonstoichiometric HAP having a Ca/P ratio greater than 1.44 or less than 2.4 still possesses an apatitic crystal structure by X-ray diffraction. In addition, calcium can be easily substituted with other Group I and II elements, while the phosphate group

can be substituted with AsO_4^{3-} , VO_4^{3-} , SiO_4^{4-} , SO_4^{2-} , CO_3^{2-} , etc. Furthermore, the hydroxide site can be substituted with F^- , Cl^- , Br^- , I^- , CO_3^{2-} , etc. [14, 15]. Thus, impurities and non-stoichiometries can be easily introduced in typical synthesis [7, 8]. Consequently, conventionally processed HAP demonstrates poor chemical and thermal stability, and decomposes when densified at high temperatures [9, 10].

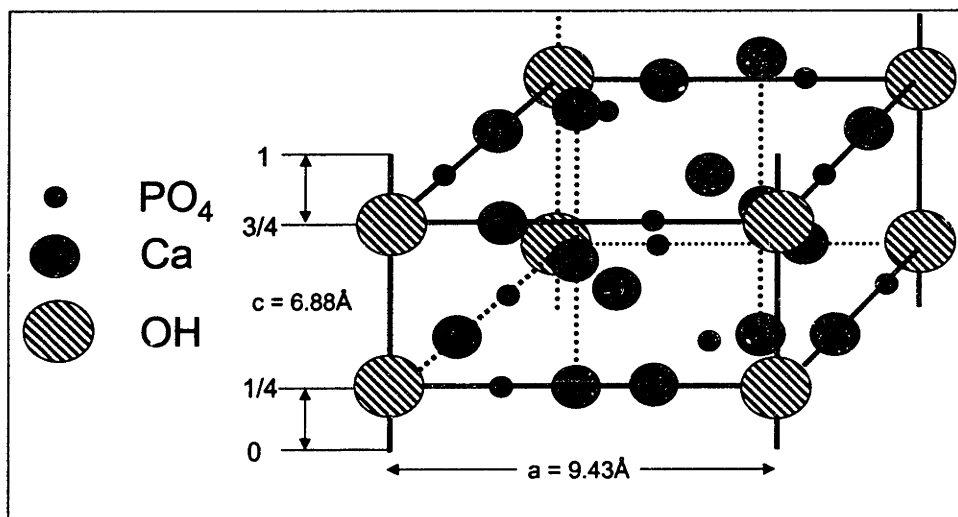


Figure 1.4. Simplified crystal structure of hydroxyapatite.

Since nanostructure processing allows for materials design from the molecular level, it can be used to overcome the deficiencies in conventional processing by controlling characteristics such as stoichiometry, crystallinity, particle morphology, and grain size. Processing conditions can also be optimized to yield HAP nanocrystals with superior phase purity and chemical homogeneity so that excellent thermal stability and sinterability may be attained. Unique size-dependent properties can also be achieved with nanocrystalline compacts. For example, it has been shown that nanocrystalline metallic, intermetallic and ceramic monoliths possess mechanical properties substantially different from their conventional polycrystalline counterparts through flaw size reduction and grain boundary sliding [16-18]. Furthermore, osteoblast attachment and proliferation have been shown to be enhanced by the surfaces of nanocrystalline alumina and zirconia monoliths [19-21]. Thus, nanostructure processing offers the potential to control HAP composition and structure in obtaining a synthetic bone mineral with excellent mechanical strength and bone bonding characteristics.

1.2.2.1. The Effect of Microstructure on Flaw Size and Mechanical Strength

Typically, materials fail mechanically when the stress concentration is exceeded at a critical flaw. Bone is engineered with a microstructure possessing nanometer-sized features to minimize the number and size of its critical flaws. By attaining structural features at a length scale similar to bone, nanostructure processing can be used to achieve HAP compacts with uniform and ultrafine microstructures. This will reduce the flaw sizes in dense HAP monoliths for increased mechanical reliability.

1.2.2.2. The Effect of Microstructure on Osteoblast Behavior

The nanocrystallinity of dense HAP monoliths may provide a structure that can enhance interactions with osteoblasts. Since the feature size and composition of nanocrystalline HAP is similar to that of bone, osteoblast attachment, proliferation and mineralization on nanocrystalline HAP may be greater than those on other load-bearing orthopedic materials. The expected increase in osteoblast adhesion and bone mineral formation may be correlated to the large volume fraction of grain boundaries.

1.2.2.3. The Effect of Composition on Flaw Tolerance and Strength

As illustrated in Figure 1.2, bone has a high flaw tolerance due to the nanoscale dispersion of carbonated apatite bone mineral and collagen. The ultrahigh dispersion yields uniform microstructures (i.e. fewer flaws) and better mechanical reinforcement. Using nanostructure processing, we can also introduce a highly dispersed secondary phase to mechanically reinforce the HAP matrix. For example, zirconia dispersoids can be used to toughen the HAP matrix by transformation toughening and/or crack deflection. Silver dispersoids can be employed to toughen the HAP matrix by crack bridging and/or plastic deformation.

1.2.2.4. Synthetic Bone Mineral through Nanostructure Processing

Although the precise crystal structure of bone remains elusive, the mineral phase of bone has been determined to be a poorly crystalline carbonated apatite where the phosphate ions are substituted with carbonate ions. Nanostructure processing can be used to precipitate a synthetic carbonated apatite with similar characteristics as the native bone mineral and to promote resorption by tailoring the site and extent of carbonate substitution into the apatitic lattice.

1.3. References

- [1] G. A. Ilizarov, *Transosseous Osteosynthesis* (Springer-Verlag, New York, 1992).
- [2] L. L. Hench, *J. Am. Ceram. Soc.* **74**, 1487 (1991).
- [3] W. Suchanek, M. Yoshimura, *J. Mater. Res.* **13**, 94 (1998).
- [4] L. L. Hench, E. C. Etheridge, *Biomaterials: An Interfacial Approach* (Academic Press, New York, 1982).
- [5] L. L. Hench, in *Bioactive Ceramics*, P. Ducheyne, J. Lemmons, Eds. (Annals of New York Academy of Sciences, New York, 1988), vol. 523, p. 24.
- [6] U. Gross, R. Kinne, H. J. Schmitz, V. Strunzve, *CRC Crit. Rev. Biocomp.* **4**, 155 (1988).
- [7] A. Slosarczyk, E. Stobierska, Z. Pazkiewicz, M. Gawlicki, *J. Am. Ceram. Soc.* **79**, 2539 (1996).
- [8] M. T. Fulmer, R. I. Martin, P. W. Brown, *J. Mater. Sci. Mater. Med.* **79**, 2539 (1992).
- [9] M. Akao, H. Aoki, K. Kato, *J. Mater. Sci.* **16**, 809 (1981).
- [10] A. J. Ruys, *et al.*, *Biomater.* **16**, 409 (1995).
- [11] L. Kuhn-Spearing, C. Rey, H. M. Kim, M. J. Glimcher, Carbonated Apatite Nanocrystals from Bone, TMS Annual Meeting (1996).
- [12] A. Ravagliodi, A. Krajewcki, *Bioceramics: Materials, Properties, Applications* (Chapman & Hall, New York, 1992).
- [13] P. Fratzl, N. Fratzl-Zelman, K. Klaushofer, *Biophys. J.* **64**, 260 (1993).
- [14] J. C. Elliot, *Studies in Inorganic Chemistry 18: Structure and Chemistry of the Apatites and Other Calcium Orthophosphates* (Elsevier Science, New York, 1994).
- [15] D. E. C. Corbridge, *Studies in Inorganic Chemistry 10: Phosphorous, An Outline of Its Chemistry, Biochemistry, and Technology* (Elsevier Science, New York, 1990).
- [16] K. A. Padamanabhan, H. Hahn, in *Synthesis and Processing of Nanocrystalline Powders*, D. L. Bourell, Ed. (The Mineral, Metals and Materials Society, Philadelphia, 1996), p. 21.
- [17] M. J. Mayo, in *Nanostructured Materials: Science and Technology*, G. M. Chow, N. I. Noskova, Eds. (Kluwer, Netherlands, 1998), p. 361.

- [18] K. Niihara, *J. Ceram. Soc. Jpn.* **99**, 974 (1991).
- [19] T. J. Webster, R. W. Siegel, R. Bizios, in *Bioceramics*, R. Z. LeGeros, J. P. LeGeros, Eds. (World Scientific Publishing, New York, 1998), vol. 11, p. 273.
- [20] T. J. Webster, R. W. Siegel, R. Bizios, *Biomater.* **20**, 1221 (1999).
- [21] T. J. Webster, C. Ergun, R. H. Doremus, R. W. Siegel, R. Bizios, *Biomater.* **21**, 1803 (2000).

Chapter 2 – Nanocrystalline Hydroxyapatite

2.1. Introduction

Cobalt-, chromium-, nickel- and titanium-based alloys, as well as polycrystalline alumina and zirconia ceramics, have been the focus for developing orthopedic load-bearing applications, dental implants, and alveolar ridge augmentation [1-4]. Although clinically successful, stress-shielding, corrosion and implant-tissue interfacial stability present major problems in the applications of metallic implants. Analysis over the past twenty years indicates that most failures involved an unstable implant-tissue interface, and/or a mismatch in the mechanical behavior of the implant with its surrounding tissue [1, 3-6]. Thus, it would be very attractive to develop hard tissue implant materials that offer a stable interface with the connective tissue, with a matching mechanical behavior as the tissue to be replaced [1, 3, 4, 6].

Unlike metallic implants, bioceramic materials may be tailored for corrosion resistance, mechanical strength, and bonding with the surrounding tissue. Bioactive ceramics, such as hydroxyapatite (HAP), Bioglass®, Ceravital®, and A/W glass-ceramics, possess enhanced interfacial stability [1, 3-6] since their surface reactions give rise to specific biological responses that form a bond between the tissue and the material [1, 3, 4, 6, 7]. However, they have been limited to coatings and non-load-bearing applications due to their poor mechanical properties.

Of particular interest for orthopedic and dental implant applications is HAP ($\text{Ca}_{10}(\text{PO}_4)_6(\text{OH})_2$), which closely resembles native bone mineral and is inherently osteoconductive. Applications of conventional HAP have been limited to powders, coatings, porous implants, and as a bioactive phase in composites [1] due to its poor processability and mechanical properties. To be used for load-bearing applications, HAP powders must be consolidated into a bulk monolith and densified. However, HAP is difficult to sinter, and dense HAP ceramics have to be obtained by high-temperature sintering with glassy additives. This frequently induces HAP decomposition to undesirable phases with poor mechanical and chemical stability [1, 4, 8-11].

In this chapter, we demonstrate that nanostructure processing of HAP offers the microstructural control necessary to enhance sintering behavior and, consequently, the mechanical strength and bioactivity of this bioceramic system. Nanostructured HAP powders are also shown to exhibit superior chemical and thermal stability by virtue of their superb

chemical homogeneity and phase purity. By understanding the chemical precipitation processing parameters, the chemical and physical properties of HAP powders are optimized to yield materials with unique nanostructured features for high-strength bioactive implant applications.

2.2. Experimental

2.2.1. Hydroxyapatite Synthesis

Reagent grade $\text{Ca}(\text{NO}_3)_2 \cdot 4\text{H}_2\text{O}$ (CaN; Fluka) and $(\text{NH}_4)_2\text{HPO}_4$ (NHP; Fluka) were used as starting materials. A 0.167 M $\text{Ca}(\text{NO}_3)_2$ solution and a 0.100 M $(\text{NH}_4)_2\text{HPO}_4$ solution were prepared, and their pH's were adjusted by adding concentrated NH_4OH . 900 ml of a 0.167 M solution of $\text{Ca}(\text{NO}_3)_2$ were added to 900 ml of a 0.100 M solution of $(\text{NH}_4)_2\text{HPO}_4$ at approximately 3 ml/min. The resulting solution was magnetically stirred for 10, 50 or 100 hr, and aged at 0, 25 or 80°C. After aging, the white precipitate was subjected to aqueous washes with solutions of decreasing pH, followed by a series of ethanol washes. The gel was ground dry with a heated mortar and pestle. The powder was then oven-dried at 120°C overnight and calcined in oxygen at 550°C for 2 hr (ramp rate = 10°C/min). The synthesis conditions for various HAP samples are shown in Table 2.1.

Table 2.1. Synthesis conditions for HAP samples.

| Sample Name | Precursor Conc. [M] | | Solution pH | | Aging Time (hr) | Aging Temperature (°C) |
|-------------|---------------------|-------|-------------|------|-----------------|------------------------|
| | CaN* | NHP** | CaN | NHP | | |
| A | 0.167 | 0.1 | 10.4 | 10.4 | 0 | 25 |
| B | 0.167 | 0.1 | 10.4 | 10.4 | 10 | 25 |
| C | 0.167 | 0.1 | 10.4 | 10.4 | 50 | 25 |
| D | 0.167 | 0.1 | 10.4 | 10.4 | 100 | 25 |
| E | 0.167 | 0.1 | 6.1 | 10.4 | 100 | 25 |
| F | 0.167 | 0.1 | 11.8 | 11.0 | 100 | 25 |
| G | 0.167 | 0.1 | 10.4 | 10.4 | 100 | 0 |
| H | 0.167 | 0.1 | 10.4 | 10.4 | 100 | 80 |

*CaN = Calcium Nitrate

**NHP = Ammonium Phosphate

2.2.2. Characterization of Hydroxyapatite Powders

Powder X-ray diffraction (XRD) patterns of calcined HAP powders were obtained with a Siemens D5000 θ - θ diffractometer (45 kV, 40 mA, Cu K_α). Grain size analyses were performed on the <002> and <300> diffraction peaks using Scherrer's method. The BET surface area of the 550°C-calcined HAP powders were evaluated by nitrogen adsorption on a Micromeritics ASAP 2000/2010 Analyzer. Photoacoustic Fourier-transform infrared (PA-FTIR) spectroscopy was performed on a Biorad FTS-60A spectrometer with a MTEC photoacoustic attachment.

Chemical analysis by inductively coupled plasma – atomic emission spectroscopy (ICP-AES) was performed on a Perkin-Elmer Plasma 40 spectrometer, and particle size analysis was attained with a Horiba CAPA-300 Particle Size Analyzer. Particle morphology was determined by transmission electron microscopy (TEM) with a JEOL 200CX or JEOL 2000 microscope.

2.2.3. *Ceramics Sintering and Microstructural Studies*

Calcined HAP samples were subjected to pressure-assisted and pressureless sintering. For the former, ~ 2 g of HAP powders were placed in 20 mm-diameter graphite dies in a graphite vacuum furnace (Materials Research Furnace H-4.5x7-G-2000-V&G). The furnace was subsequently evacuated and purged with dry nitrogen three times to a final pressure of 3×10^{-2} mbar, whereupon a pressure of 100 MPa was applied to the powder at a sintering temperature of 500–1300°C for 30 min (ramp rate = 5°C/min). For pressureless sintering, ~ 0.15 g of HAP powders were uniaxially pressed in 10 mm-diameter stainless steel dies to 150 MPa. The pellets were next cold isostatically pressed (CIPed) at 300 MPa for 3 min, and sintered in an oxygen atmosphere at 800–1300°C for 2 hr (ramp rate = 5°C/min). The density of the sintered pellets was measured with water by Archimedes' method, and compared to the theoretical density of HAP (3.16 g/cm^3). The sintered pellets were polished with 0.05- μm $\gamma\text{-Al}_2\text{O}_3$ (Buehler); their surfaces were lightly etched in 0.01 M lactic acid for 20 sec and analyzed by XRD for phase composition. Following the acid etch, the surfaces of the sintered pellets were coated with 50 Å of gold-palladium. Microstructural analysis was performed with a JEOL 6320 field emission gun scanning electron microscope (FEGSEM).

2.2.4. *Mechanical Testing of Dense Hydroxyapatite*

The optimal HAP sample pressure-assisted sintered at 900°C was subjected to ultimate-point compressive strength measurements using an Instron Series 1125 Universal Test Instrument with a 20,000-lb_f load cell. Tests were performed on 2 mm x 4 mm x 10 mm bars at a crosshead speed of 0.05 in/min. Ultimate point 3-point bending strength of the optimal HAP sample (2 mm x 4 mm x 20 mm) was also measured using Instron 1125 fitted with a 1,000-lb_f load cell. The span of the 3-point bending fixture was set at 15 mm. The crosshead speed was set at 0.005 in/min. Data from the 3-point bending tests were evaluated using ASTM C1161-94.

Pellets were polished to a P4000 SiC grit, and tested for Vickers hardness using a LECO DM-400 instrument. A force of 200 gf was applied for 10 sec to obtain an indentation with crack propagation. The critical fracture toughness, K_{Ic} , was determined from

$$K_{Ic} = 0.203 H (a^2/c^{3/2}) \quad (2.1)$$

where H is the Vickers hardness, a is the characteristic dimension of the indentation, and c is the characteristic crack length [12].

2.2.5. Cell Culture Studies on Dense Hydroxyapatite

2.2.5.1. Substrate Preparation

In the cell culture studies on dense HAP, the effect of HAP microstructure on osteoblast adhesion, attachment and mineralization was evaluated. Osteoblast response to nanocrystalline HAP (Nano HAP) was compared to their response to polycrystalline HAP (Poly HAP). Tissue culture polystyrene (TCPS, Becton Dickinson) was used as positive control, and non-tissue culture polystyrene (nTCPS, Becton Dickinson) was used as a negative control.

Nano HAP was prepared according to the conditions that yielded dense, nanostructured HAP as established in Section 2.2.1 (sample D). Nanostructured HAP powders were calcined at 550°C for 2 hr (ramp = 10°C/min) in oxygen. They were pressure-assisted sintered at 900°C for 30 min (ramp = 5°C/min) under an uniaxial load of 100 MPa in a 8 mm-diameter graphite die. The resulting dense HAP cylinders were sectioned into discs using a diamond wafering blade (Buehler) and polished to a mirror finish using a 0.01- μ m diamond paste. To form Poly HAP, discs of Nano HAP were subjected to a post-sintering heat treatment at 1200°C for 2.5 hr (ramp = 5°C/min) in an oxygen atmosphere saturated with water. The Poly HAP discs were also polished to a mirror finish with a 0.01- μ m diamond paste. All HAP discs were sterilized with ethylene oxide.

2.2.5.2. Characterization of Dense Hydroxyapatite Surfaces

The microstructure and surface chemistry of the different HAP surfaces were characterized with scanning electron microscopy (SEM), atomic force microscopy (AFM), sessile contact angle measurements, and X-ray photoelectron spectroscopy (XPS). SEM (JEOL 6320 Field Emission Gun Scanning Electron Microscope) was used to evaluate the microstructural differences between Nano HAP and Poly HAP. AFM (Digital Instruments Nanoscope IIa Scanning Probe Microscope) was used to determine the difference in surface

roughness between the different HAP surfaces, and sessile contact angle measurements (Ramé Hart Goniometer) were used to determine HAP surface hydrophilicity. XPS (Surface Science 206 X-Ray Photoelectron Spectrometer, Al K α) was used to determine the surface concentration of calcium and phosphorous.

2.2.5.3. Cell Attachment Assay

To observe the rate of attachment of osteoblasts to the different HAP surfaces, primary human osteoblasts (NHOst; Clonetics) were seeded at an initial density of 100 cells/mm², and incubated with Osteoblast Growth Medium (OGM; Clonetic) supplemented with 0.1% ascorbic acid, 10% FBS and 0.1% antibiotic (OGM BulletKit; Clonetics) at standard cell culture conditions (37°C, humidified 5% CO₂/95% air). Osteoblasts at population numbers 3–5 were used in this study. For the attachment assay, samples were collected at 1 hr, 3 hr, 6 hr, 12 hr and 24 hr with a sample size of n = 3 for each time point. Cells were fixed with 4% formaldehyde *in situ*. After fixation, HAP samples were stained with a fluorescent Hoechst dye (Polysciences), while TCPS and nTCPS surfaces were stained with Bradford Reagent (Sigma-Aldrich). An epifluorescent microscope (Zeiss III RS; 365 nm excitation, 400 nm emission) was used to count the number of cells attached to the HAP surfaces in nine random fields per surface. An optical microscope (Nikon Labophot-2) was used to count the number of cells attached to the surface in nine random fields per surface for the cells stained with Bradford Reagent. The average cell count per substrate was expressed as cell density in units of cells/mm².

2.2.5.4. Cell Adhesion Assay

The cell line used in the cell adhesion assay was a MC3T3 immortalized murine osteoblast donated by Dr. Louis Gerstenfeld (Boston Medical Center). The MC3T3 osteoblasts were incubated in Dulbecco's modified Eagle medium (DMEM; Gibco) supplemented with 10% heat-inactivated fetal bovine serum (FBS; Hyclone) and 2% antibiotic (Gibco) at standard cell culture conditions (37°C, humidified 5% CO₂/95% air). To determine the effect of HAP microstructure on osteoblast adhesion, cell spreading was measured after 24 hr of incubation in DMEM. The initial seeding density was 40 cells/mm². The sample size used in this study was n = 6 for Nano HAP, Poly HAP, TCPS and nTCPS.

After 24 hr, cells were fixed *in situ* to the surfaces of the HAP discs with Karnovsky's fixative (Polysciences) for 30 min, stained with 1% osmium tetroxide (Polysciences) for 1 hr,

dehydrated with a series of ethanol/water mixtures to 100% ethanol, and dried with hexamethyldisilazane (Polysciences). Dried samples were coated with 200 Å of gold-palladium and observed by SEM. For each surface, five random fields were recorded. The area of the cells was measured using Scion Images in units of μm^2 .

2.2.5.5. Cell Proliferation Assay

To observe the proliferation of osteoblasts on the different HAP surfaces, primary human osteoblasts (NHOst; Clonetics) were seeded at an initial density of 50 cells/ mm^2 , and incubated with Osteoblast Growth Medium (OGM; Clonetics) containing 0.1% ascorbic acid, 10% FBS and 0.1% antibiotic (OGM BulletKit; Clonetics) at standard cell culture conditions (37°C, humidified 5% CO_2 /95% air). Osteoblasts at population numbers 3–5 were used in this study. For the proliferation assay, samples were collected at 1 d, 3 d, 5 d, 7 d and 10 d with a sample size of $n = 3$ for each time point. Cells were fixed with 4% formaldehyde *in situ*. After fixation, HAP samples were stained with a fluorescent Hoechst dye (Polysciences), while TCPS and nTCPS surfaces were stained with Bradford Reagent (Sigma-Aldrich). An epi-flourescent microscope (365 nm excitation; 400 nm emission) was used to count the number of cells attached to the HAP surfaces in nine random fields per surface. An optical microscope was used to count the number of cells attached to the surface in nine random fields per surface for the cells stained with Bradford Reagent. The average cell count per substrate was expressed as cell density in units of cells/ mm^2 .

2.2.5.6. Mineralization Assay

To observe the mineralization behavior of osteoblasts on the different surfaces, primary human osteoblasts (NHOst; Clonetics) were seeded at an initial density of 400 cells/ mm^2 [13-15] on Nano HAP, Poly HAP, TCPS and nTCPS. Cells were incubated with Osteoblast Growth Medium (OGM; Clonetics) containing 0.1% ascorbic acid, 10% FBS and 0.1% antibiotic (OGM BulletKit; Clonetics), and further supplemented with 0.1% hydrocortisone and β -glycerophosphate (Differentiation SingleQuots; Clonetics) to initiate mineralization at standard cell culture conditions (37°C, humidified 5% CO_2 /95% air). In addition, the medium was supplemented with 10 $\mu\text{g}/\text{ml}$ tetracycline (Aldrich) [16]. Osteoblasts at population numbers 3–5 were used in this study. For the mineralization assay, samples were collected at 1 d, 7 d, 14 d, 21 d and 28 d with a sample size of $n = 2$ for each time point. According to Clonetics, these human

osteoblasts are expected to stain positively for von Kossa and alkaline phosphates after 3 to 4 weeks.

At each time point, the medium was retained so that osteocalcin concentration could be measured by ELISA (Mid-Tact Osteocalcin Elisa Kit; Biomedical Technologies) [13]. HAP substrates were fixed with 4% formaldehyde and immunolabeled for F-actin and collagen I. F-actin was immunolabeled with Alexa Fluor 488 phalloidin (Molecular Probes) at a dilution of 1:200. Collagen I was labeled with a primary rabbit anti-collagen I antibody (Rockland) at a dilution of 1:100; a fluorescently labeled goat anti-rabbit secondary antibody (Alexa Fluor 594; Molecular Probes) was attached to the primary anti-collagen I antibody at a dilution of 1:400. Tetracycline contained in the medium was used to fluorescently label the mineralization deposits [16]. The mineralized nodules were visualized using epi-flourescent and confocal microscopy (Carl Zeiss Laser Scanning System LSM 510). The surface coverage of the mineralized deposits was calculated and expressed as mineralized area in units of μm^2 . TCPS and nTCPS substrates were stained for alkaline phosphatase (Sigma-Aldrich).

2.2.5.7. Statistical Analysis

Numerical data were analyzed using a standard analysis of variance (ANOVA) techniques; statistical significance was considered at $P < 0.05$.

2.3. Results and Discussion

2.3.1. Effect of Processing Conditions on the Precipitation and Sintering of HAP

For load-bearing applications, sintered HAP samples must be fully dense with ultrafine flaw sizes. To enhance ceramic sinterability, submicron, equiaxed and spherical particles are desired. Submicron particles have been shown to improve sintering kinetics [17], while uniform, equiaxed and spherical particles give rise to compacts with minimal density variations and reduced flaw sizes.

Although precipitation has been successfully applied to produce ultrafine, non-agglomerated oxides [18], this technique needs to be carefully developed for synthesizing HAP due to the complexity of this compound. Processing parameters, such as solution pH, aging time and temperature were examined to achieve non-agglomerated, ultrafine, equiaxed and spherical HAP particles. This section further discussed how the chemical and microstructural

characteristics of the precipitated HAP powders affected the thermal stability, sinterability, mechanical properties and bioactivity of the resulting bioceramic compacts.

2.3.1.1. Effect of Aging Time

Precipitated HAP powders were subjected to aging for 0, 10, 50 and 100 hr (samples A, B, C and D, respectively). Aging time affected the crystallinity and morphology of precipitates. Previous research suggested that the initial precipitate was an amorphous calcium phosphate (ACP), which underwent stages of aging to form a poorly crystalline apatitic phase, and then a fully crystallized HAP phase [19, 20]. While significant effort has been devoted to the chemistry of HAP formation, relatively little attention has been given to the subsequent maturation of the primary HAP crystals and their impact on material properties [21].

In our synthesis, as-precipitated material (sample A) could be crystallized upon calcination at 550°C (Table 2.2). It has the largest average particle size and crystallite size, and the lowest BET surface area compared to samples that were subjected to aging. The TEM micrograph in Figure 2.1(a) also illustrates that sample A has an irregular particle morphology. These physical properties and features were likely retained from the as-precipitated ACP phase. IR spectrum of sample A (Figure 2.2(a)) also showed a more intense OH⁻ peak (3569 cm⁻¹) and HPO₄²⁻ peak (633 cm⁻¹). These features were consistent with the higher levels of hydration and presence of HPO₄²⁻ associated with ACP [20, 21].

Table 2.2. Effect of aging time on HAP calcined at 550°C.

| Sample Name | Aging Time (hr) | Crystallite Size <002> (nm) | Crystallite Size <300> (nm) | Aspect Ratio <002>/<300> | Avg. Particle Size (μm) | BET Surface Area (m ² /g) | Ca/P Ratio |
|-------------|-----------------|-----------------------------|-----------------------------|--------------------------|-------------------------|--------------------------------------|------------|
| A | 0 | 76 | 23 | 3.3 | 2.26 | 64 | 1.68 |
| B | 10 | 56 | 23 | 2.4 | 0.84 | 76 | 1.65 |
| C | 50 | 53 | 19 | 2.8 | 0.96 | 93 | 1.67 |
| D | 100 | 57 | 20 | 2.9 | 0.91 | 88 | 1.67 |

The change in Ca/P ratio from 1.68 to 1.65 when aging time was increased from 0 to 10 hr and the change in the grain morphology shown in Figure 2.1 suggested that a solution-mediated dissolution process occurred, transforming ACP to HAP [20]. As the primary HAP nuclei began to convert the as-precipitated ACP, the emerging interfacial surfaces from the crystalline HAP phase acted as heterogeneous nucleation sites [19, 22]. Consequently, the surface area increased, the average particle size decreased, and the volume-averaged crystallite size along <002> plane decreased.

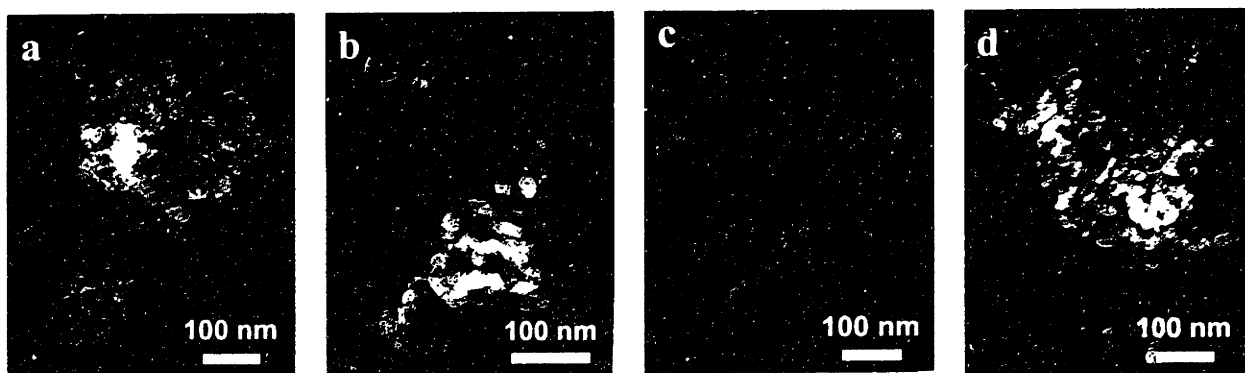


Figure 2.1. TEM micrographs illustrating 550°C-calcined HAP particles that were aged for (a) 0 hr, (b) 10 hr, (c) 50 hr, and (d) 100 hr.

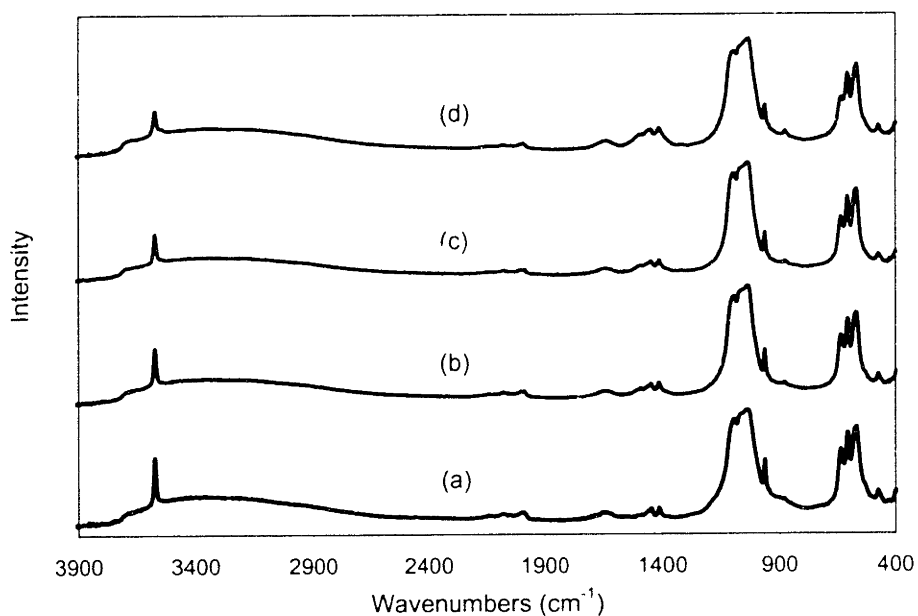


Figure 2.2. PA-FTIR spectra of 550°C-calcined HAP nanocrystals that were aged for (a) 0 hr, (b) 10 hr, (c) 50 hr, and (d) 100 hr.

When aging time was increased to 50 or 100 hr, the final stage of aging took place, yielding the Ca/P ratio for stoichiometric HAP (Table 2.2). The aspect ratios of the grains were changed to 2.8–2.9. Excellent surface areas were obtained for samples C and D. By harvesting samples after aging for at least 50 hr, we ensured that the precipitates have completely transformed into crystalline HAP and occluded impurities have been carefully removed.

Samples A–D were subjected to pressure-assisted sintering at 900°C for 30 min at 100 MPa. Sample A underwent significant HAP phase decomposition, as detected by XRD (Table 2.3). The SEM micrograph of the cross-section of this sintered specimen revealed an abundance

of irregularly shaped pores of $\sim 1 \mu\text{m}$ (Figure 2.3(a)), which could have resulted from HAP decomposition. As this sample was poorly developed structurally and chemically from lack of aging, it was thermally unstable and could not be properly densified.

Table 2.3. Effect of aging time on pressure-assisted sintered HAP.

| Sample Name | Aging Time (hr) | % Theoretical Density |
|-------------|-----------------|-----------------------|
| A | 0 | Decomposition |
| B | 10 | 96.4 |
| C | 50 | 95.8 |
| D | 100 | 98.5 |

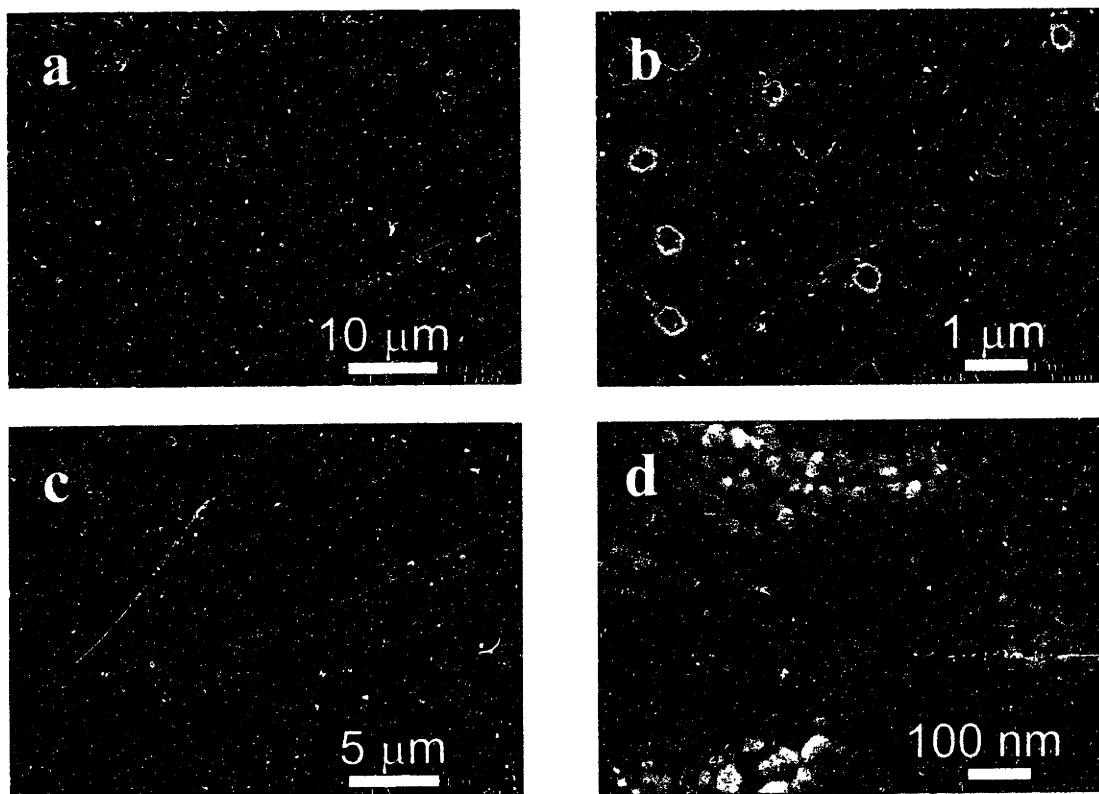


Figure 2.3. SEM micrographs of HAP samples (a) A, (b) B, (c) C and (d) D after pressure-assisted sintering at 900°C and 100 MPa.

The sintered specimens of samples B and C possessed spherical pores of 300–600 nm (Figures 2.3 (b) and (c)). These materials retained a pure HAP phase after pressure-assisted sintering, but they did not achieve $> 97\%$ of the theoretical density of HAP. The pore formation in samples B and C might be attributed to the dehydroxylation of HAP. At ambient pressures, reversible dehydroxylation might occur above $\sim 800^\circ\text{C}$ with loss of up to 75–80% of the total hydroxyl groups [23]. At higher temperatures, closed pores might form, and blow-holes would

appear as water was released irreversibly from the sintered compacts [23]. In contrast, sample D, which had been aged for 100 hr, attained an excellent density of 98.5% after pressure-assisted sintering at 900°C. The resulting compact was transparent, and retained an ultrafine microstructure with grain sizes below 100 nm (Figure 2.3(d)).

Our study indicated that sintering behavior and microstructural development of HAP depended on a combination of physical properties, phase stability, and thermal stability of the hydroxyl groups. HAP aged for less than 10 hr was susceptible to decomposition during sintering because of its poor structural development. While the thermal stability increased with longer aging time, the hydroxyls groups were still unstable in samples aged for 10–50 hr, resulting in spherical pore formation. By aging for 100 hr, a well-crystallized HAP with the desired chemical characteristics and the stability to withstand thermal decomposition and dehydroxylation could be obtained.

2.3.1.2. Effect of Initial Solution pH

The effect of precursor solution pH was examined at relatively low supersaturations, at room temperature, and at long aging times (see Table 2.1). These conditions resulted in longer induction times and increased ACP stability. Sample E was precipitated by adding an acidic calcium nitrate solution (pH = 6.1) to a basic ammonium phosphate solution (pH = 10.4). Sample D was obtained with two basic precursor solutions of matching pH (10.4). Sample F was prepared with calcium nitrate and ammonium phosphate solutions of high initial pH's of 11.8 and 11.0, respectively. As the initial solution pH increased, the crystallite size along the <002> axis increased, and the <002>/<300> aspect ratio increased (see Table 2.4). The particle size was also found to increase.

Table 2.4. Effect of initial solution pH on HAP calcined at 550°C.

| Sample Name | Solution pH | | Crystallite Size <002> (nm) | Crystallite Size <300> (nm) | Aspect Ratio <002>/<300> | Avg. Particle Size (μm) | BET Surface Area (m ² /g) | Ca/P Ratio |
|-------------|-------------|------|-----------------------------|-----------------------------|--------------------------|-------------------------|--------------------------------------|------------|
| | CaN | NHP | | | | | | |
| E | 6.1 | 10.4 | 44 | 19 | 2.3 | 0.59 | 84 | 1.72 |
| D | 10.4 | 10.4 | 57 | 20 | 2.9 | 0.91 | 88 | 1.67 |
| F | 11.8 | 11.0 | 75 | 23 | 3.3 | 3.05 | 68 | 1.74 |

By adding an acidic calcium nitrate solution to a basic ammonium phosphate solution as in the case of sample E, the solubility product, with respect to HAP or one of its intermediates, was massively exceeded and precipitation occurred almost instantaneously [18]. Thus, a large

number of crystallites could be nucleated with very little growth. As the initial solution pH increased, the extent to which the solubility product was exceeded would decrease, and the crystallite and particle sizes would grow to a greater extent after nucleation.

During the HAP synthesis under acidic conditions, a precipitate of dicalcium phosphate dihydrate (brushite, DCPD) could be formed without involving ACP as an initial phase [24]. In neutral solutions, hydrolysis of an octacalcium phosphate (OCP) precursor into a poorly crystalline apatite was observed [24], and an excess of acid phosphates might also be present on the crystal surface [22]. Thus, sample E's nonstoichiometry and the presence of more intense OH^- and HPO_4^{2-} IR peaks (Figure 2.4(a)) might be attributed to the remnants of DCPD or OCP intermediates formed during the development of HAP or from the shorter induction times at low pH's. These metastable intermediates were unlikely to form under the high pH conditions [25] of sample F. At $\text{pH} > 10.25$, kinetics of ACP transformation to HAP was known to increase very rapidly [25]. Thus, the very short induction time at high pH's would result in defective HAP crystallites, as noted in sample F.

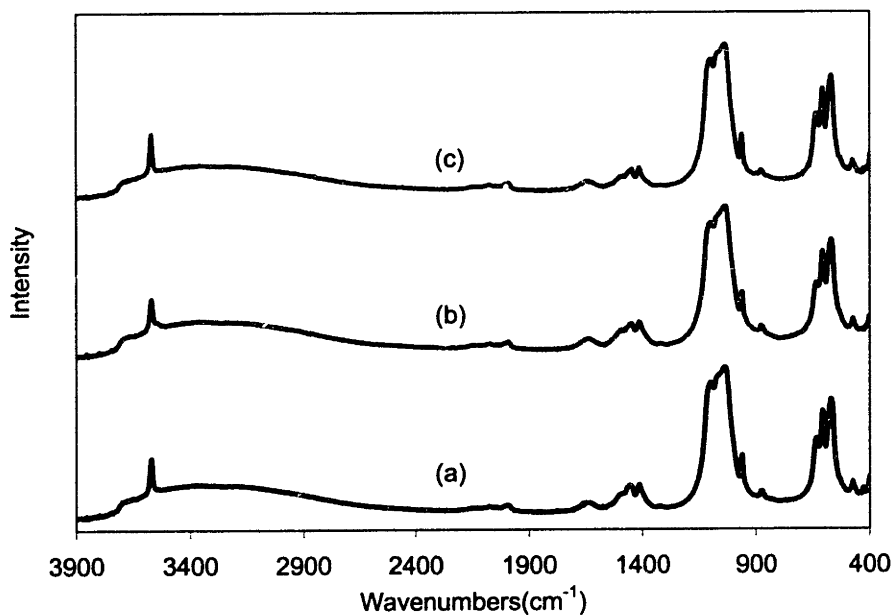


Figure 2.4. PA-FTIR spectra of 550°C-calcined HAP samples (a) E, (b) D and (c) F.

Low and high pH conditions resulted in the dehydroxylation of samples E and F after pressure-assisted sintering at 900°C and 100 MPa. XRD patterns of these sintered specimens showed some minor HAP phase decomposition, and the presence of a small secondary phase of

tricalcium phosphate (Table 2.5). SEM micrographs of these samples illustrated the presence of many irregularly shaped, submicron-sized pores (Figures 2.5(a) and 2.5(c)). In addition to the irregularly shaped pores from HAP phase decomposition, there were spherical pores resulting from dehydroxylation. Compared to sample E (Figure 2.5(a)), sample F possessed more porosity (Figure 2.5(c)), indicating the HAP synthesized at high pH's has a greater propensity to dehydroxylate and decompose than that derived under acidic conditions. Dehydroxylation could also be related to the stoichiometry of the HAP materials. Samples E and F possessed Ca/P ratios of 1.72 and 1.74, respectively (Table 2.4). The phosphate group deficiency might have resulted in a greater incorporation of hydroxyl groups to maintain charge balance within the crystal structure; more dehydroxylation could thus occur readily in these two nonstoichiometric HAP samples during sintering.

Table 2.5. Effect of initial solution pH on pressure-assisted sintered HAP.

| Sample Name | Solution pH | | % Theoretical Density |
|-------------|-------------|------|-----------------------|
| | CaN | NHP | |
| E | 6.1 | 10.4 | 98.5* |
| D | 10.4 | 10.4 | 98.5 |
| F | 11.8 | 11.0 | 97.1* |

* A small XRD peak of tricalcium phosphate was detected.

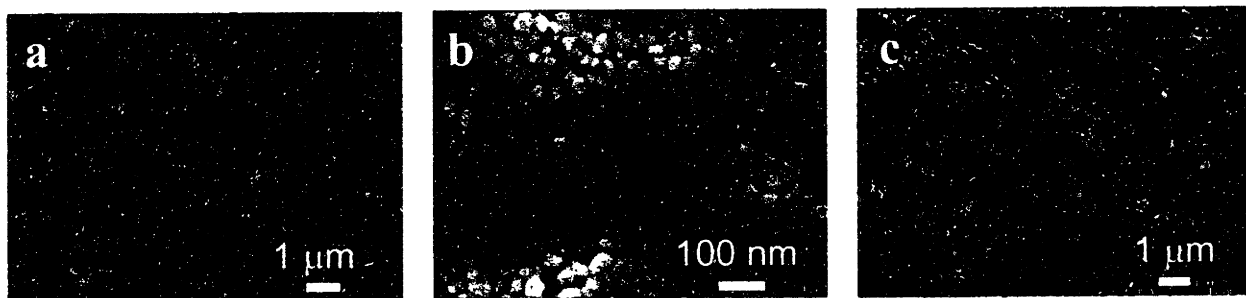


Figure 2.5. SEM micrographs of HAP samples (a) E, (b) D and (c) F after pressure-assisted sintering at 900°C and 100 MPa.

A stoichiometric Ca/P ratio was obtained only for sample D, which was prepared under a matching basic pH of 10.4. This sample was also shown to possess the least intense OH⁻ and HPO₄²⁻ infrared peaks compared to samples E and F (see Figure 2.4). It successfully attained full densification during pressure-assisted sintering, yielding a transparent bioceramic compact with grain sizes of < 100 nm (Figure 2.5(b)). This study illustrates that the initial solution pH's were critical to the chemical composition and thermal stability of HAP powder precipitated. These

factors in turn affect the sinterability and phase stability of the ceramic compacts during densification.

2.3.1.3. Effect of Aging Temperature

The effect of increasing the aging temperature was to decrease the induction time by both increasing the ACP solubility and providing additional energy to form a stable primary HAP nucleus [20]. HAP crystallization could be greatly accelerated by aging at a high temperature [19]. Aging temperature could also affect the solubility of the precursor salts. As temperature was increased, precipitation would occur at a lower supersaturation, resulting in fewer nuclei and larger particles.

To examine the effect of aging temperatures, samples G, D and H were precipitated from matching precursor solution pH's of 10.4, and were aged for 100 hr at 0°C, 25°C and 100°C. Sample G possessed a large <002>/<300> aspect ratio (Table 2.6), a very large particle size of 3.38 μm , an irregular particle morphology (Figure 2.6(a)), and a relatively low surface area. These characteristics are similar to those of sample A, which was aged for 0 hr, and the results can be explained in a similar manner. Despite the low aging temperature, large primary nuclei of HAP was able to form in sample G. However, further secondary heterogeneous nucleation did not occur, resulting in the large particle size and low surface area. Furthermore, the Ca/P ratio was only 1.44, indicating that the low aging temperature hindered structural development. The poorly developed HAP crystallinity was further confirmed by the broadening of the infrared phosphate bands to encompass 700–1300 cm^{-1} (Figure 2.7(a)).

Table 2.6. Effect of aging temperature on HAP calcined at 550°C.

| Sample Name | Aging Temperature (°C) | Crystallite Size <002> (nm) | Crystallite Size <300> (nm) | Aspect Ratio <002>/<300> | Avg. Particle Size (μm) | BET Surface Area (m^2/g) | Ca/P Ratio |
|-------------|------------------------|-----------------------------|-----------------------------|--------------------------|--------------------------------------|--|------------|
| G | 0 | 83 | 19 | 4.4 | 3.38 | 52 | 1.44 |
| D | 25 | 57 | 20 | 2.9 | 0.91 | 88 | 1.67 |
| H | 80 | 200 | 33 | 6.1 | 0.90 | 52 | 1.65 |

By precipitating at higher temperatures, crystal growth rate could be increased along specific crystal axes, resulting in larger, elongated crystals. This was illustrated in sample H, which was aged at 80°C. The average particle size of sample H was similar to that of sample D, but the surface area of the former was substantially lower due to the very large <002>/<300>

aspect ratio. Aging at 25 °C resulted in the smallest crystallite size and the highest surface area. It also gave rise to the desired HAP stoichiometry.

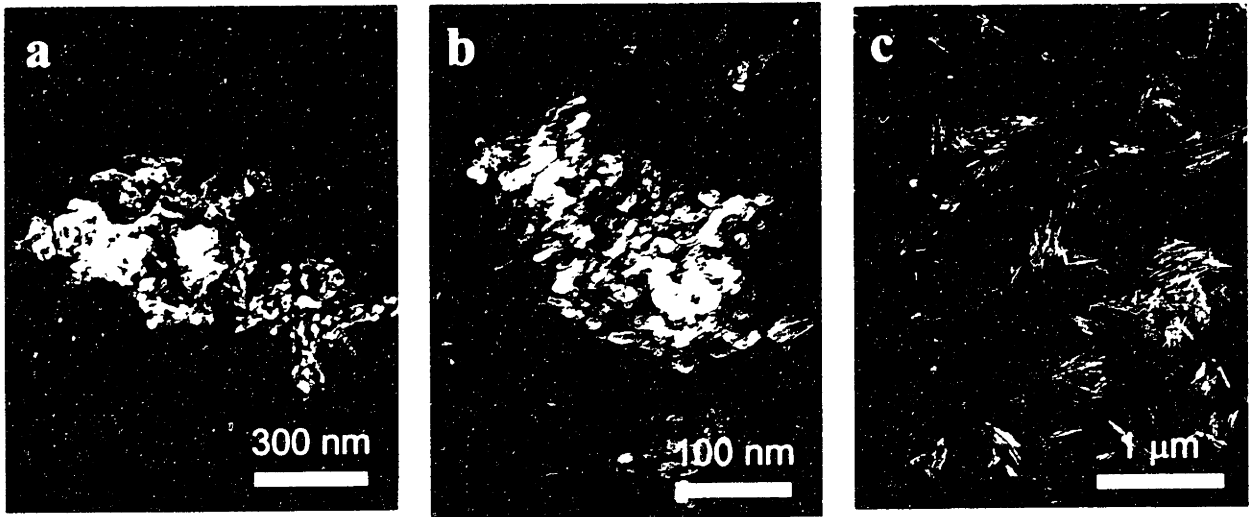


Figure 2.6. TEM micrographs illustrating 550°C-calcined HAP particles that were aged at (a) 0°C, (b) 25°C and (c) 80°C.

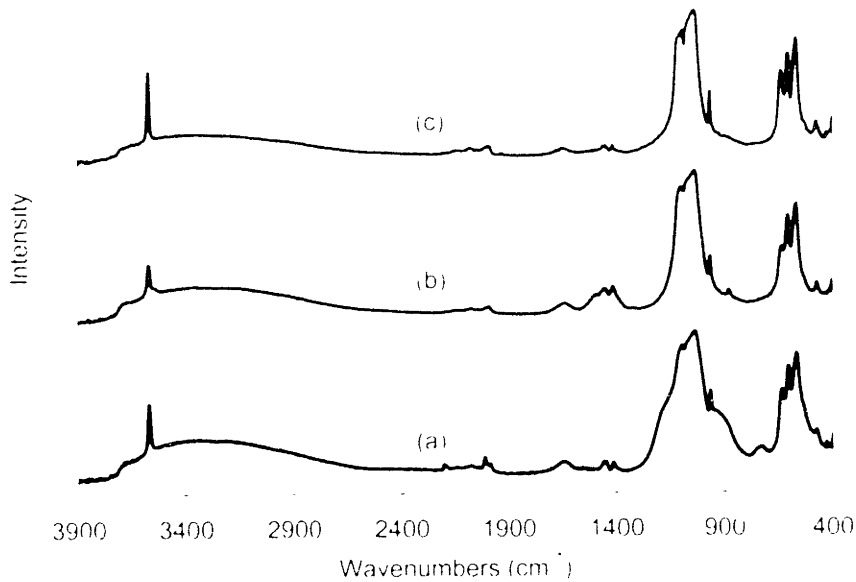


Figure 2.7. PA-FTIR spectra of 550°C-calcined HAP particles that were aged at (a) 0°C, (b) 25°C and (c) 80°C.

Sample G attained full densification, but its nonstoichiometry and poor structural development led to complete transformation to tricalcium phosphate (TCP) during pressure-assisted sintering. The sintered specimen was transparent, and consisted of coarse grains of ~ 1

μm (Figure 2.8(a)). In contrast, sample D retained a pure HAP phase and an ultrafine microstructure after densification (Figure 2.8(b)). Sample H also retained an ultrafine grain size upon sintering, but its microstructure was dominated by pores on the order of 100–200 nm (Figure 2.8(c)). This might be related to the packing of elongated particles in the starting powder. A small amount of TCP was found in sample H after sintering.

Table 2.7. Effect of aging temperature on pressure-assisted sintered HAP.

| Sample Name | Aging Temperature (°C) | % Theoretical Density |
|-------------|------------------------|-----------------------|
| G | 0 | Decomposition |
| D | 25 | 98.5 |
| H | 80 | 97.3* |

* A small XRD peak of tricalcium phosphate was detected.

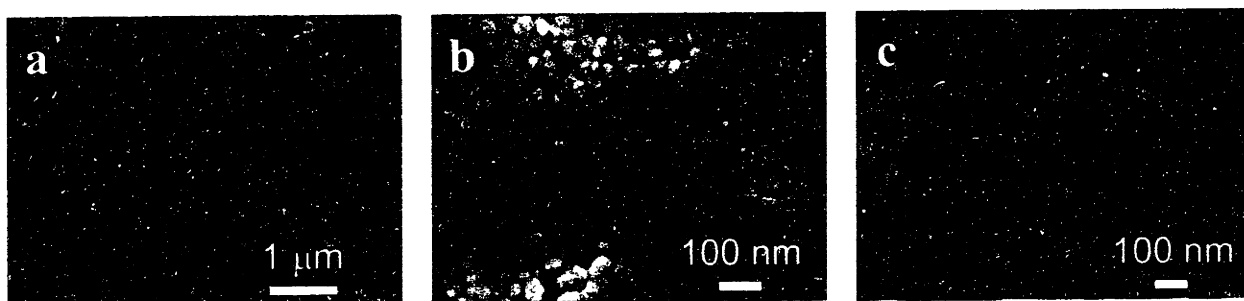
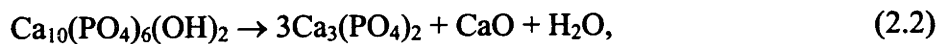


Figure 2.8. SEM micrographs of HAP samples (a) G, (b) D and (c) H after pressure-assisted sintering at 900°C and 100 MPa.

2.3.2. Sintering Behavior of Nanostructured Hydroxyapatite

Fully dense and transparent HAP has been difficult to obtain by traditional powder processing and sintering routes. Previous researchers have obtained a highly translucent specimen by sintering a dried filter cake at 1100°C for 1 hr. This material was 99.6% dense and has a grain size of 284 nm [10, 26]. A dried filter cake of HAP, processed by Jarcho *et al.*'s method [26] with the addition of argon sparging, has been HIPed between 800°C and 1000°C for 2 hr at 100 MPa to achieve a transparent specimen with grains of ~100 nm [10, 27]. Commercial HAP powders (Merck A.G., Darmstadt, Germany) have been colloiddally pressed and sintered at 1250°C to yield compacts of 96–98% theoretical density, with a grain size of 5 μm and a flexural strength of 125 MPa [10, 28]. Microwave sintering at 1100°C and conventional pressureless sintering at 1150°C of dried filter cakes or hydrothermally treated HAP have also resulted in translucent specimens, but these samples were only 1–2 mm in thickness [10].

Although Jarcho *et al.* [26] and other researchers have been able to obtain a fully densified HAP with a relatively fine grain size, they were only able to achieve that by drying and sintering a filter cake or by HIPing. Through careful control of processing parameters, we have shown that the powder stoichiometry, crystallinity, grain size and particle morphology could be tailored so that HAP powders of superior quality could be achieved. These nanostructured HAP samples were subjected to pressure-assisted sintering and pressureless sintering. Compared to other researchers, we were able to use mild sintering conditions to attain fully densified HAP with minimal grain growth. This ease of sintering was associated with the attractive characteristics of our HAP powder. Figure 2.9(a) illustrates that sample D underwent full densification by 900°C under pressure-assisted sintering at 100 MPa, while retaining an ultrafine grain size of < 100 nm. Temperatures of 1000°C or higher were shown to lead to rapid grain growth, as well as reduction in density due to HAP phase decomposition (Figure 2.9(b)),



which was induced by the vacuum/reducing atmosphere involved in the pressure-assisted sintering. Thus, the best pressure-assisted sintering temperature was 900°C for our optimized HAP sample; this was a relatively low temperature compared to conditions required for HAP sintering in previous studies. To illustrate the differences in the sinterability and phase stability of nanocrystalline HAP and conventional HAP, sample D and commercial HAP (Aldrich) were examined by SEM after pressure-assisted sintering at 900°C. Figures 2.10(a) and (b) illustrate the high porosity in the resulting commercial HAP compact, and the presence of TCP and calcia decomposition products, respectively. In contrast, sintered sample D possessed a defect-free microstructure at high magnification (Figure 2.10(c)) and ultrafine grains of < 100 nm (Figure 2.10(d)).

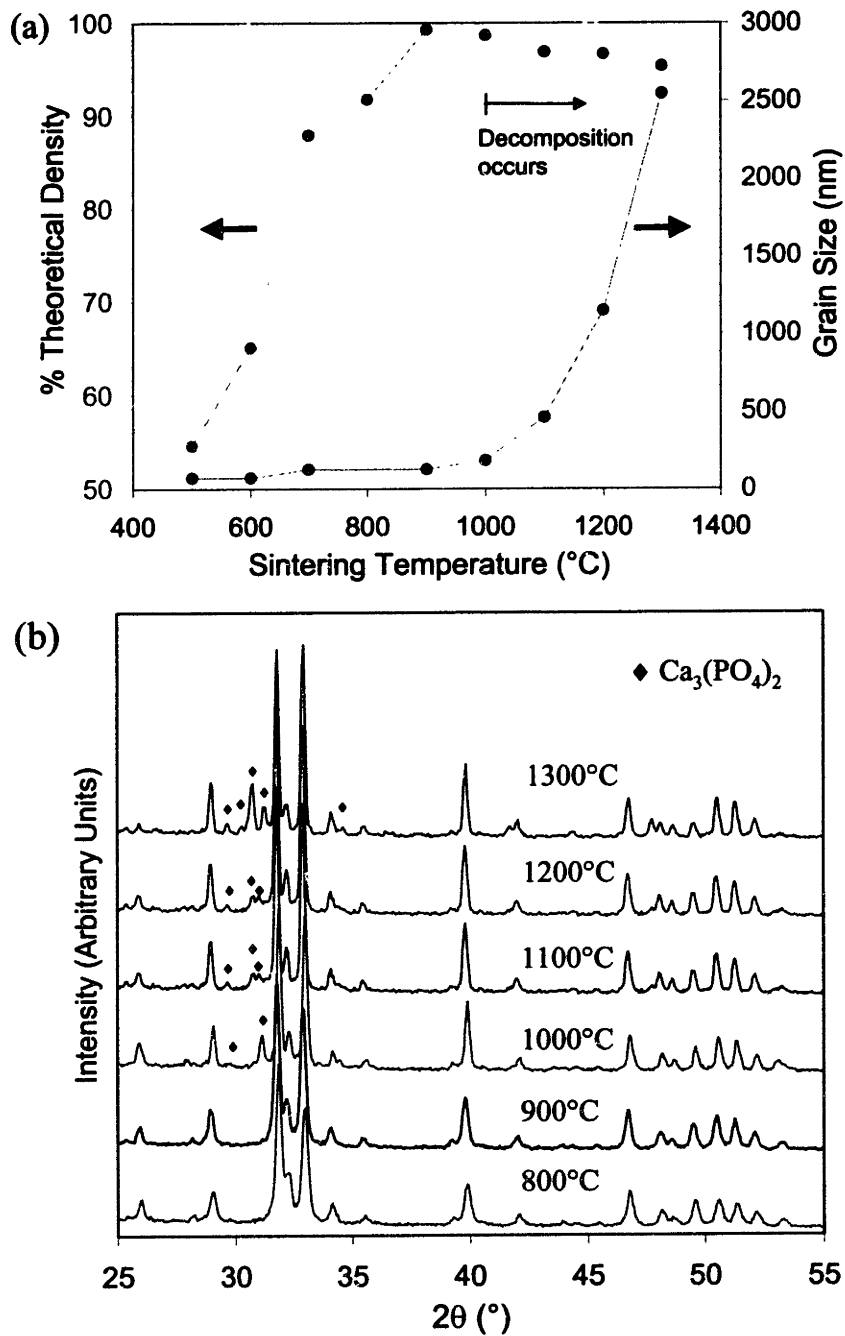


Figure 2.9. Effect of sintering temperature on (a) densification and grain size measured by SEM, and (b) XRD phase composition of HAP sample D in pressure-assisted sintering at 100 MPa.

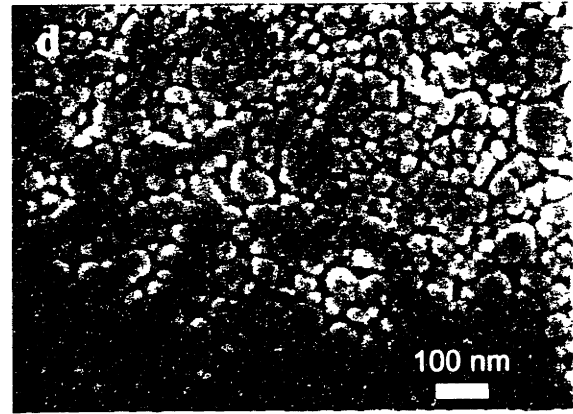
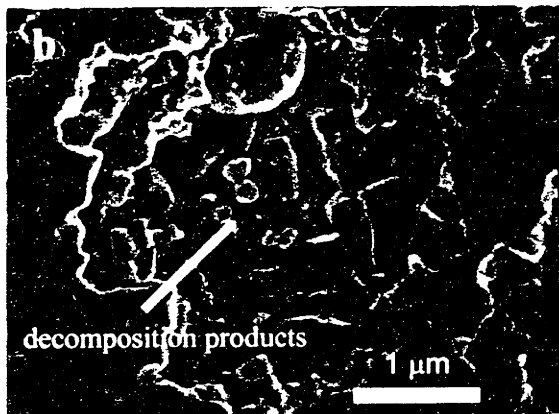
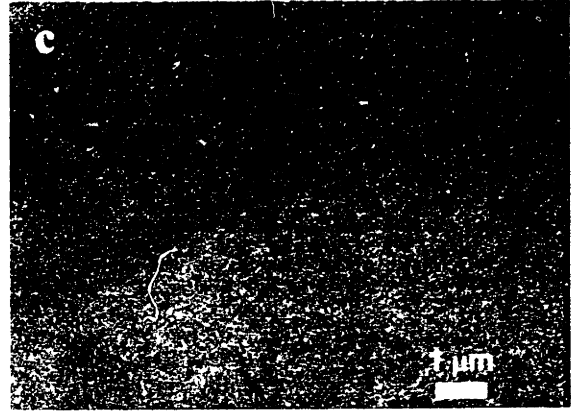
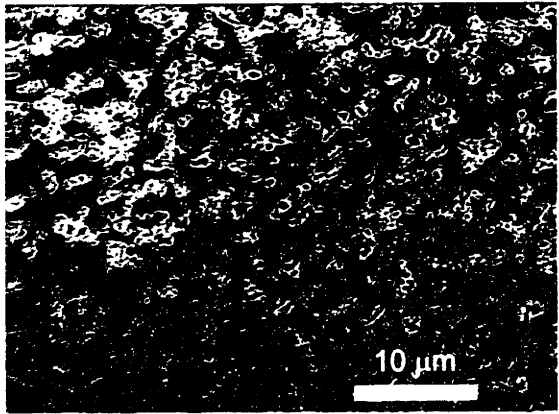


Figure 2.10. SEM micrographs of polished cross-sections of (a,b) commercial HAP and (c,d) nano-crystalline HAP (sample D), after pressure-assisted sintering at 900°C and 100 MPa.

Nano-crystalline HAP also demonstrated enhanced densification under pressureless sintering. A fully dense, translucent specimen of sample D was obtained by 1000 °C, which was 100 °C lower than that required by the best system reported in literature [11] (see Figure 2.11(a)). XRD studies further indicated that sample D possessed excellent thermal stability, with no phase decomposition even at 1300 °C under pressureless sintering conditions (see Figure 2.11(b)).

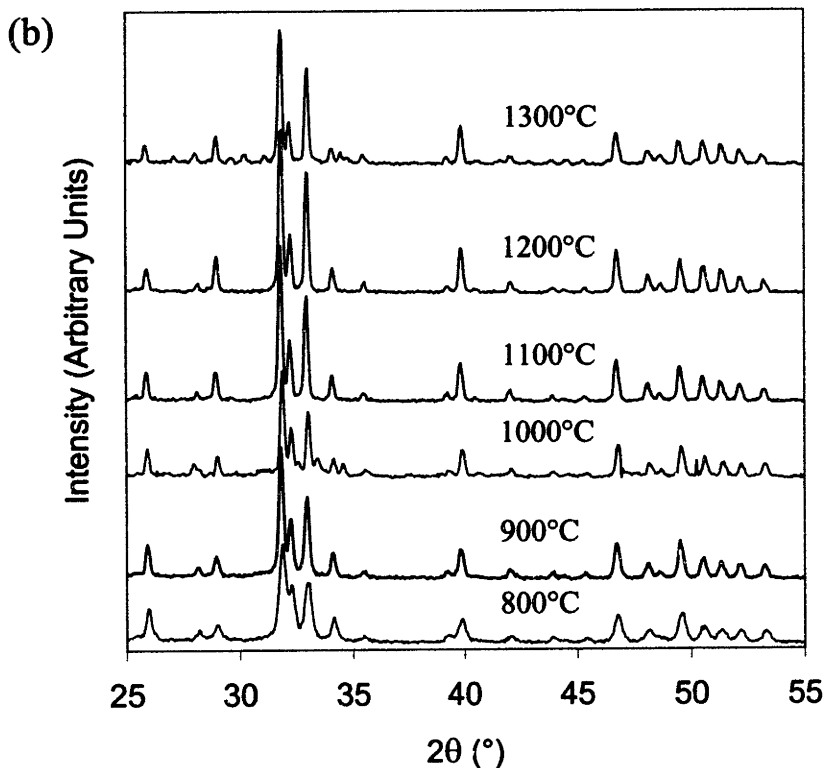
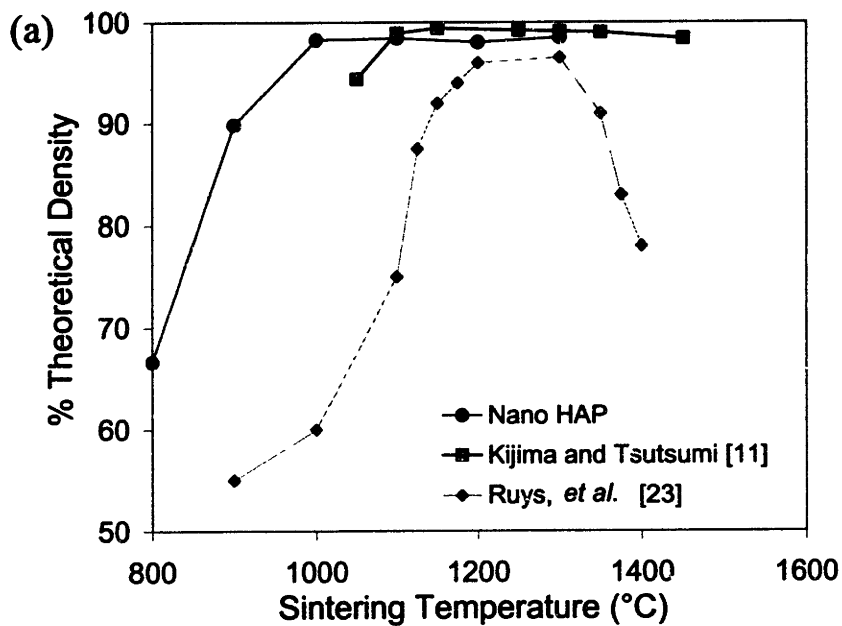


Figure 2.11. Effect of pressureless sintering temperature on (a) densification of nanocrystalline HAP (sample D) and literature HAP samples [11, 23], and (b) XRD phase composition of nanocrystalline HAP (sample D).

2.3.3. Mechanical Properties of Nanostructured Hydroxyapatite

Mechanical failure in a brittle ceramic occurs when the stress concentration at a critical flaw is exceeded. Thus, the size and number of such flaws must be reduced to improve mechanical strength of the material. In the case of HAP, nanostructure processing has resulted in a phase-pure and thermally stable material with nanometer-sized grains. The resulting material would undergo facilitated sintering without phase decomposition. By allowing fully dense bioceramics to be achieved at relatively low temperatures, nanocrystalline HAP compacts were able to retain its ultrafine microstructure without significant grain growth. The resulting system has reduced flaw sizes, a uniform microstructure consisting of crystalline HAP grains and grain boundaries. Such HAP ceramics should have superior strength and reliability to conventionally processed HAP ceramics, since the latter involved coarser grain sizes, phase decomposition and/or glassy interfaces (from the need of glassy sintering additives).

Nanostructured HAP (sample D) was tested for mechanical properties after pressure-assisted sintering at 900°C. Table 2.8 shows that the nanostructured compact has superb compressive and bending strengths and fracture toughness, compared to values reported in the literature for conventional HAP. Sample D's microstructure and phase purity could be credited for its superior strength compared to conventional HAP, dental enamel and compact bone. Nanostructured HAP's excellent mechanical properties make it an exciting potential candidate as orthopedic and dental implant material.

Table 2.8. Mechanical properties of nanostructured HAP (sample D) compared to conventional HAP, dental enamel, and compact bone.

| | Compressive Strength (MPa) | Bending Strength (MPa) | Fracture Toughness (MPa • m ^{1/2}) |
|-------------------------------|-------------------------------|---------------------------|---|
| Nanostructured HAP | 879 | 183 | 1.3 |
| Conventional HAP [†] | 120-800 | 38-113 | 1.0 |
| Dental Enamel [‡] | 95-370 | 76 | - |
| Compact Bone [‡] | 170-193 | 160 | 2-12 |

[†] Ref [23, 28-30].

[‡] Ref [29].

2.3.4. Cell Culture Studies

The microstructure of bone, in addition to providing mechanical support, also provides a scaffold to regulate its population of cells. The features that these cells encounter are largely nanometer in length scale, suggesting that this length scale is critical in regulating cell behavior. Bioactive materials such as Bioglass®, A/W glass-ceramics, β -tricalcium phosphate, or calcium sulfate rely upon composition and the solubility of that composition to bond with hard tissue, frequently sacrificing mechanical stability [1, 7, 31, 32]. Alternatively, nanocrystalline HAP monoliths can provide a structure that can enhance interactions with osteoblasts. Because the feature size and composition of nanocrystalline HAP are similar to that of bone, this microstructure may influence osteoblast adhesion, attachment, proliferation and mineralization. Previous research has shown that nanocrystalline alumina, zirconia and titania surfaces affected osteoblast attachment and proliferation [33, 34]. The objective of this study was to determine the effect of nanostructured HAP microstructures [35, 36] on osteoblast behavior during different time scales of interaction. Osteoblast attachment and adhesion were measured over very short time scales [37]. At intermediate time scales, osteoblast proliferation was evaluated. The extent of mineralization was determined over long time scales.

2.3.4.1. Surface Characterization of Dense Hydroxyapatite

Nano and Poly HAP surfaces were characterized to determine the surface microstructure, surface roughness, surface chemistry, and surface hydrophilicity (Table 2.9). Poly HAP possessed an average grain size of 5 μm while Nano HAP possessed an average grain size of 100 nm (Figure 2.12). The surface roughness, as measured by AFM, indicated the surfaces were relatively smooth. Furthermore, the surface Ca/P ratio, as determined by XPS, suggested that the surface chemistries between the two materials were quite similar. Consequently, the increased hydrophilicity (smaller contact angle) of Nano HAP relative to Poly HAP could be attributed mainly to the smaller average grain size and larger grain boundary volume. The larger grain boundary volume associated with Nano HAP may influence protein adsorption and their conformation on the HAP surface.

Table 2.9. Surface properties of Nano and Poly HAP.

| | Grain Size | Surface Roughness | Surface Ca/P Ratio | Contact Angle |
|----------|-----------------|-------------------|--------------------|---------------|
| Nano HAP | 100 nm | 3 nm | 1.32 | 58° |
| Poly HAP | 5 μm | 7 nm | 1.24 | 68° |

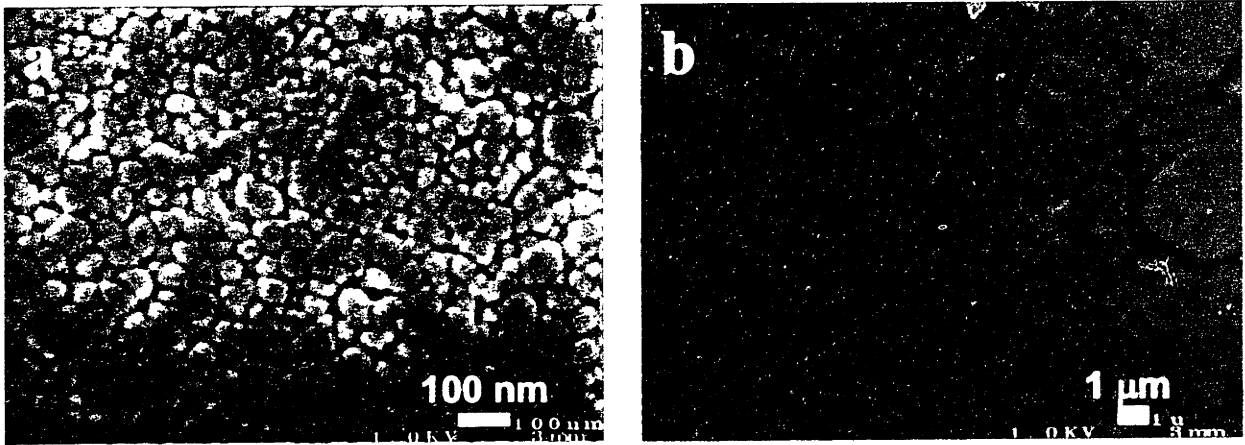


Figure 2.12. SEM micrographs comparing the microstructures of (a) Nano HAP and (b) Poly HAP.

2.3.4.2 Osteoblast Attachment to Nanostructured Hydroxyapatite

To evaluate the interaction of osteoblasts with HAP surfaces at short time scales, osteoblast attachment was investigated over a 24-hr period (Figure 2.13). Osteoblasts attached rapidly to TCPS, the positive control, while attaching poorly to nTCPS, the negative control. At 1 hr and 3 hr of incubation, osteoblasts attached quite similarly to Nano and Poly HAP. After 6 hr of incubation, the osteoblasts attached in greater numbers to Nano HAP. By 24 hr, Nano HAP had significantly more attached osteoblasts than Poly HAP. These results indicated that the nanocrystallinity of Nano HAP was an important parameter affecting osteoblast attachment. Furthermore, at least 12 hr of incubation were required before osteoblasts attached in statistically significant numbers to Nano HAP, suggesting that surfaces did not become saturated with cell adhesion proteins until after 12 hr.

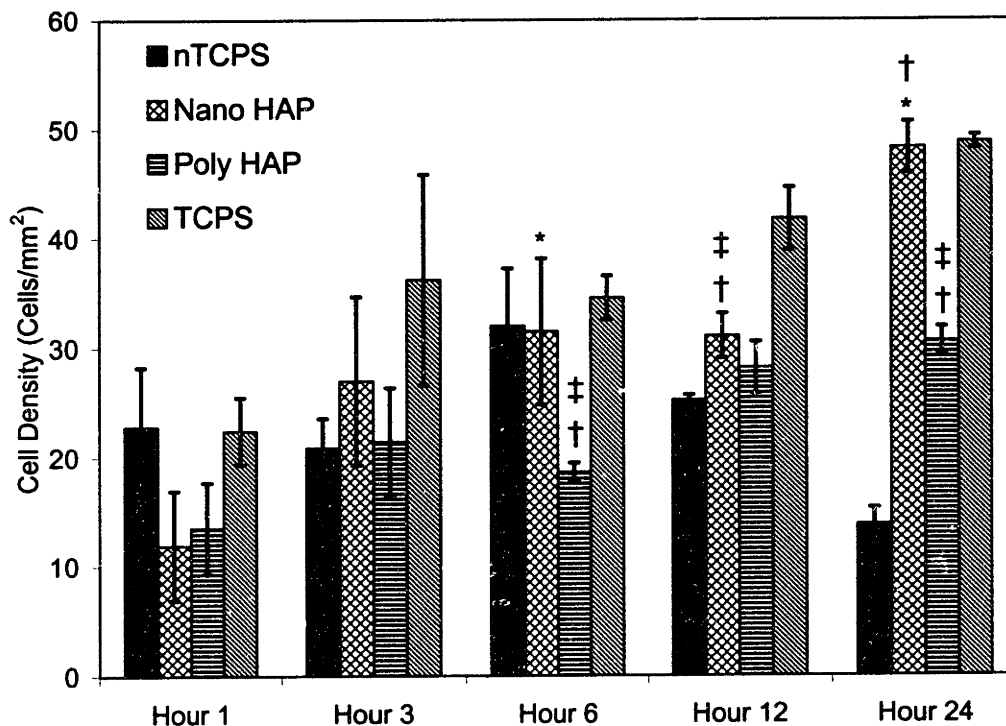


Figure 2.13. Attachment of primary human osteoblasts on different substrates. Values are mean \pm standard error of the mean. * $P < 0.05$ compared to Poly HAP. † $P < 0.05$ compared to nTCPS. ‡ $P < 0.05$ compared to TCPS.

2.3.4.3. Osteoblast Adhesion on Nanostructured Hydroxyapatite

The attachment behavior of osteoblasts on HAP surfaces was further evaluated based upon their adhesion, as measured by cell spreading, at the end of 24 hr. TCPS, the positive control, possessed the largest cell area while nTCPS, the negative control, possessed the smallest cell area. Most importantly, polycrystalline HAP microstructures resulted in a larger cell area than nanocrystalline HAP. We postulated that adhesion to Poly HAP increased cell area by decreasing the surface density of cell adhesion proteins, such as fibronectin, on the surface because of the coarser microstructures. Since cell adhesion proteins might adsorb along the grain boundaries, coarser microstructures would increase the distance between cell adhesion proteins, forcing cells to spread over greater distances to make contact with cell adhesion proteins. A smaller grain size would decrease the distance between cell adhesion proteins. Consequently, Nano HAP possessed a smaller cell area relative to Poly HAP.

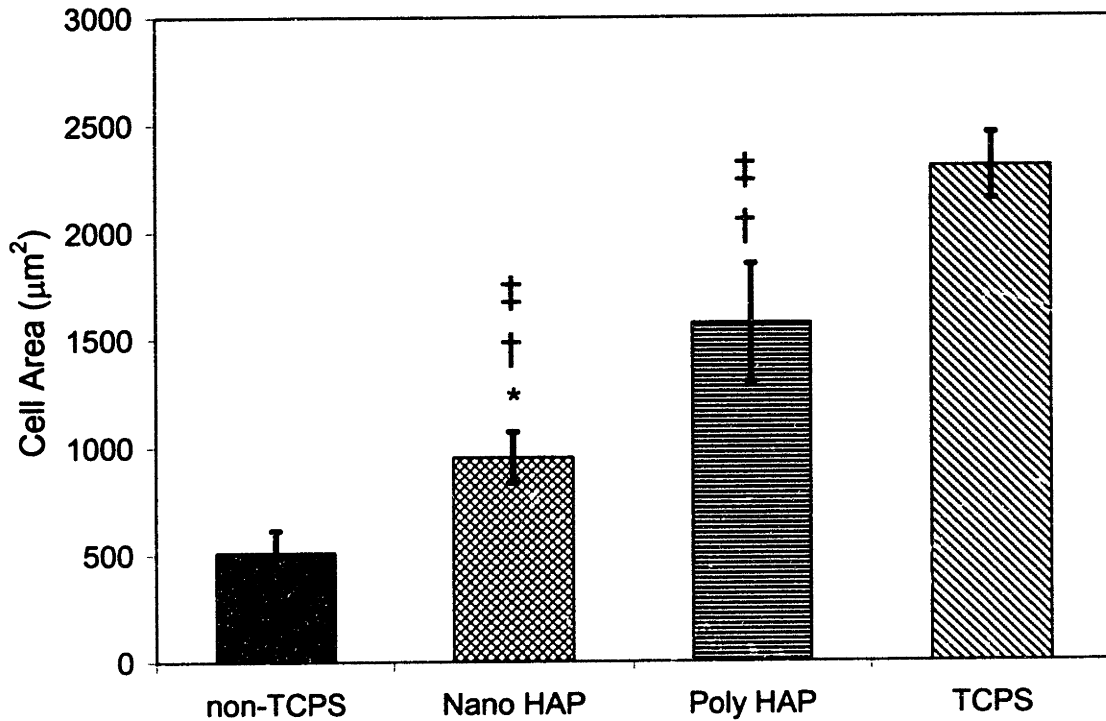


Figure 2.14. MC3T3 osteoblast cell adhesion on different substrates after 24 hr of incubation. Values are mean \pm standard error of the mean. * $P < 0.05$ compared to Poly HAP. † $P < 0.05$ compared to nTCPS. ‡ $P < 0.05$ compared to TCPS.

The substrates used in the cell adhesion assays also affected cell morphology. In Figure 2.15(a), MC3T3 osteoblasts minimized contact with the surface of nTCPS and adopted a globular morphology. On TCPS, osteoblasts were flattened and highly spread (Figure 2.14(d)). On Nano HAP, osteoblasts extended pseudopods (Figure 2.14(b)), unlike the osteoblasts on TCPS. On Poly HAP, osteoblasts also extended pseudopods, but over longer distances than on Nano HAP (Figure 2.14(c)). Hence, the coarser HAP microstructure increased the spatial distance between cell adhesion proteins, requiring cells to extend their pseudopods further to interact with adhesion focal points.

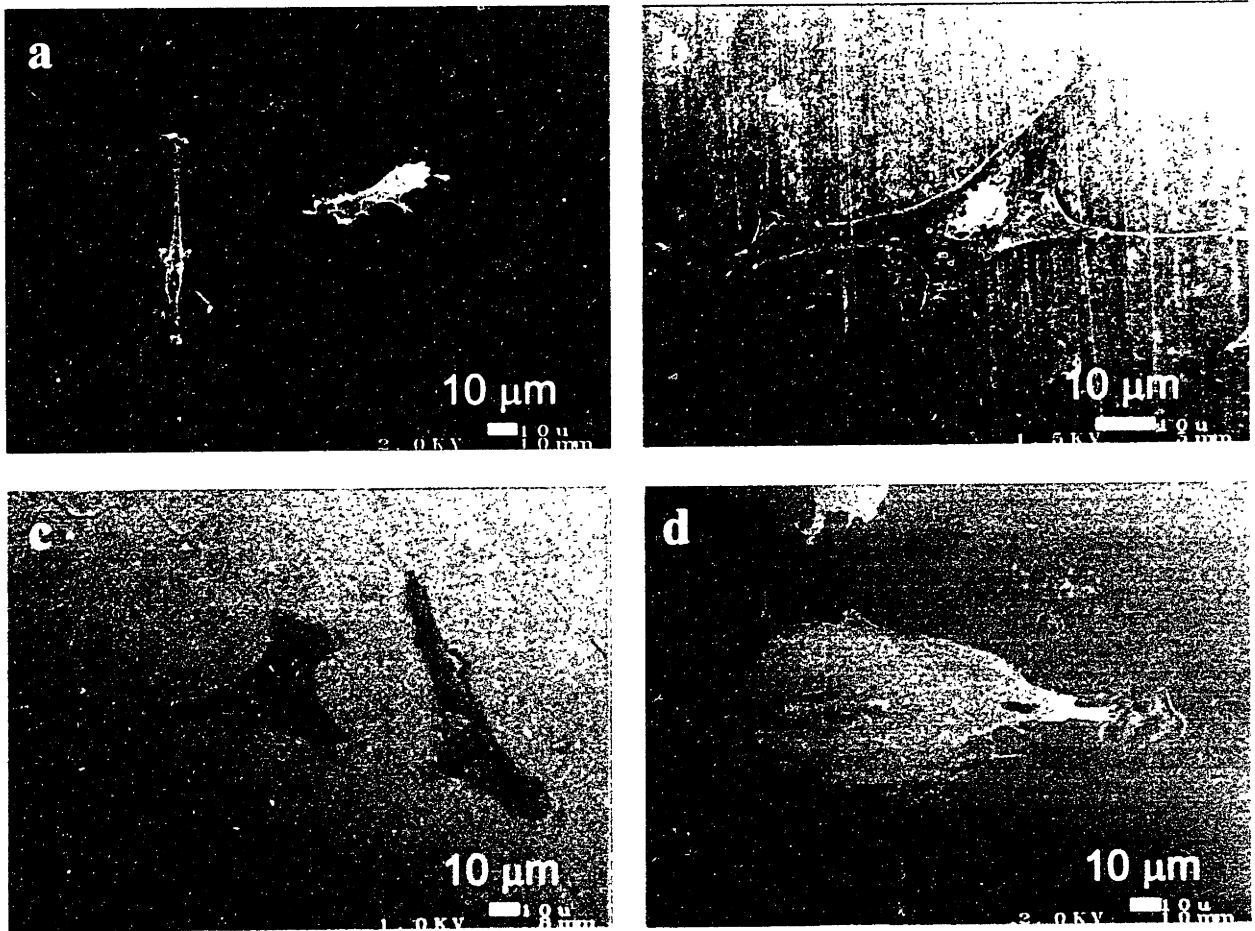


Figure 2.15. SEM micrographs of MC3T3 osteoblasts on (a) nTCPS, (b) Nano HAP, (c) Poly HAP, and (d) TCPS after 24 hr of incubation.

2.3.4.4 *Osteoblast Proliferation on Nanostructured Hydroxyapatite*

To evaluate the interaction of osteoblasts with HAP surfaces at intermediate time scales, osteoblast proliferation on the different substrates was measured over a 10-d period. Proliferation occurred slowly for the first four days and increased substantially after 5 d. Figure 2.16 showed that osteoblasts rapidly proliferated on TCPS, the positive control, and achieved confluency by 10 d. Osteoblasts proliferated very slowly on nTCPS, the negative control. The mean cell density on Nano HAP had exceeded Poly HAP by day 3. After 10 d, the mean cell density on Nano HAP was over 30% higher than that on Poly HAP. These results indicated that nanocrystallinity significantly influenced osteoblast proliferation. Due to the greater cell attachment on Nano HAP (Figure 3.13) and the smaller cell area occupied by osteoblasts on Nano HAP (Figure 2.14), a higher surface density and a greater proliferation of osteoblasts could be achieved over this nanocrystalline bioceramic than over its coarse-grained counterpart.

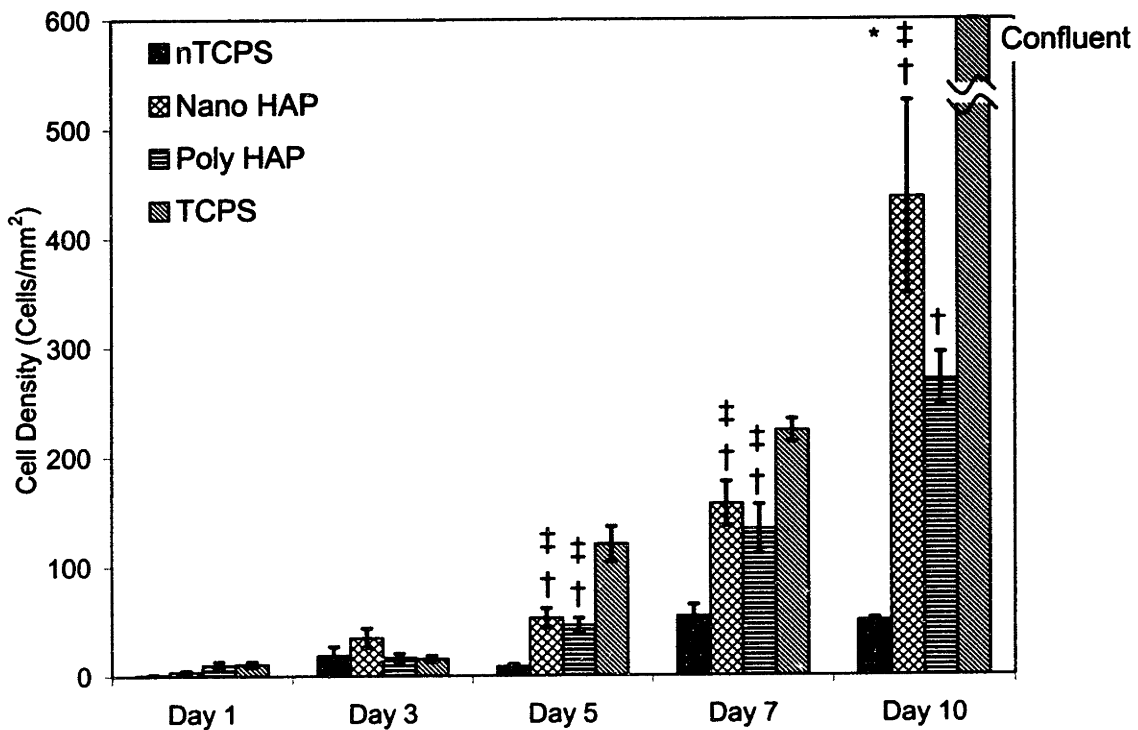


Figure 2.16. Proliferation of primary human osteoblasts on different substrates. Values are mean \pm standard error of the mean. * $P < 0.05$ compared to Poly HAP. † $P < 0.05$ compared to nTCPS. ‡ $P < 0.05$ compared to TCPS.

2.3.4.5. Osteoblast Mineralization on Nanostructured Hydroxyapatite

Mineralization was the osteoblast response that required the longest time to induce. To evaluate the effect of microstructure on osteoblast mineralization, primary human osteoblasts were cultured on Nano and Poly HAP, TCPS, and nTCPS for 28 d in a medium containing mineralization initiators, such as β -glycerophosphate and hydrocortisone [13-15, 38]. To determine whether the observed mineralization was attributed to the reprecipitation of calcium and phosphate ions solubilized from the surfaces of HAP substrates or was osteoblastic in origin, the presence of markers for the osteoblastic phenotype, such as osteocalcin and alkaline phosphatase, was determined. Osteocalcin is a noncollagenous matrix molecule abundantly excreted by postmitotic osteoblasts, but is undetectable in preosteoblasts [39]. Alkaline phosphatase is a cell surface protein that is required to breakdown the organophosphate, β -glycerophosphate, so that the phosphate group can react with free calcium ions [39]. Since the cells used in this assay were primary human osteoblasts, Figure 2.17 showed that osteoblasts secreted osteocalcin for the duration of the assay. While the osteoblasts were positive for

osteocalcin, the osteoblasts on the TCPS and nTCPS controls only stained positively for alkaline phosphatase at day 28. Hence, 28 d were required for the osteoblasts to fully express the mineralizing phenotype.

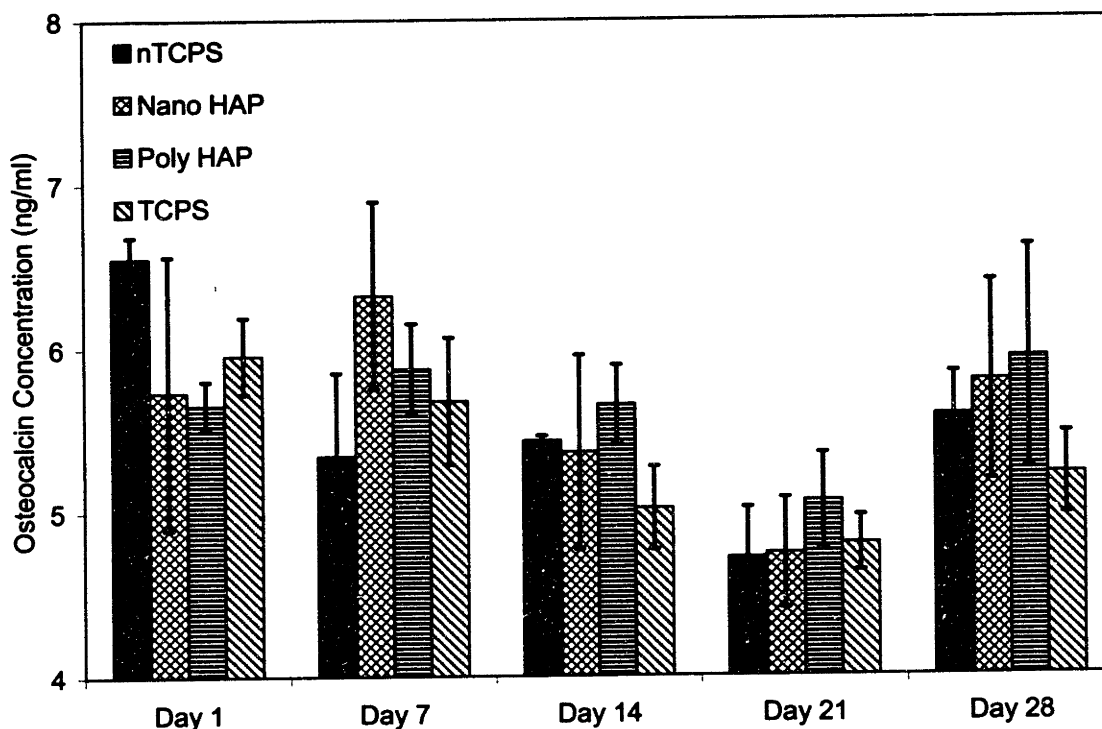


Figure 2.17. Osteocalcin concentration in the mineralizing medium for primary human osteoblasts incubated on different substrates. Values are mean \pm standard error of the mean. * $P < 0.05$ compared to Poly HAP. † $P < 0.05$ compared to nTCPS. ‡ $P < 0.05$ compared to TCPS.

Though the osteoblasts cultured on the TCPS and nTCPS controls stained negatively for alkaline phosphatase on day 21, mineralization was observed on Nano HAP and Poly HAP. By day 28, large mineralized nodules were observed on all HAP surfaces (see Figure 2.18). As shown in the micrographs, osteoblasts grew into a multilayer with a heavily collagenized cell layer closely opposed to the surface of HAP. The osteoblasts farthest from the surface stained positively for F-actin, and were not surrounded by a collagen extracellular matrix. The mineralized deposits were globular aggregations containing both collagen and calcium phosphates [16, 38] with the mineralized deposits ranging in diameter from 0.5 μm to 50 μm . The largest mineralized deposits were deeply embedded in the collagen-rich layer, whereas

smaller deposits were observed at the interface between the collagenized and the noncollagenized cell layers.

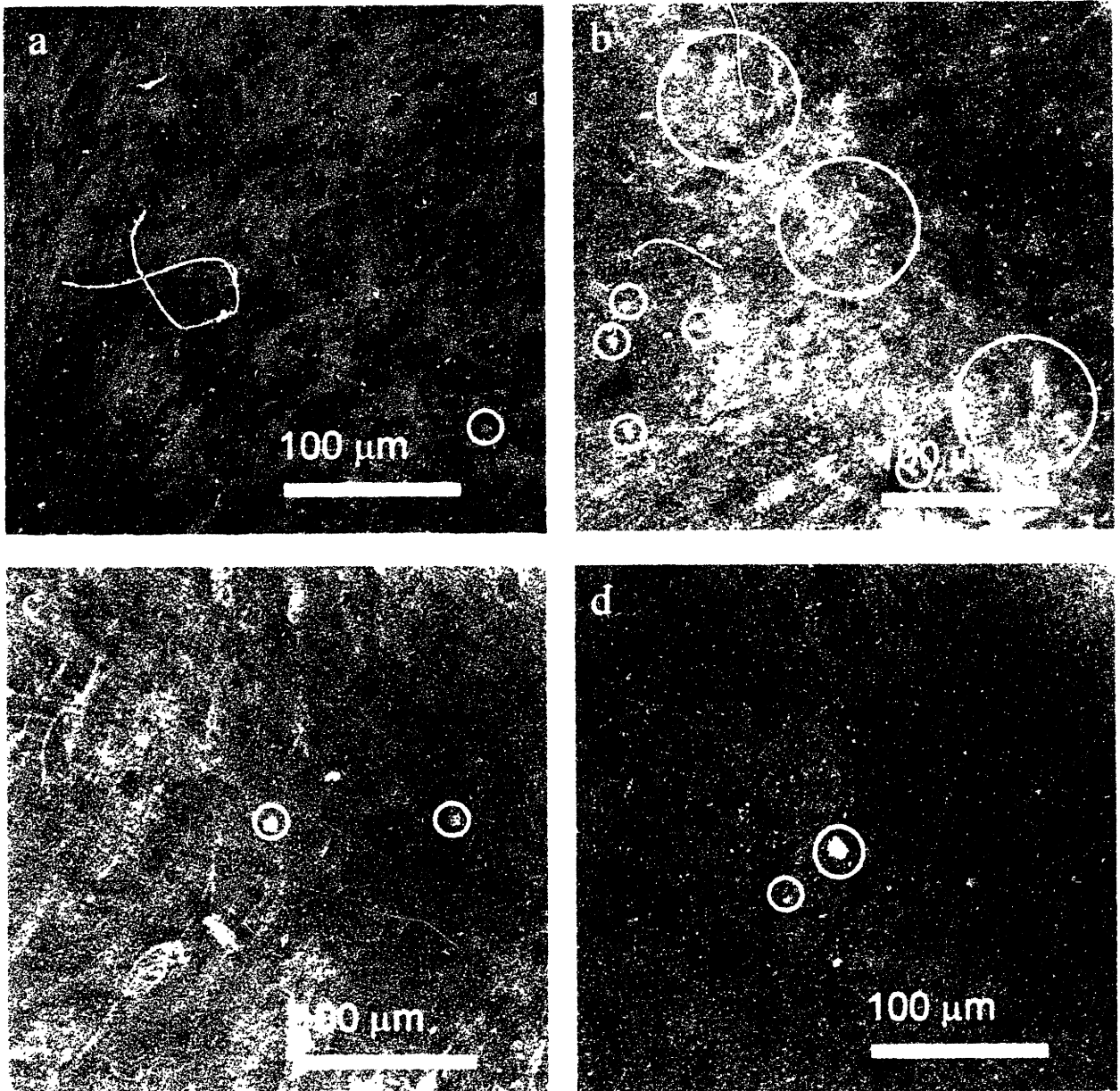


Figure 2.18. Laser scanning confocal micrographs of cell layers on HAP substrates at 28 d, where collagen I, F-actin, and mineralized deposits have been fluorescently labeled in (a) Nano HAP and (c) Poly HAP, and where only collagen I and mineralized deposits have been fluorescently labeled in (b) Nano HAP and (d) Poly HAP. Mineralized regions were contained within the white circles.

The area occupied by the mineralized deposits shown in Figure 2.18 were quantified, and the results are shown in Table 2.10. Mineralization occurred more readily on the surfaces of

Nano HAP than on the surfaces of Poly HAP. Figure 2.16 illustrated that osteoblasts on Nano HAP could achieve greater proliferation than on Poly HAP. Consequently, the larger number of osteoblasts on the surface of Nano HAP could account for the greater area of mineralization.

Table 2.10. Mineralized areas on Nano and Poly HAP substrates.

| | Mineralized Area (μm^2)* |
|----------|---------------------------------------|
| Nano HAP | 720 \pm 259 |
| Poly HAP | 291 \pm 54 |

* Values are mean \pm standard error of the mean.

2.4. Conclusions

We have demonstrated the versatility of nanostructure processing in controlling the chemistry and microstructural characteristics of a complex ceramic system, such as HAP. This approach successfully addressed many processing difficulties associated with HAP, allowing nanocrystalline grains of perfect stoichiometry and phase purity to be achieved. The nanocrystalline HAP powders obtained from controlled chemical precipitation could be easily sintered into fully dense, transparent ceramics, while retaining the ultrafine microstructure. Such nanostructured bioceramics possessed superior mechanical properties and bioactivity over conventional HAP, and could be applied potentially as load-bearing implants, bone grafts, dental replacements and bioactive coatings.

2.5. References

- [1] L. L. Hench, *J. Am. Ceram. Soc.* **74**, 1487 (1991).
- [2] "Total Hip Replacement, NIH Consensus Statement" (NIH, 1994).
- [3] L. L. Hench, E. C. Etheridge, *Biomaterials: An Interfacial Approach* (Academic Press, New York, 1982).
- [4] L. L. Hench, in *Bioactive Ceramics*, P. Ducheyne, J. Lemmons, Eds. (Annals of New York Academy of Sciences, New York, 1988), vol. 523, p. 24.
- [5] U. Gross, R. Kinne, H. J. Schmitz, V. Strunzve, *CRC Crit. Rev. Biocomp.* **4**, 155 (1988).
- [6] L. L. Hench, R. J. Splinter, W. C. Allen, T. K. Greenlee, Jr., *J. Biomed. Mater. Res.* **2**, 117 (1972).
- [7] L. L. Hench, *J. Am. Ceram. Soc.* **81**, 1705 (1998).

- [8] J. D. Santos, J. C. Knowles, R. L. Reis, F. J. Monteiro, G. W. Hastings, *Biomater.* **15**, 5 (1994).
- [9] Y. Fang, D. K. Agrawal, D. M. Roy, in *Hydroxyapatite and Related Materials*, P. W. Brown, P. Wenzil, B. C. Constantz, Eds. (CRC Press, Boca Raton, FL, 1994), p. 147.
- [10] Y. Fang, D. K. Agrawal, D. M. Roy, R. Roy, *Mater. Lett.* **23**, 147 (1995).
- [11] T. Kijima, M. Tsutsumi, *J. Am. Ceram. Soc.* **62**, 455 (1979).
- [12] K. Niihara, *J. Ceram. Soc. Jpn.* **99**, 974 (1991).
- [13] S. J. Peter, L. Lu, D. J. Kim, A. G. Mikos, *Biomater.* **21**, 1207 (2000).
- [14] R. T. Franceschi, B. S. Iyer, *J. Bone Min. Res.* **7** (1992).
- [15] J. Y. Choi, *et al.*, *J. Cell. Biochem.* **61**, 609 (1996).
- [16] J. E. G. Hulshoff, *et al.*, *J. Biomed. Mater. Res.*, **40**, 464 (1998).
- [17] C. Herring, *J. Appl. Phys.* **21**, 301 (1950).
- [18] M. J. Mayo, D. C. Hague, D.-J. Chen, *Mater. Sci. Eng.* **A166**, 145 (1993).
- [19] E. D. Eanes, I. H. Gillessen, A. S. Posner, *Nature* **208**, 365 (1965).
- [20] A. L. Boskey, A. S. Posner, *J. Phys. Chem.* **77**, 2313 (1973).
- [21] E. D. Eanes, J. L. Meyer, *Calcif. Tiss. Res.* **23**, 259 (1977).
- [22] J. D. Termine, R. A. Peckauskas, A. S. Posner, *Arch. Biochem. Biophys.* **140**, 318 (1970).
- [23] A. J. Ruys, *et al.*, *Biomater.* **16**, 409 (1995).
- [24] M. S.-A. Johnsson, G. H. Nancollas, *Crit. Rev. Oral Bio. Med.* **3**, 61 (1992).
- [25] J. L. Meyer, C. C. Weatherall, *J. Coll. Interf. Sci.* **89**, 257 (1982).
- [26] M. Jarcho, *et al.*, *J. Mater. Sci.* **11**, 2027 (1976).
- [27] K. Uematsu, M. Takagi, T. Honda, N. Uchida, K. Saito, *J. Am. Ceram. Soc.* **72**, 1476 (1989).
- [28] G. D. With, H. J. A. V. Dijk, N. Hattu, K. Prijs, *J. Mater. Sci.* **16**, 1592 (1981).
- [29] W. Suchanek, M. Yoshimura, *J. Mater. Res.* **13**, 94 (1998).

- [30] M. Akao, H. Aoki, K. Kato, *J. Mater. Sci.* **16**, 809 (1981).
- [31] L. L. Hench, *Curr. Opin. Solid State Mater. Sci.* **2**, 604 (1997).
- [32] L. L. Hench, *J. Biomed. Mater. Res.* **41**, 511 (1998).
- [33] T. J. Webster, R. W. Siegel, R. Bizios, *Biomater.* **20**, 1221 (1999).
- [34] T. J. Webster, C. Ergun, R. H. Doremus, R. W. Siegel, R. Bizios, *Biomater.* **21**, 1803 (2000).
- [35] Z. Schwartz, B. D. Boyan, *J. Cell. Biochem.* **56**, 340 (1994).
- [36] D. A. Puleo, A. Nanci, *Biomater.* **20**, 2311 (1999).
- [37] K. Anselme, *Biomater.* **21**, 667 (2000).
- [38] J. D. de Bruijn, I. van Brink, J. van Meer, P. Nijweide, Y. P. Bovell, in *Bioceramics*, J. Wilson, L. L. Hench, D. Greenspan, Eds. (Elsevier Science, Tarrytown, 1995), vol. 8, p. 97.
- [39] J. E. Aubin, F. Liu, in *Principles of Bone Biology*, J. P. Bilezikian, L. G. Raisz, G. A. Rodan, Eds. (Academic Press, New York, 1996), p. 143.

Chapter 3 – Hydroxyapatite-based Nanocomposites

3.1. Background and Motivation

Although composite engineering can increase the strength and toughness of ceramics, the processing of the HAP-based composite systems has been challenging. Conventional HAP-based composite involves a physical mixing of coarse aggregates of HAP and a secondary phase [1-9]. Thus, the resulting system often suffers from microstructural heterogeneity and poor phase dispersion. In the conventional composites, a substantial amount of the reinforcing phase such as alumina, zirconia, or silver, has to be employed in order to strengthen the HAP matrix. The presence of poorly dispersed secondary phases introduces large flaws and interfacial stability problems in the resulting HAP matrix, and lowers the biocompatibility of the system [10]. Sintering of conventional composites also requires very high temperatures and/or pressures, which may give rise to HAP phase decomposition. Decomposition products, such as β -tricalcium phosphate (β -TCP) and CaO, increase biodegradability and negatively impact the strength of the resulting composites [10].

To successfully process HAP-based composites, nanostructure processing is employed to provide for an ultrahigh dispersion of HAP and the secondary phase. This allows the HAP matrix to be strengthened with a minimal amount of secondary additives, so that it maintains high bioactivity and phase purity. The uniform microstructure with ultrafine grain size allows the HAP-based nanocomposite to be sintered more easily, without causing phase decomposition. The resulting nanocomposite possesses a much finer microstructure and reduced flaw sizes compared to conventional composite; it allows greater mechanical reliability and uniform toughening to be achieved for the HAP-based system.

In this chapter, secondary phases such as zirconia and silver are used to strengthen HAP in nanocomposite processing. These additives are chosen to be compatible with the processing and chemistry of HAP. Zirconia is employed to reinforce the HAP matrix through crack deflection and phase transformation toughening. Silver is incorporated to toughen the HAP matrix via mechanisms such as plastic deformation and crack bridging.

3.2. Experimental

3.2.1. Preparation of Hydroxyapatite-Zirconia Nanocomposite Powders

3.2.1.1. Zirconia Synthesis

Yttria-stabilized zirconia (YSZ) and unstabilized tetragonal zirconia (TZ) were used in the synthesis of HAP-zirconia nanocomposites. For YSZ synthesis, 3 mol% $Y(NO_3)_3 \cdot 4H_2O$ (Aldrich) was added to a 2.0 M aqueous solution of $ZrOCl_2 \cdot 8H_2O$ (Aldrich). 25 ml of the resulting solution was subsequently diluted to a 0.2 M solution with 225 ml ethanol, and added to a basic solution containing 100 ml of concentrated NH_4OH and 150 ml of ethanol. The precipitate was either allowed to age at 25°C for 24 hr to obtain an amorphous yttria-doped zirconium hydroxide gel, or was hydrothermally treated at 120°C for 3 hr to obtain crystalline yttria-stabilized tetragonal zirconia. For TZ synthesis, a similar procedure was followed without the 3 mol% yttria dopants.

3.2.1.2. HAP-Zirconia Nanocomposite Synthesis by a Colloidal Addition Technique

After hydrothermal treatment, YSZ or TZ was redispersed in 900 ml of 0.1 M $(NH_4)_2HPO_4$ (NHP; Fluka) at a pH of 10.4, and sonicated for 30 min. 900 ml of 0.167 M $Ca(NO_3)_2 \cdot 4H_2O$ (CaN; Fluka) with a pH of 10.4 was added at 3 ml/min to the 0.1 M $(NH_4)_2HPO_4$ /colloidal zirconia solution. The precipitate was magnetically stirred for 100 hr at 25°C. After aging, the white precipitate was washed successively with aqueous solutions of decreasing pH, followed by a series of ethanol washes. The gel was ground dry with a heated mortar and pestle. The powder was oven-dried at 120°C overnight, and then calcined in oxygen at 550°C for 2 hr (ramp = 10°C/min). HAP-based nanocomposites were prepared with various YSZ and TZ loadings, as shown in Tables 3.1 and 3.2, respectively.

Table 3.1. Conditions for the synthesis of HAP-YSZ nanocomposites.

| YSZ Content (wt %) [†] | Precursor Conc. [M] | | Aging Time (hr) | Aging Temperature (°C) | Solution pH | |
|------------------------------------|---------------------|-------|--------------------|---------------------------|-------------|------|
| | CaN* | NHP** | | | CaN | NHP |
| 0 | 0.167 | 0.1 | 100 | 25 | 10.4 | 10.4 |
| 1.5 | 0.167 | 0.1 | 100 | 25 | 10.4 | 10.4 |
| 3 | 0.167 | 0.1 | 100 | 25 | 10.4 | 10.4 |
| 8 | 0.167 | 0.1 | 100 | 25 | 10.4 | 10.4 |
| 12 | 0.167 | 0.1 | 100 | 25 | 10.4 | 10.4 |
| 15 | 0.167 | 0.1 | 100 | 25 | 10.4 | 10.4 |

[†]Concentration verified with chemical analysis.

*CaN = Ca(NO₃)₂•4H₂O.

**NHP = (NH₄)₂HPO₄.

Table 3.2. Conditions for the synthesis of HAP-TZ nanocomposites.

| TZ Content (wt %) [†] | Precursor Conc. [M] | | Aging Time (hr) | Aging Temperature (°C) | Solution pH | |
|-----------------------------------|---------------------|-------|--------------------|---------------------------|-------------|------|
| | CaN* | NHP** | | | CaN | NHP |
| 0 | 0.167 | 0.1 | 100 | 25 | 10.4 | 10.4 |
| 1.5 | 0.167 | 0.1 | 100 | 25 | 10.4 | 10.4 |
| 3 | 0.167 | 0.1 | 100 | 25 | 10.4 | 10.4 |
| 5 | 0.167 | 0.1 | 100 | 25 | 10.4 | 10.4 |
| 10 | 0.167 | 0.1 | 100 | 25 | 10.4 | 10.4 |
| 15 | 0.167 | 0.1 | 100 | 25 | 10.4 | 10.4 |

[†]Concentration verified with chemical analysis.

*CaN = Ca(NO₃)₂•4H₂O.

**NHP = (NH₄)₂HPO₄.

3.2.1.3. HAP-Zirconia Nanocomposite Synthesis by a Gel Mixing Technique

In this synthesis, HAP was first precipitated from adding 900 ml of 0.167 M Ca(NO₃)₂•4H₂O (pH = 10.4) to 900 ml of 0.1 M (NH₄)₂HPO₄ (pH = 10.4). It was then aged and subjected to aqueous and ethanolic washes as described in Section 3.2.1.2. The zirconia (3 wt%) was introduced as an amorphous zirconium hydroxide gel or a crystalline zirconia gel (see Section 3.2.1.1) to the HAP gel. The resulting gel composite of HAP and zirconia was redispersed in ethanol and ball-milled for 12 hr. It was then washed in ethanol and dried by grinding in a heated mortar and pestle. The powder was oven-dried overnight at 120°C, and calcined in oxygen at 550°C for 2 hr (ramp = 5°C/min).

3.2.2. Preparation of HAP-Silver Nanocomposite Powders

Nanocrystalline HAP powder was synthesized and calcined to 550°C according to the technique described in Section 3.2.1.2, without the zirconia additive. Silver powder (Alfa Aesar, 0.7–1.3 μm) was added to 10 g of HAP powder to form a mixture with a silver loading of 1, 2, 5, 10, 20 or 30 vol%. 100 ml of acetone were introduced to this dry HAP-silver mixture to form a slurry, which was ball-milled in a 1-liter polyethylene bottle with 100 g of 3-mm YSZ spheres

and 150 g of 7 mm x 7 mm YSZ cylinders. After 12 hr of ball-milling, the slurry was centrifuged and ground in a heated mortar and pestle. The composite powder was oven-dried overnight at 120°C. It was calcined to 400°C in oxygen (ramp = 5°C/min), and soaked in nitrogen for 2 hr.

3.2.3. Characterization of Nanocomposite Powders

Powder X-ray diffraction (XRD) patterns of calcined powders were obtained with a Siemens D5000 θ - θ diffractometer (45 kV, 40 mA, Cu K_{α}). Chemical analysis by inductively coupled plasma – atomic emission spectroscopy (ICP-AES) was performed using a Perkin-Elmer Plasma 40. Particle morphology was determined from transmission electron microscopy (TEM) images obtained with a JEOL 200CX or JEOL 2000 microscope at 200 kV.

3.2.4. Sintering Studies and Microstructure Characterization

Calcined HAP-based nanocomposite powders were densified by pressure-assisted sintering in a graphite vacuum furnace (Materials Research Furnace H-4.5x7-G-2000-V&G). About 2 g of nanocomposite powders were placed in 20-mm diameter graphite dies in the furnace, which was then evacuated and purged with dry nitrogen or argon three times to a final pressure of 3×10^{-2} mbar, whereupon a load was applied to the powder. HAP-zirconia powders were sintered at 1000°C (unless otherwise noted) for 30 min under a load of 50 MPa (ramp = 5°C/min). HAP-silver powders were sintered at 900°C for 30 min under a load of 100 MPa (ramp = 5°C/min).

Densities of these sintered pellets were measured by Archimedes' method using water. The theoretical densities of HAP, zirconia and silver were assumed to be 3.16 g/cm³, 5.89 g/cm³ and 10.5 g/cm³, respectively. The sintered HAP pellets were polished using a final 0.05- μ m γ -Al₂O₃ (Buehler), and lightly etched in 0.01 M lactic acid for 20 sec. These samples were then analyzed by XRD and scanning electron microscopy (SEM). For the SEM studies, a 50 Å-thick coating of gold-palladium was deposited onto the sample surface to prevent charging under the electron beam, and a JEOL 6320 field emission gun scanning electron microscope (FEGSEM) was employed. By configuring the SEM to detect only backscattered electrons (BSE), a differentiation can be made between nuclei of different atomic numbers. Atoms of a higher atomic number have a larger nucleus, and thus backscatter a greater percentage of electrons and

appear significantly brighter. This allows us to distinguish the presence of zirconia and silver phases in the hydroxyapatite matrix in the backscattered SEM images of nanocomposites.

3.2.5. Mechanical Testing of Nanocomposites

Compressive and 3-point bending strengths were measured with an Instron Series 1125 Universal Test Instrument. For ultimate point compressive strength, tests were performed on 2 mm x 4 mm x 10 mm bars at a crosshead speed of 0.05 in/min with a 20,000-lb_f load cell. For ultimate point 3-point bending strength, tests were performed on 2 mm x 4 mm x 20 mm bars at a crosshead speed of 0.005 in/min with a 1,000-lb_f load cell. The span of the 3-point bending fixture was set at 15 mm. Data from the 3-point bending tests were evaluated using ASTM C1161-94.

Sintered pellets were polished to a P4000 SiC grit, and tested for Vickers hardness using a LECO DM-400 instrument. A force of 200 g_f was applied for 10 sec to obtain an indentation.

3.3. Results and Discussion

3.3.1. HAP-Zirconia Nanocomposites

Conventionally, HAP-zirconia composite powders have been prepared by ball-milling HAP and zirconia powders [6], or by adding zirconia crystallites during the HAP precipitation, followed with a hydrothermal treatment [4, 5, 11]. These approaches required a loading of 30–66 wt% zirconia to substantially increase the mechanical properties of HAP, and greatly reduced the biocompatibility of the resulting systems. Furthermore, dense specimens were only obtained through hot isostatic pressing (HIPing) up to 1300°C at 200 MPa. Such severe sintering conditions resulted in the undesired phase decomposition and grain growth of HAP.

3.3.1.1. Effect of Synthesis Method on Sintering and Microstructure

A synthesis technique that involves a high dispersion of zirconia would require a smaller amount of additive for reinforcing HAP. The resulting composite would also be easier to sinter, and provide a phase-pure HAP-based system that is stronger and more biocompatible. In this study, we examined two different methods of synthesizing HAP-zirconia composites. To achieve intimate mixing of phases and interactions at the nanometer scale, colloidal addition was used to introduce hydrothermally treated zirconia during the precipitation of HAP. To create composites by a physical process, the gel mixing approach was employed.

The 550°C-calcined HAP-zirconia (3 wt%) nanocomposites prepared by gel-mixing using zirconium hydroxide (Figure 3.1(a)) and crystalline zirconia (Figure 3.1(b)) have a similar particle morphology and zirconia dispersion. HAP nanocrystals were slightly elongated, and the zirconia nanocrystals were spherical. In the nanocomposite prepared by colloidal addition, HAP nanocrystals appeared to be coating the primary zirconia particles (Figure 3.1(c)). In this synthesis, zirconia served as nucleation sites during the HAP precipitation, so HAP nanocrystals were formed on the surfaces of the zirconia particles. This phenomenon should provide for a more intimate mixing of HAP and zirconia.

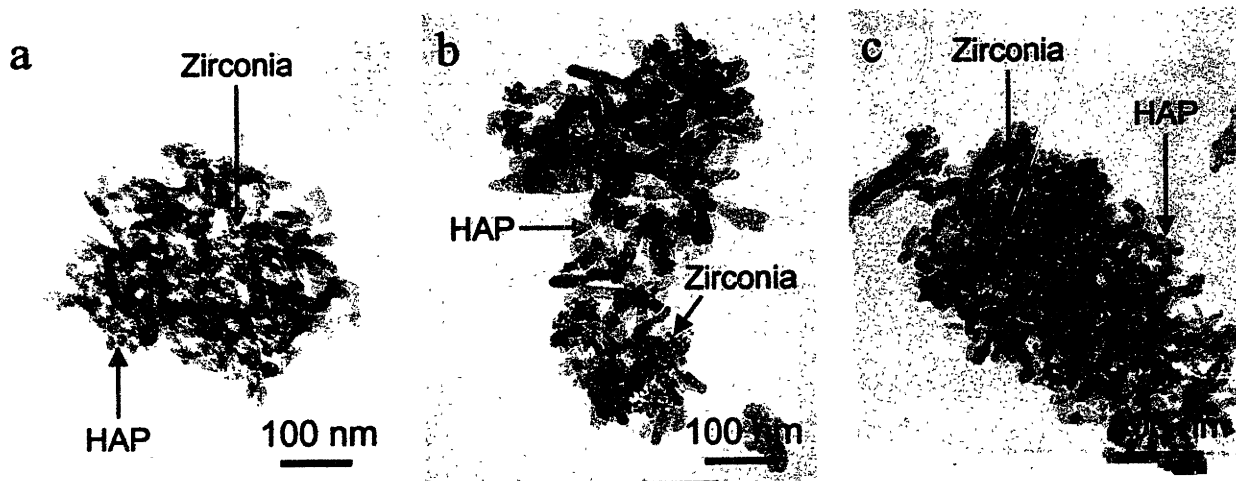


Figure 3.1. TEM micrographs of HAP-zirconia (3 wt%) nanocomposite powders prepared by gel mixing with (a) amorphous zirconium hydroxide and (b) crystalline zirconia, and (c) by colloidal addition of crystalline zirconia.

After pressure-assisted sintering at 1000°C and 50 MPa, the % theoretical densities of all three nanocomposites were 98%. By our approaches, 3 wt% zirconia addition did not affect the sintering of HAP significantly, allowing successful densification by a relatively low-temperature, low-pressure process. Backscattered SEM images illustrated that the nanocomposites derived by gel mixing (Figures 3.2(a) and (b)) possessed a lower zirconia dispersion than that prepared by colloidal addition (Figures 3.2 (c) and (d)). The former has a zirconia dispersion on the order of 200 nm. In contrast, the colloidal addition technique resulted in a ultrahigh dispersion of individual 30-nm zirconia grains in the HAP matrix.

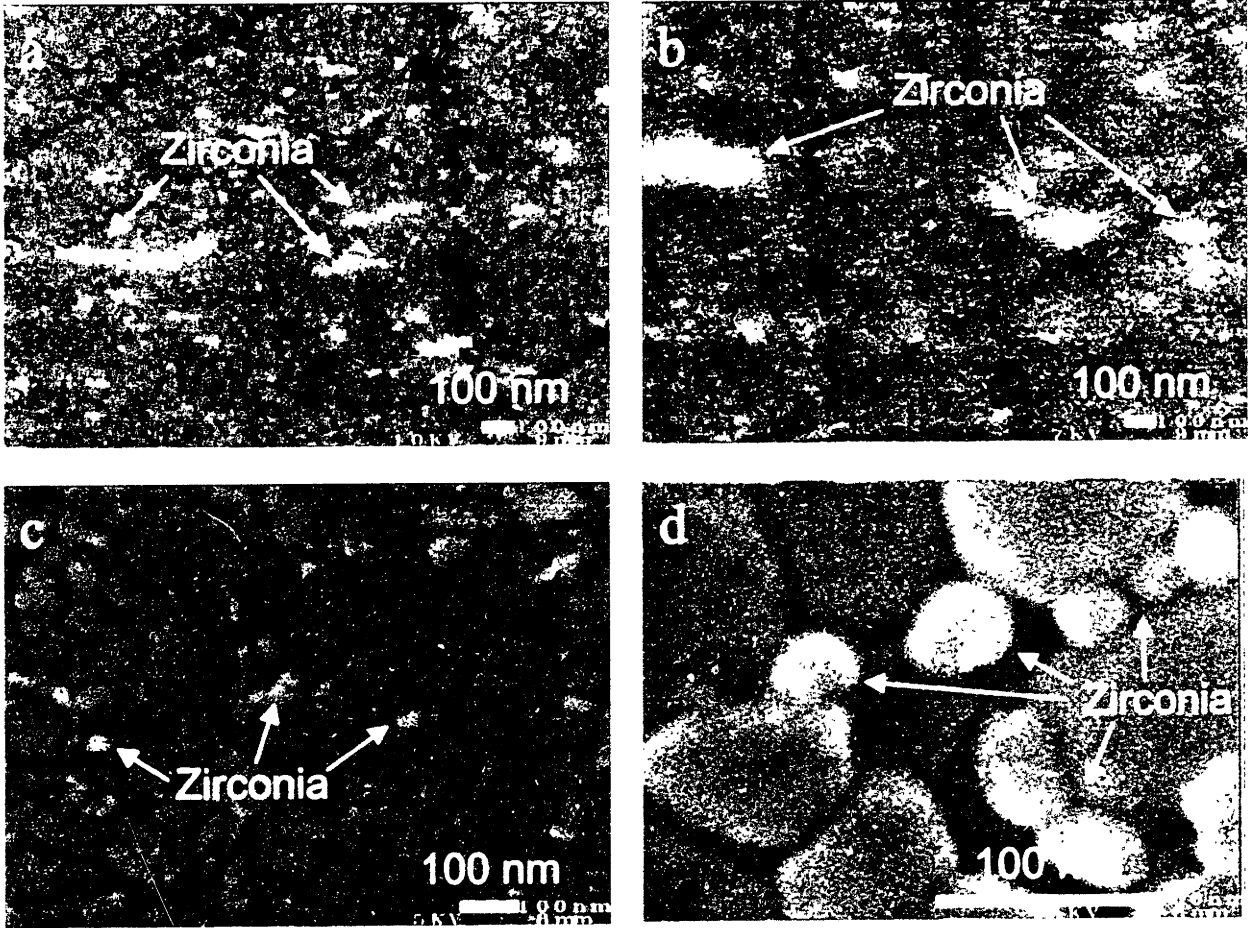


Figure 3.2. Backscattered SEM micrographs of HAP-zirconia (3 wt%) nanocomposites after pressure-assisted sintering at 1000°C and 50 MPa. The samples were prepared by gel mixing with (a) amorphous zirconium hydroxide and (b) crystalline zirconia, and (c,d) by colloidal addition of crystalline zirconia.

3.3.1.2 Effect of Zirconia Loading on Sintering and Microstructure

Since colloidal addition yielded a higher zirconia dispersion, this technique was used to examine the effect of zirconia loading on nanocomposites in detail. The calcined HAP-zirconia nanocomposite powders were sintered at 500–1300 °C for 30 min under a uniaxial load of 50 MPa. The highest density that could be achieved without decomposition was obtained by systems with 1 and 3 wt% zirconia loading at 1000 °C (see Figure 3.3). HAP-zirconia (15 wt%) nanocomposite did not fully densify before decomposition began at 1000 °C. Zirconia typically sinters at temperatures of 1500–1800 °C [12], which is above the HAP decomposition temperature. Consequently, the presence of a significant amount of zirconia is expected to hinder the densification of HAP based systems. Figure 3.4 illustrates that the nanocomposite

with 3 wt% zirconia loading has an ultrafine dispersion of zirconia, and that those with 8 and 15 wt% zirconia loadings suffered from a reduced zirconia dispersion.

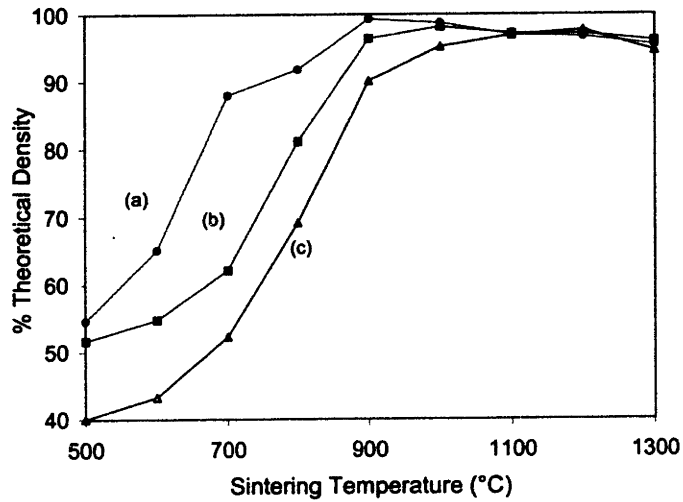


Figure 3.3. Sintering curves of HAP-zirconia nanocomposites with (a) 0, (b) 3 and (c) 15 wt% zirconia, prepared by colloidal addition.

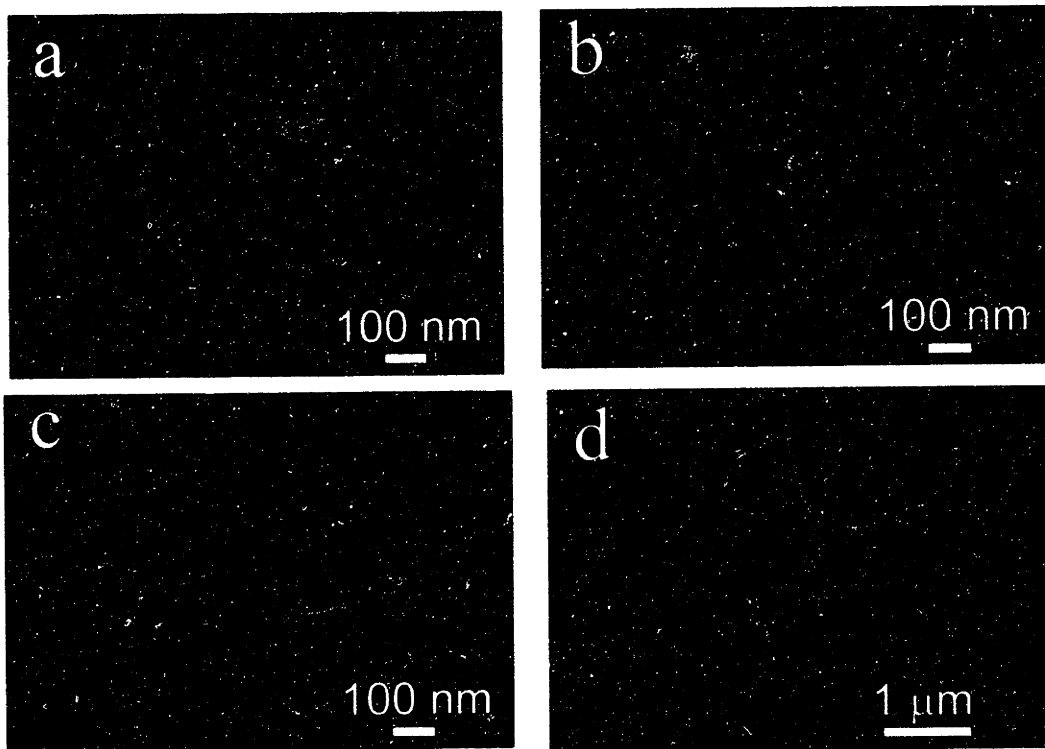


Figure 3.4. Backscattered SEM micrographs of HAP-zirconia nanocomposites pressure-assisted sintered at 1000°C and 50 MPa. The samples have zirconia loadings of (a) 0, (b) 3, (c) 8 and (d) 15 wt%.

3.3.1.3. *Effect of Zirconia Loading on Mechanical Properties*

Zirconia is potentially a superior reinforcing agent because it has a lower Young's modulus, greater strength, better wear properties, and higher fracture toughness than other common ceramics such as alumina. Zirconia also offers multiple mechanisms for toughening the HAP matrix. Like alumina, zirconia can provide mechanical reinforcement through a crack deflection mechanism. A crack will be able to propagate when the tip of the crack gains enough energy such that it is equal to the fracture toughness of the surrounding material. For pure hydroxyapatite, cracks will propagate when their energy is equal to $\sim 1.0 \text{ MPa}\cdot\text{m}^{1/2}$. When the propagating crack encounters a harder phase such as zirconia, it would be deflected around the harder phase, dissipating crack energy and slowing crack growth. In addition to crack deflection, the tetragonal phase of zirconia provides additional reinforcement through phase transformation toughening. The energy carried by a propagating crack may cause tetragonal zirconia to change to the monoclinic phase [12], which is associated with an increase in volume of 3–4%. This volume increase creates a compressive force that serves to counteract crack-tip stress, preventing the crack from propagating further [12]. Typically, the stability of the tetragonal phase increases with reduced zirconia grain size. In Figure 3.4(b), we note that the zirconia nanocrystals were only $\sim 30 \text{ nm}$ in dimension in the HAP-zirconia (3 wt%) nanocomposite. Consequently, the tetragonal phase in these zirconia nanocrystals was highly stable, and the introduction of yttria dopants into the zirconia nanocrystals would further stabilize the tetragonal phase.

The Vickers hardness (H_v) of HAP-based nanocomposites was measured as a function of zirconia loading and as a function of zirconia stabilization. Vickers hardness is a convenient method for estimating the yield strength (σ_y) of ceramic systems since $H_v \approx 3\sigma_y$. The yield strength is defined as the stress at the onset of plastic flow. The greatest hardness for HAP-based nanocomposites was achieved with an addition of 1.5 wt% TZ and YSZ (Figure 3.5). The introduction of more zirconia would reduce hardness due to the difficulty in fully sintering the nanocomposites. Although nanocomposite sintering was still hindered as loading was increased beyond 5 wt% TZ, bulk TZ properties began to compensate for the incomplete densification. For HAP-YSZ nanocomposites, we observed a similar trend; hardness of the system increased when YSZ loading was increased beyond 8 wt%.

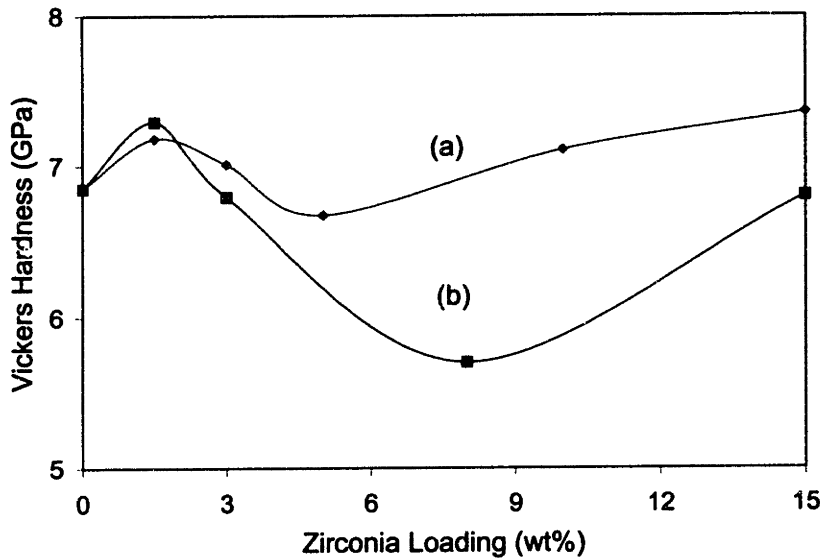


Figure 3.5. Vickers hardness of HAP-zirconia nanocomposites as a function of (a) TZ and (b) YSZ loadings.

HAP-zirconia nanocomposites that were > 98% dense were subjected to bending and compressive tests. With the addition of 1.5 wt% TZ, the bending strength of the HAP-based nanocomposite was increased to 243 MPa (Table 3.3). HAP-TZ (3 wt%) nanocomposite has a lower bending strength of 203 MPa, which was still higher than that of pure HAP (183 MPa). Unlike TZ, YSZ was unable to undergo phase transformation due to the additional stabilization provided by the yttria dopant. Consequently, even though YSZ was highly dispersed (like TZ) within the HAP matrix, the resulting nanocomposites did not provide for enhanced bending strengths. High-resolution TEM micrographs show that both the sintered nanocrystalline HAP and HAP-zirconia (3 wt%) nanocomposite were fully dense with crystalline interfaces and ultrafine grains (Figure 3.6). Figures 3.6(c) and (d) further illustrate that the zirconia grains were dispersed intergranularly within the HAP matrix, without introducing glassy phases or defects. Since potential cracks would likely propagate along the grain boundaries in materials with such an ultrafine microstructure, the high intergranular dispersion of zirconia nanocrystals offered by the colloidal addition technique provided an attractive benefit in strengthening the HAP matrix.

Table 3.3. Bending strengths of HAP-TZ and HAP-YSZ nanocomposites.

| Zirconia Loading (wt%) | Bending Strength (MPa) | |
|---------------------------|------------------------|---------|
| | HAP-TZ | HAP-YSZ |
| 0 | 183 | 183 |
| 1.5 | 243 | 164 |
| 3 | 203 | 156 |

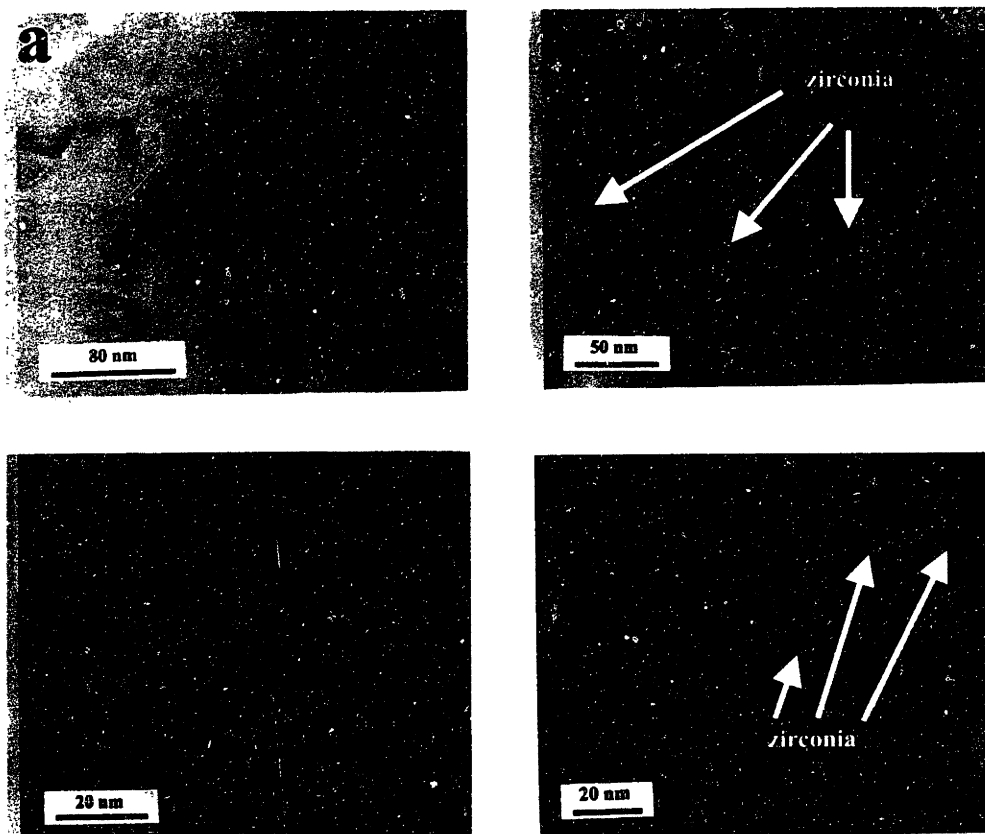


Figure 3.6. Thin-section high-resolution TEM micrographs of pressure-assisted sintered nanocrystalline (a,b) HAP and (c,d) HAP-zirconia (3 wt%).

Through nanocomposite processing, we were able to achieve dramatic improvements in the HAP-zirconia system with the use of a very low TZ loading. Table 3.4 shows that the HAP-TZ (1.5 wt%) nanocomposite provided a greater bending strength than conventional composite that required a high loading of 18 wt% zirconia [11, 13]. By using a much smaller amount of zirconia, the Young's modulus of the nanocomposite was also not increased as much as the conventional composite. The small amount of zirconia added would also allow the HAP to retain its high bioactivity in implant applications.

Table 3.4. Mechanical properties of various materials and HAP-zirconia nanocomposite.

| Composition | Bending Strength (MPa) | Compressive Strength (MPa) | Young's Modulus (GPa) |
|---|------------------------|----------------------------|-----------------------|
| Zirconia [12] | 900–1200 | 2000 | 210 |
| Conventional HAP [10] | 38–113 | 120–800 | 120 |
| Nano HAP | 183 | 879 | 130 |
| Conventional HAP-Zirconia (18 wt%) [11, 13] | 160 | – | 171 |
| Nano HAP-Zirconia (1.5 wt%) | 243 | 766 | 149 |

3.3.2. HAP-Silver Nanocomposites

The highest literature values in fracture toughness have been achieved with HAP containing 20–30% FeCr alloy fibers ($K_{Ic} = 6.0\text{--}7.4 \text{ MPa}\cdot\text{m}^{1/2}$). However, the question remains whether a metal-reinforced HAP composite may remain highly biocompatible. The use of metal often introduces problems such as corrosion, wear, and/or negative tissue reaction [10]. In contrast to other metal additives, silver may be used without the above issues due to its inert and anti-bacterial properties [8]. Its high ductility can also be gainfully employed to toughen HAP through plastic deformation and crack bridging mechanisms [8].

Through nanocomposite processing, we have successfully incorporated silver into HAP matrix with a good dispersion. The HAP-silver powders were sintered at 900°C and 100 MPa for 30 min. Figures 3.7 and 3.8 show that the bending and compressive strengths of HAP were substantially increased with the addition of 5 vol% silver. At lower silver loadings, the mechanical strengths of the composite systems were lower than the pure HAP material. This was because silver introduced critical size defects, and the highly dispersed silver (see Figure 3.9(a)) was not at a sufficiently high loading level to absorb enough crack energy through plastic deformation or bridge the propagating cracks. 5 vol% appeared to be the critical loading at which silver could absorb crack energy and no longer behaved as a defect (see Figure 3.9(b)). At higher loadings, negative contributions from a lowered silver dispersion (see Figure 3.9(c)) could dominate to decrease mechanical strengths. Only at a very high loading of 30 vol% would the bulk properties of silver begin to compensate for such negative effects as poor silver dispersion. This is illustrated in Figure 3.9(d), which shows that silver formed semi-continuous phase within the HAP matrix.

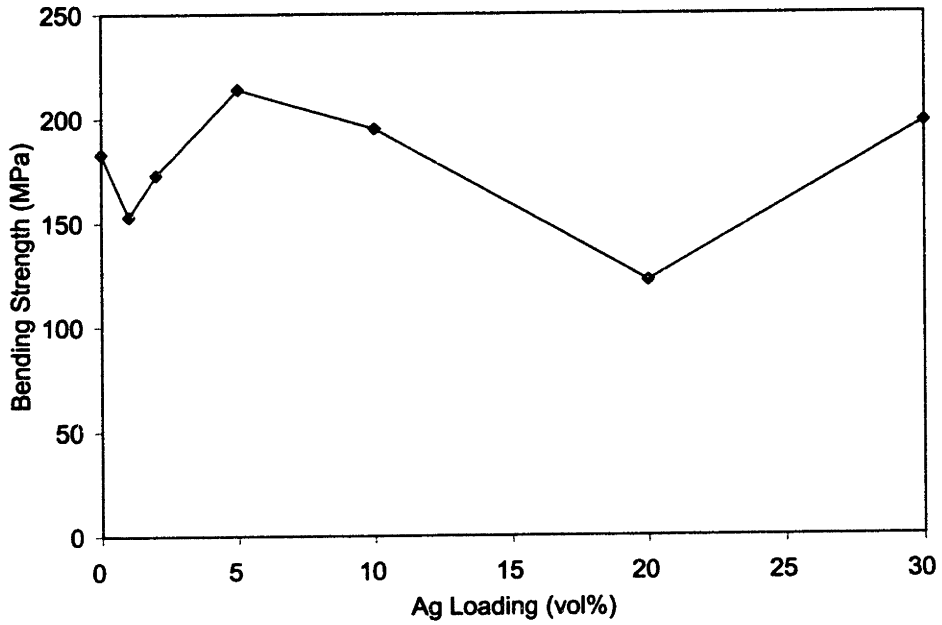


Figure 3.7. Bending strength of HAP-silver nanocomposites as a function of silver loading.

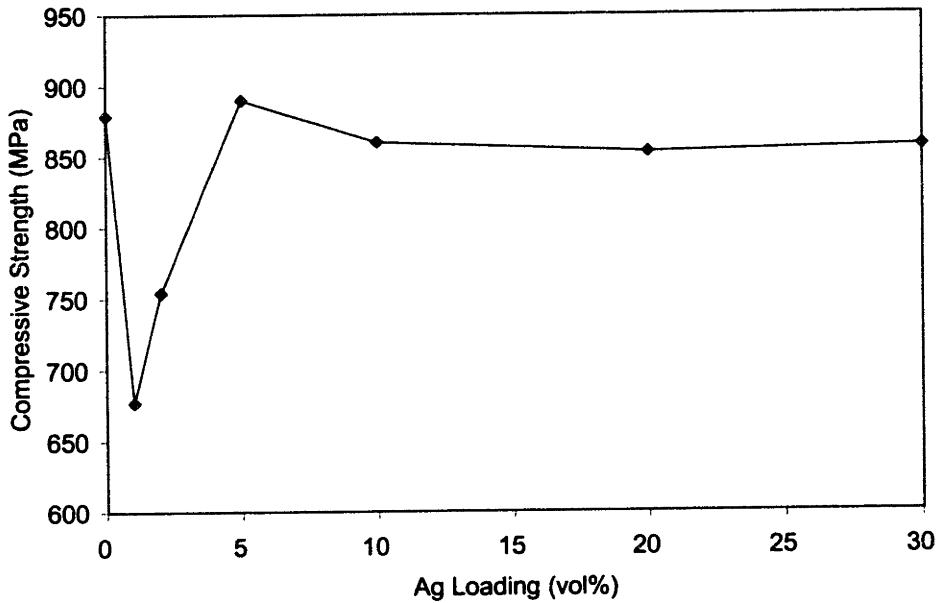


Figure 3.8. Compressive strength of HAP-silver nanocomposites as a function of silver loading.

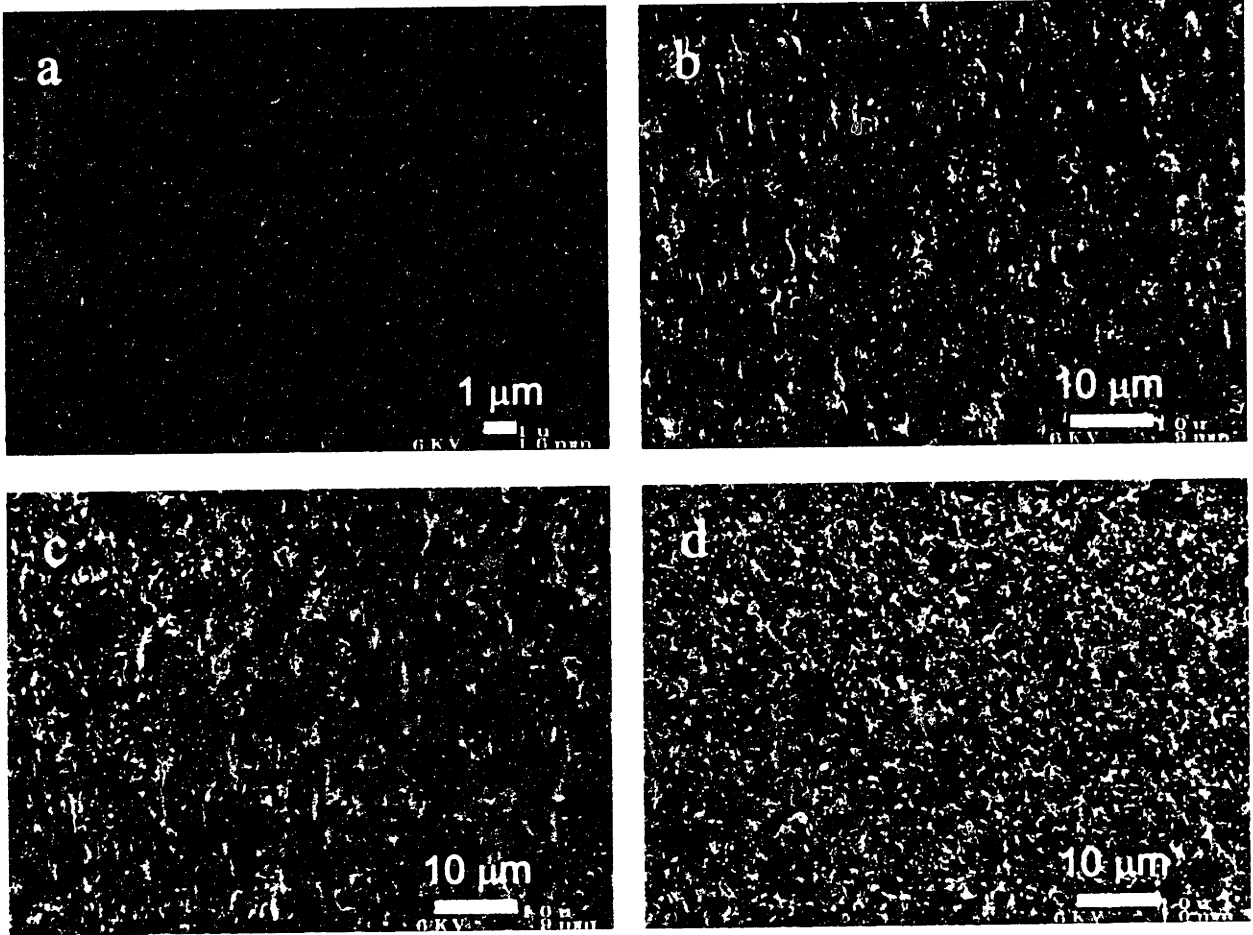


Figure 3.9. Backscattered SEM micrographs of sintered HAP-silver nanocomposites with (a) 1, (b) 5, (c) 20 and (d) 30 vol% silver. The bright pixels in the micrographs corresponded to silver.

The optimal HAP-silver nanocomposite is compared to conventional HAP-silver composites in Table 3.5. Chaki *et al.* [9] observed that the bending strength of their composite was maximized at 80 MPa with 5 vol% silver loading, but their average HAP and silver grain sizes were 1.4 μm and 10 μm, respectively. The optimal HAP-silver composite developed by Zhang *et al.* [8] consisted of 10 vol% silver and possessed a bending strength of 100 MPa. Zhang *et al.*'s systems have an average silver grain size of 1.5 μm, the HAP grain size was 0.75–0.8 μm at 5–10 vol% silver loading. In contrast to the conventional composites, our HAP-silver nanocomposite possessed a much finer HAP grain size (100 nm) and a higher silver dispersion. Thus, it was able to achieve a much higher bending strength of 214 MPa at a low silver loading of 5 vol%.

Table 3.5. Mechanical properties of various materials and HAP-silver nanocomposite.

| Composition | Bending Strength (MPa) | Compressive Strength (MPa) |
|---------------------------------------|------------------------|----------------------------|
| Conventional HAP [10] | 38–113 | 120–800 |
| Nano HAP | 183 | 879 |
| Nano HAP-silver (5 vol%) | 214 | 890 |
| Conventional HAP-silver (5 vol%) [9] | 80 | – |
| Conventional HAP-silver (5 vol%) [8] | 65 | – |
| Conventional HAP-silver (10 vol%) [8] | 100 | – |

3.4. Conclusions

To form a strong and bioactive HAP-based material, nanocomposite processing was developed to achieve a high dispersion of zirconia or silver with HAP nanocrystals. This allowed for structural reinforcement without the need of a high loading of additives. The resulting nanocomposites could be densified without the use of severe sintering conditions that frequently caused HAP decomposition. They possessed significantly higher mechanical strength compared to pure HAP and conventional HAP-based composites. By utilizing a small loading of zirconia and silver effectively in the nanocomposite systems, the HAP matrix could be greatly strengthened without considerably compromising its biocompatibility.

3.5. References

- [1] E. Adolfsson, P. Alberius-Henning, L. Hermansson, *J. Am. Ceram. Soc.* **83**, 2798 (2000).
- [2] J. A. Delgado, *et al.*, *J. Mater. Sci. Mater. Med.* **10**, 715 (1999).
- [3] L. Fu, K. A. Khor, J. P. Lim, *Surf. Coat. Technol.* **127**, 66 (2000).
- [4] K. Ioku, M. Yoshimura, S. Somiya, *Mater. Res. Soc. Symp. Proc.* **110**, 445 (1989).
- [5] K. Ioku, S. Somiya, M. Yoshimura, *J. Ceram. Soc. Jpn.* **99**, 196 (1991).
- [6] J. Li, H. Liao, L. Hermansson, *Biomater.* **17**, 1787 (1996).
- [7] J. Li, E. Adolfsson, H. Liao, L. Hermansson, *J. Dent. Res.* **75**, 2158 (1996).
- [8] X. Zhang, G. H. M. Gubbels, R. A. Terpstra, R. Metselaar, *J. Mater. Sci.* **32**, 235 (1997).
- [9] T. K. Chaki, P. E. Wang, in *Bioceramics: Materials and Applications*, G. Fischman, A. Clare, L. Hench, Eds. (The American Ceramic Society, Westville, 1995), vol. 48, p. 235.
- [10] W. Suchanek, M. Yoshimura, *J. Mater. Res.* **13**, 94 (1998).
- [11] K. Ioku, M. Yoshimura, S. Somiya, *Biomater.* **11**, 57 (1990).

- [12] C. Piconi, G. Maccauro, *Biomater.* **20**, 1 (1999).
- [13] J. Li, H. Liao, L. Hermansson, *Biomater.* **17**, 1787 (1996).

Chapter 4 – Carbonated Apatite Nanocrystals

4.1. Introduction

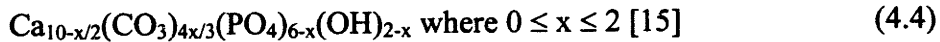
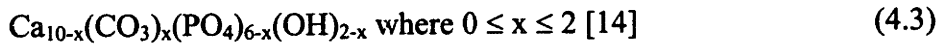
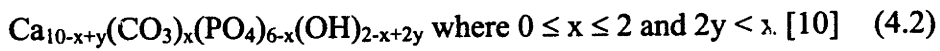
Carbonated apatite represents the mineral phase found in natural bone, which contains 5–8 wt% carbonate [1]. Thus, synthetic carbonated apatite is of great interest for medical and dental applications [2]. It has shown excellent osteogenic properties [3], and is anticipated to possess unusual properties, such as enhanced dissolution, osteoclast-mediated resorption and matrix synthesis [4-6]. Furthermore, carbonated apatite may stimulate the chemistry of the mineralized tissue in bioceramic materials, and may provide a means of improving the level of biological response of the host to the implant *in vivo* [7-9]. Carbonated apatite may be used instead of synthetic, unsubstituted hydroxyapatite for future orthopedic implant applications.

Hydroxyapatite is tolerant of vacancies and substitutions because of its complex composition and crystal structure ($P6_3/m$) (see Figure 1.4). Stoichiometric, unsubstituted HAP has a chemical formula of $Ca_{10}(PO_4)_6(OH)_2$ and a Ca/P ratio of 1.67, but nonstoichiometric HAP materials having a Ca/P ratio greater than 1.44 or less than 2.4 still possess an apatitic crystal structure by X-ray diffraction (XRD). In addition, calcium can be easily substituted with other Group I and II elements, while the phosphate group can be substituted with AsO_4^{3-} , VO_4^{3-} , SiO_4^{4-} , SO_4^{2-} , CO_3^{2-} , etc. Furthermore, the hydroxide site can be substituted with F^- , Cl^- , Br^- , I^- , CO_3^{2-} , etc. [10, 11]. Thus, dopants can be easily introduced in a typical synthesis [12, 13] to control the chemical stability and rate of resorption. To increase stability in acidic environments, for example, fluorine ions can be used to substitute for the hydroxyl groups. Carbonate ions can be introduced into the hydroxyapatite structure to decrease stability and to synthesize an apatite more closely resembling natural bone mineral.

The carbonate ion may be substituted into the apatite crystal structure at two locations. For type A and type B carbonated apatites, carbonate ions are substituted into the hydroxyl sites and phosphate sites of the apatite lattice, respectively. Type A carbonated apatites possess a chemical formula of



where $0 \leq x \leq 1$. Several different models have been proposed for the chemical formula of a type B carbonated apatite, such as,



The differences in these three models are attributed to different assumptions in the number of carbonates replacing a phosphate ion and the charge balance mechanism. Generally, type A carbonated apatites are synthesized at high temperatures, whereas type B carbonated apatites are formed at low temperatures [6]. Type B carbonated apatites may contain varying amounts of carbonates and have consequently an ill-defined crystal structure, while type A carbonated apatites are crystallographically well-defined. Type B carbonated apatites are more similar to natural bone mineral, and are therefore more desirable as a synthetic bone crystal.

When carbonates are substituted into phosphate sites, crystallite size and crystallinity are reduced for the apatites, and spheroidal particles are formed. The resulting carbonated apatites have an increase in the solubility compared to HAP [6]. The composition and structure of carbonated apatites depend on the preparation conditions [14]. Processing parameters such as precursor Ca/P ratio in the reaction medium, CO_3^{2-} concentration in the reaction medium, solution pH, aging temperature and time can be used to obtain carbonated apatites in different morphologies and compositions [14]. Nanostructure processing of carbonated apatite may achieve selective carbonate substitution into the apatite crystal structure, and attain excellent chemical homogeneity and phase purity.

4.2. Experimental

4.2.1. Synthesis of Carbonated Apatite

First, a stock solution of 0.5 M $\text{Ca}(\text{NO}_3)_2$ (CaN, Fluka) (pH = 10.4) and a stock solution of 0.3 M $(\text{NH}_4)_2\text{HPO}_4$ (NHP, Fluka) (pH = 10.4) were prepared. $(\text{NH}_4)\text{HCO}_3$ (NHC, Aldrich) was added to the NHP solution to give a NHC concentration of 0.1, 0.3, 0.9 or 2.0 M. The CaN solution was then slowly added (3 ml/min) to the NHP/NHC solution to give a precursor Ca/P ratio of 1, 1.67, 3.33 or 5. This mother liquor was aged at 25°C or 80°C for 24 or 100 hr with stirring (see Table 4.1 for synthesis conditions). In other cases, the mother liquor was also hydrothermally treated at 120°C for 100 hr with daily agitation (see Table 4.2). After aging, the white precipitate was washed successively with aqueous solutions of decreasing pH, followed by

a series of ethanol washes. The gel was ground dry in a heated mortar and pestle, and oven-dried at 120°C overnight.

Table 4.1. Synthesis conditions for carbonated apatite precipitation.

| Ca/P Ratio | NHC (M) | Aging Time (hr) | Aging Temperature (°C) |
|------------|---------|-----------------|------------------------|
| 1.67 | 0.0 | 24 | 25 |
| 1.67 | 0.3 | 24 | 25 |
| 1.67 | 2.0 | 24 | 25 |
| 1.67 | 0.0 | 24 | 80 |
| 1.67 | 0.1 | 24 | 80 |
| 1.67 | 0.3 | 24 | 80 |
| 1.67 | 2.0 | 24 | 80 |
| 1.67 | 0.0 | 100 | 25 |
| 1.67 | 0.1 | 100 | 25 |
| 1.67 | 0.3 | 100 | 25 |
| 1.67 | 2.0 | 100 | 25 |
| 1.67 | 0.0 | 100 | 80 |
| 1.67 | 0.1 | 100 | 80 |
| 1.67 | 0.3 | 100 | 80 |
| 3.33 | 0.0 | 24 | 25 |
| 3.33 | 0.1 | 24 | 25 |
| 3.33 | 0.3 | 24 | 25 |
| 3.33 | 1.5 | 24 | 25 |
| 3.33 | 2.0 | 24 | 25 |
| 3.33 | 0.0 | 24 | 80 |
| 3.33 | 0.3 | 24 | 80 |
| 3.33 | 2.0 | 24 | 80 |
| 3.33 | 0.0 | 100 | 25 |
| 3.33 | 0.1 | 100 | 25 |
| 3.33 | 0.3 | 100 | 25 |

Table 4.2. Hydrothermal treatment conditions for carbonated apatite.

| Ca/P Ratio | NHC (M) | Aging Time (hr) | Aging Temperature (°C) |
|------------|---------|-----------------|------------------------|
| 1 | 0.0 | 100 | 120 |
| 1 | 0.1 | 100 | 120 |
| 1 | 0.3 | 100 | 120 |
| 1 | 0.9 | 100 | 120 |
| 1.67 | 0.0 | 100 | 120 |
| 1.67 | 0.1 | 100 | 120 |
| 1.67 | 0.3 | 100 | 120 |
| 1.67 | 0.9 | 100 | 120 |
| 1.67 | 2.0 | 100 | 120 |
| 3.33 | 0.0 | 100 | 120 |
| 3.33 | 0.1 | 100 | 120 |
| 3.33 | 0.3 | 100 | 120 |
| 3.33 | 0.9 | 100 | 120 |
| 5 | 0.0 | 100 | 120 |
| 5 | 0.45 | 100 | 120 |
| 5 | 0.9 | 100 | 120 |
| 5 | 1.5 | 100 | 120 |

4.2.2. Characterization of Carbonated Apatite

The precipitated carbonated apatite powders were characterized by XRD, transmission electron microscopy (TEM), photoacoustic Fourier-transform infrared spectroscopy (PA-FTIR), inductively coupled plasma – atomic emission spectroscopy (ICP-AES), CHN analysis, thermogravimetric analysis (TGA), and mass spectroscopy (MS). The dependence of phase behavior on processing conditions was evaluated by XRD on a Siemens D5000 θ - θ diffractometer (45 kV, 40 mA, Cu K_{α}). Particle morphology was determined from TEM micrographs obtained with a JEOL 200CX or JEOL 2000 microscope. PA-FTIR studies were performed with a Biorad FTS-60A spectrometer with a MTEC photoacoustic attachment to characterize carbonate substitution. Ca and P contents of the carbonated apatites were analyzed using a Perkin-Elmer Plasma 40. CHN analysis (Quantitative Technologies Incorporated, Whitehorse, NJ) was performed to quantify total carbon. TGA (Perkin Elmer System 7) and MS (VG Gaslab 300) were used to measure the weight loss at $\leq 1000^{\circ}\text{C}$ and to characterize the carbonate desorption profile within the apatitic structure [15, 16]. The TGA samples were held at 25°C for 10 min and heated to 150°C at $10^{\circ}\text{C}/\text{min}$, followed by heating from 150°C to 1000°C at $25^{\circ}\text{C}/\text{min}$, with a soak at 1000°C for 10 min in a helium carrier gas. The exiting carrier gas was analyzed by the MS to measure the carbonates evolved from the samples during heat treatment.

4.3. Results and Discussion

4.3.1. Effect of Aging Time on Apatite Chemistry and Phase Stability

The effect of aging time was investigated by mapping the phase behavior of the calcium phosphate precipitates as a function of the precursor Ca/P ratio and the NHC concentration in the reaction medium. Apatitic, calcium carbonate, and amorphous phases were observed after 24 hr of aging at 25°C (Figure 4.1(a)). At a precursor Ca/P ratio of 1.67, a pure apatitic phase was detected by XRD at all NHC concentrations examined. However, the apatitic phase decreased in crystallite size along the $\langle 002 \rangle$ axis from 26 nm to 11 nm as NHC concentration in the reaction medium was increased (Figure 4.2 and Table 4.3). At a precursor Ca/P ratio of 3.33, the excess calcium ions and the presence of NHC in the reaction medium reduced the stability of the apatitic phase. A pure apatitic phase was observed only in the absence of NHC (Figure 4.3(a)). The presence of 0.3 M NHC in the reaction medium resulted in a single phase of calcium

carbonate with an amorphous background (Figure 4.3(b)). The presence of 2.0 M NHC in the reaction medium produced an amorphous material (Figure 4.3(c)).

An increase in aging time to 100 hr reduced the stability of the crystalline apatitic and calcium carbonate phases (Figure 4.1(b)). Pure carbonated apatite phase was obtained at 25°C at a precursor Ca/P ratio of 1.67 and low NHC concentrations; a biphasic material of carbonated apatite and calcium carbonate was obtained at a high NHC concentration of 2 M. Amorphous materials were obtained at NHC concentrations ≥ 0.3 M with a high precursor Ca/P ratio of 3.33. The phase behavior in Figure 4.1(b) could be attributed to the significant dissolution and reprecipitation that occurred with extensive aging of the calcium phosphate precipitates [17-21].

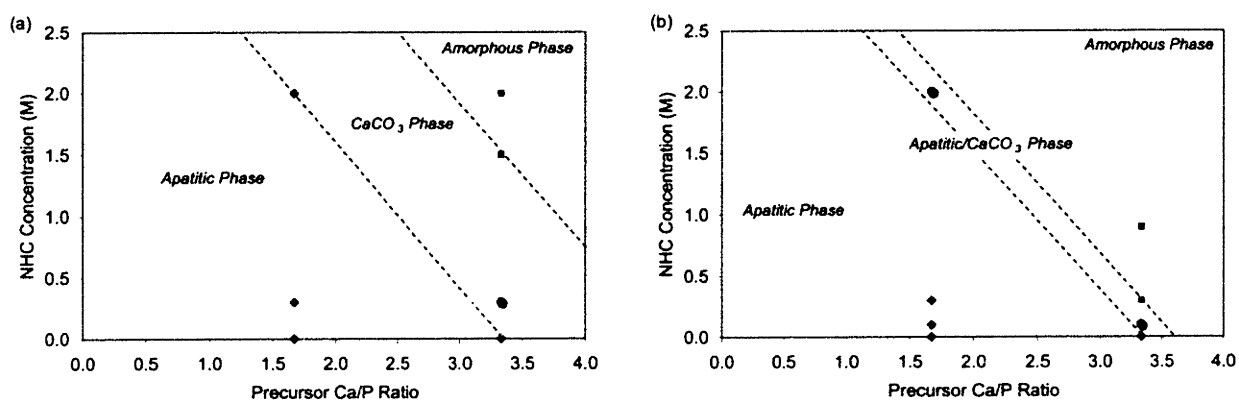


Figure 4.1. The XRD phase behavior of calcium phosphate precipitates aged at 25°C for (a) 24 and (b) 100 hr.

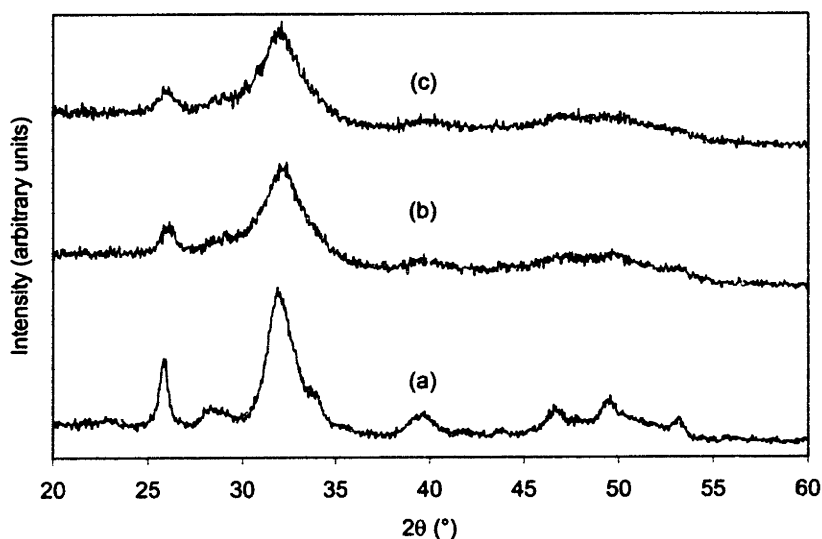


Figure 4.2. XRD patterns of calcium phosphate precipitates aged for 24 hr at 25°C with a precursor Ca/P ratio of 1.67 and (a) 0, (b) 0.3 and (c) 2.0 M NHC in the reaction medium. All peaks corresponded to the apatitic phase.

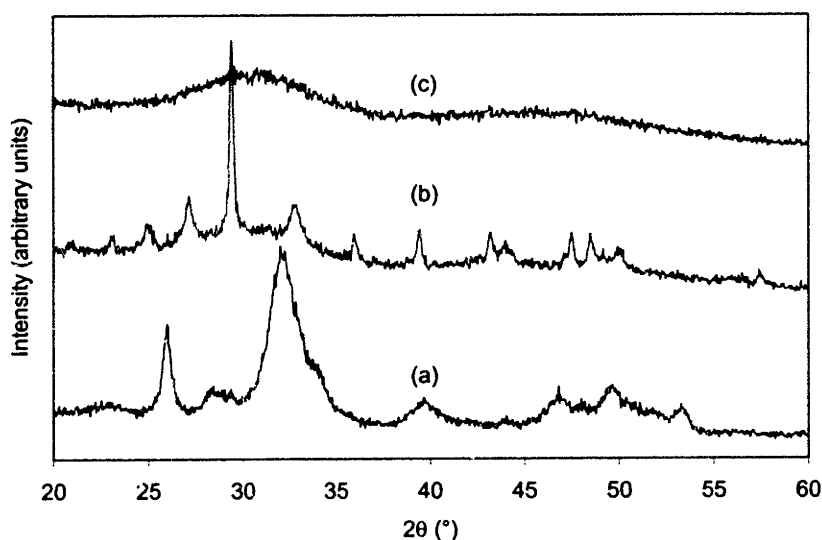


Figure 4.3. XRD patterns of calcium phosphate precipitates aged for 24 hr at 25°C with a precursor Ca/P ratio of 3.33 and (a) 0, (b) 0.3 and (c) 2.0 M NHC in the reaction medium. Peaks in (a) corresponded to the apatitic phase. Peaks in (b) corresponded to calcium carbonate. Peaks in (c) corresponded to an amorphous phase.

For carbonated apatites synthesized with a precursor Ca/P ratio of 1.67, the Ca and P contents were analyzed by ICP-AES, and the weight loss by heat treatment to 1000°C was determined by TGA. At 24 hr of aging, the measured Ca/P ratio of the carbonated apatites was

greater than 1.67, and increased with increasing NHC concentration. The weight loss determined by TGA also increased with the NHC concentration, indicating greater carbonate incorporation into the apatitic structure. For systems aged for 100 hr, the weight loss also increased with increasing NHC concentration, but not at the same extent as the systems aged for 24 hr. Furthermore, the Ca/P ratio of the carbonated apatites aged for 100 hr was close to the stoichiometric value for HAP (i.e., 1.67) for the various NHC concentrations examined (0–0.3 M).

Table 4.3. Effect of aging time and NHC concentration on the Ca/P molar ratio of carbonated apatite aged at 25°C.

| Aging Time (hr) | NHC Conc. (M) | Ca (wt%) | P (wt%) | Weight Loss (wt%) | Ca/P Ratio | Crystallite Size <002> (nm) |
|-----------------|---------------|----------|---------|-------------------|------------|-----------------------------|
| 24 | 0.0 | 37.7 | 16.5 | 8.0 | 1.77 | 26 |
| 24 | 0.3 | 42.1 | 17.6 | 17.7 | 1.85 | 13 |
| 24 | 2.0 | 39.6 | 14.2 | 19.4 | 2.15 | 11 |
| 100 | 0.0 | 38.4 | 17.8 | 4.3 | 1.69 | 82 |
| 100 | 0.1 | 42.4 | 19.9 | 6.2 | 1.65 | 20 |
| 100 | 0.3 | 41.9 | 19.3 | 15.0 | 1.68 | 15 |

Precursor Ca/P molar ratio = 1.67. All samples were of an apatitic phase.

The dramatic differences in the Ca/P ratio of the carbonated apatites indicated that precipitates were undergoing significant structural changes during aging. At short aging times, precipitates were calcium-rich, and significant amounts of carbonates were incorporated. As aging progressed, the increased crystallinity of the apatitic phase reduced the extent of carbonation, and the material assumed a Ca/P ratio similar to HAP.

4.3.2. Effect of Aging Temperature on Apatite Chemistry and Phase Stability

The effect of aging temperature on phase stability after 24 hr of aging is illustrated in Figure 4.4. An increase in aging temperature from 25°C to 80°C increased the crystallinity of the different phases. Consequently, the amorphous phase observed at 25°C was replaced with a mixed apatite-calcium carbonate region at 80°C. Regardless of aging temperature, increasing NHC concentration in the reaction medium decreased crystallinity as shown by the XRD patterns in Figure 4.5 and reduced the crystallite size along the <002> axis (see Table 4.3).

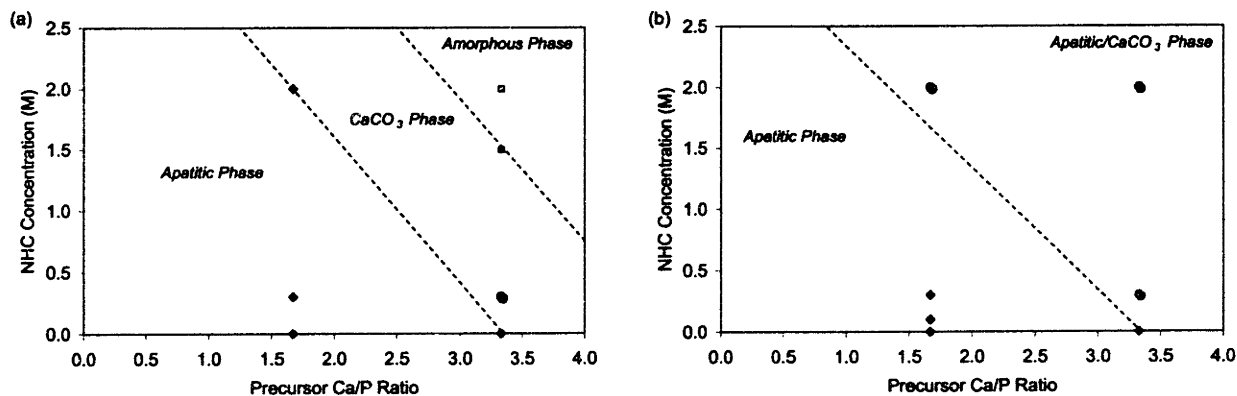


Figure 4.4. The XRD phase behavior of calcium phosphate precipitates aged for 24 hr at (a) 25°C and (b) 80°C.

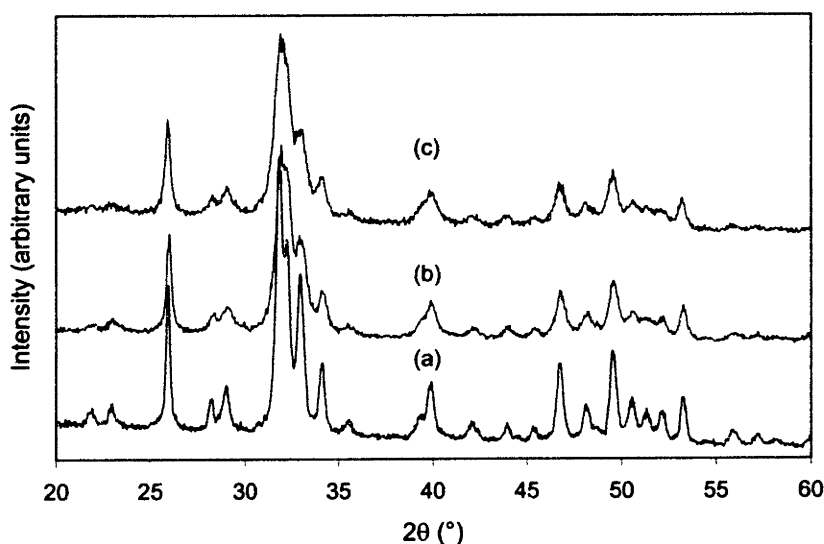


Figure 4.5. XRD patterns of calcium phosphate precipitates synthesized with a precursor Ca/P ratio of 1.67 and (a) 0, (b) 0.1 and (c) 0.3 M NHC in the reaction medium, and aged at 80°C for 24 hr. All peaks corresponded to the apatitic phase.

In section 4.3.1, increased aging time allowed the precipitates to mature into a more crystalline phase. Higher aging temperatures also facilitated the crystallization of the apatitic phase (see Table 4.4), yielding a Ca/P ratio that approached 1.67. The greater crystal growth of these carbonated apatites corresponded to a decreased weight loss measured by TGA and a reduced extent of carbonate substitution in the crystal structure.

Table 4.4. Effect of aging temperature and NHC concentration on the Ca/P molar ratio of carbonated apatite aged for 24 hr.

| Aging Temperature (°C) | NHC Conc. (M) | Ca (wt%) | P (wt%) | Weight Loss (wt%) | Ca/P Ratio | Crystallite Size <002> (nm) |
|------------------------|---------------|----------|---------|-------------------|------------|-----------------------------|
| 25 | 0.0 | 37.7 | 16.5 | 8.0 | 1.77 | 26 |
| 25 | 0.3 | 42.1 | 17.6 | 17.7 | 1.85 | 13 |
| 25 | 2.0 | 39.6 | 14.2 | 19.4 | 2.15 | 11 |
| 80 | 0.0 | 40.9 | 18.5 | 5.2 | 1.71 | > 100 |
| 80 | 0.3 | 40.5 | 18.5 | 11.5 | 1.69 | 56 |

Precursor Ca/P molar ratio = 1.67. All samples were of an apatitic phase.

Figure 4.6 illustrates the effect of aging temperature on phase stability after 100 hr of aging. As the aging temperature was increased from 25°C to 120°C, the region of apatitic phase decreased and the amorphous phase regime disappeared. A wide region that contained a mixed phase of apatite and calcium carbonate was obtained at 120°C. Furthermore, hydrothermal treatment at 120°C increased the stability of the apatitic phase at high precursor Ca/P ratios. Unlike carbonated apatites prepared at other conditions, the hydrothermal treatment of carbonate-containing calcium phosphate precipitates resulted in a well-defined XRD pattern (Figure 4.7) and a grain size of ≥ 85 nm. As the crystallinity of the apatitic phase was increased with aging temperature, the weight loss, indicating extent of carbonation, was decreased (Table 4.5).

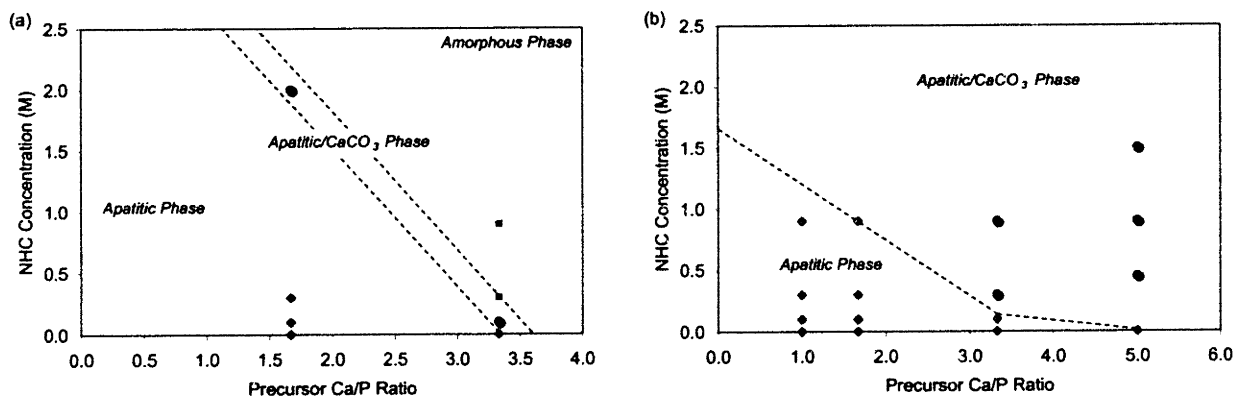


Figure 4.6. The XRD phase behavior of calcium phosphate precipitates aged for 100 hr at (a) 25°C and (b) 120°C.

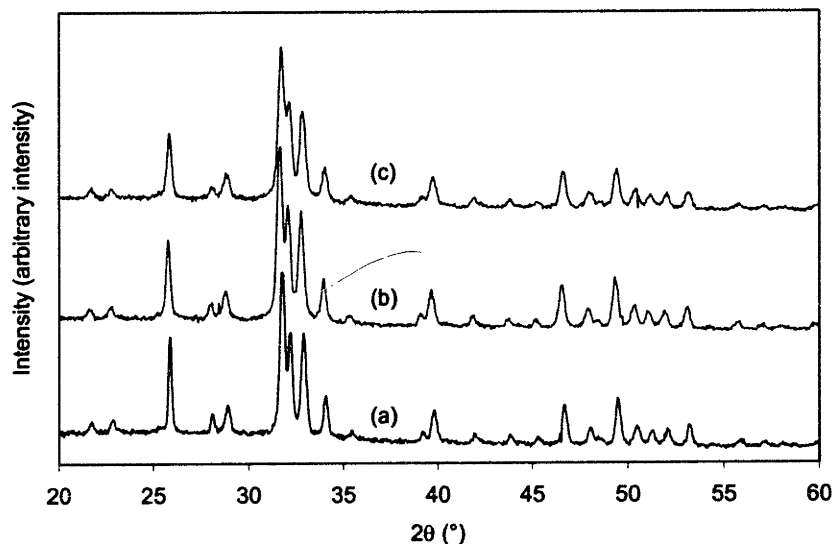


Figure 4.7. XRD patterns of calcium phosphate precipitates synthesized with a precursor Ca/P ratio of 1.67 and (a) 0, (b) 0.3 (c) 0.9 M NHC in the reaction medium, and aged at 120°C for 100 hr. All peaks corresponded to the apatitic phase.

Table 4.5. Effect of aging temperature and NHC concentration on the Ca/P molar ratio of carbonated apatite aged for 100 hr.

| Aging Temperature (°C) | NHC Conc. (M) | Ca (wt%) | P (wt%) | Weight Loss (wt%) | Ca/P Ratio | Crystallite Size <002> (nm) |
|------------------------|---------------|----------|---------|-------------------|------------|-----------------------------|
| 25 | 0.0 | 38.4 | 17.8 | 3.5 | 1.69 | 82 |
| 25 | 0.1 | 42.4 | 19.9 | 6.2 | 1.65 | 20 |
| 25 | 0.3 | 41.9 | 19.3 | 15.0 | 1.68 | 15 |
| 120 | 0.0 | 45.7 | 20.1 | 3.1 | 1.75 | > 100 |
| 120 | 0.3 | 37.9 | 15.8 | 4.5 | 1.86 | > 100 |
| 120 | 0.9 | 42.5 | 18.0 | 5.0 | 1.72 | 85 |

Precursor Ca/P molar ratio = 1.67. All samples were of an apatitic phase.

The effect of NHC concentration in the reaction medium on the Ca/P ratio of the carbonated apatites prepared with a precursor Ca/P ratio of 1 to 5 under hydrothermal conditions is presented in Figure 4.8. In the absence of NHC in the reaction medium, Ca/P ratio of the carbonated apatite precipitates was close to 1.67 regardless of the precursor Ca/P ratio. At a precursor Ca/P ratio of 1, the Ca/P ratio of the carbonated apatite precipitates was insensitive to NHC concentration in the reaction medium due to the excess phosphate ions. At a precursor Ca/P ratio of 5, calcium ions were in excess, and calcium carbonate was formed when NHC was introduced into the reaction medium. When the precursor Ca/P ratio was reduced to 3.33, up to 0.1 M NHC could be introduced into the reaction medium without forming a calcium carbonate phase. At a precursor Ca/P ratio of 1.67, the apatitic phase was stable at all NHC concentrations

examined. The Ca/P ratios of the resulting carbonated apatites were sensitive to the NHC concentrations in the reaction medium. For 0–0.3 M NHC, the increasing Ca/P ratio measured (Table 4.5) suggested successful carbonate substitution in the phosphate sites of the HAP structure. However, the sample synthesized with 0.9 M NHC has a lower Ca/P ratio than that obtained with no NHC, indicating that the former has a very different carbonate substitution behavior.

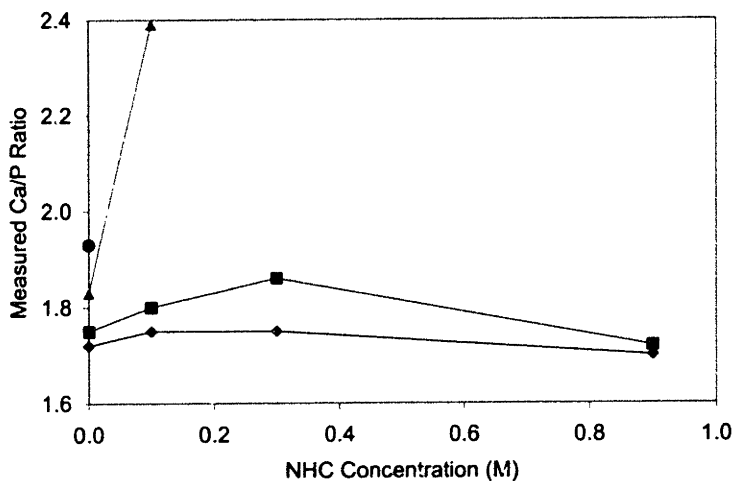


Figure 4.8. The effect of NHC concentration on the measured Ca/P ratio of carbonated apatites synthesized with a precursor Ca/P ratio of (◆) 1, (■) 1.67, (▲) 3.33 and (●) 5, and aged at 120°C for 100 hr. All samples were of an apatitic phase.

4.3.3. Effect of Ammonium Carbonate Concentration on Carbonate Substitution

Crystallinity of the carbonated apatite has been determined to affect the extent and site of carbonate substitution. It has been shown to increase with increasing aging time or temperature. This section examined the effect of NHC concentration in the reaction mixture on the extent and site of carbonate substitution. Figures 4.9(a)–(c) show apatites prepared with a precursor Ca/P ratio of 1.67 after aging at 25°C for for 24 hr. These materials were all poorly crystalline in nature regardless of the NHC concentrations used in the reaction medium. Highly crystalline apatites were prepared with a precursor Ca/P ratio of 1.67 by a hydrothermal treatment at 120°C for 100 hr (Figures 4.9(d)–(f)). In the absence of NHC, apatite formed elongated hexagonal crystals (Figure 4.9(d)). Figures 4.9(e) and (f) show spheroidal carbonated apatite nanocrystals, which decreased in size as the NHC concentration in the reaction mixture increased.

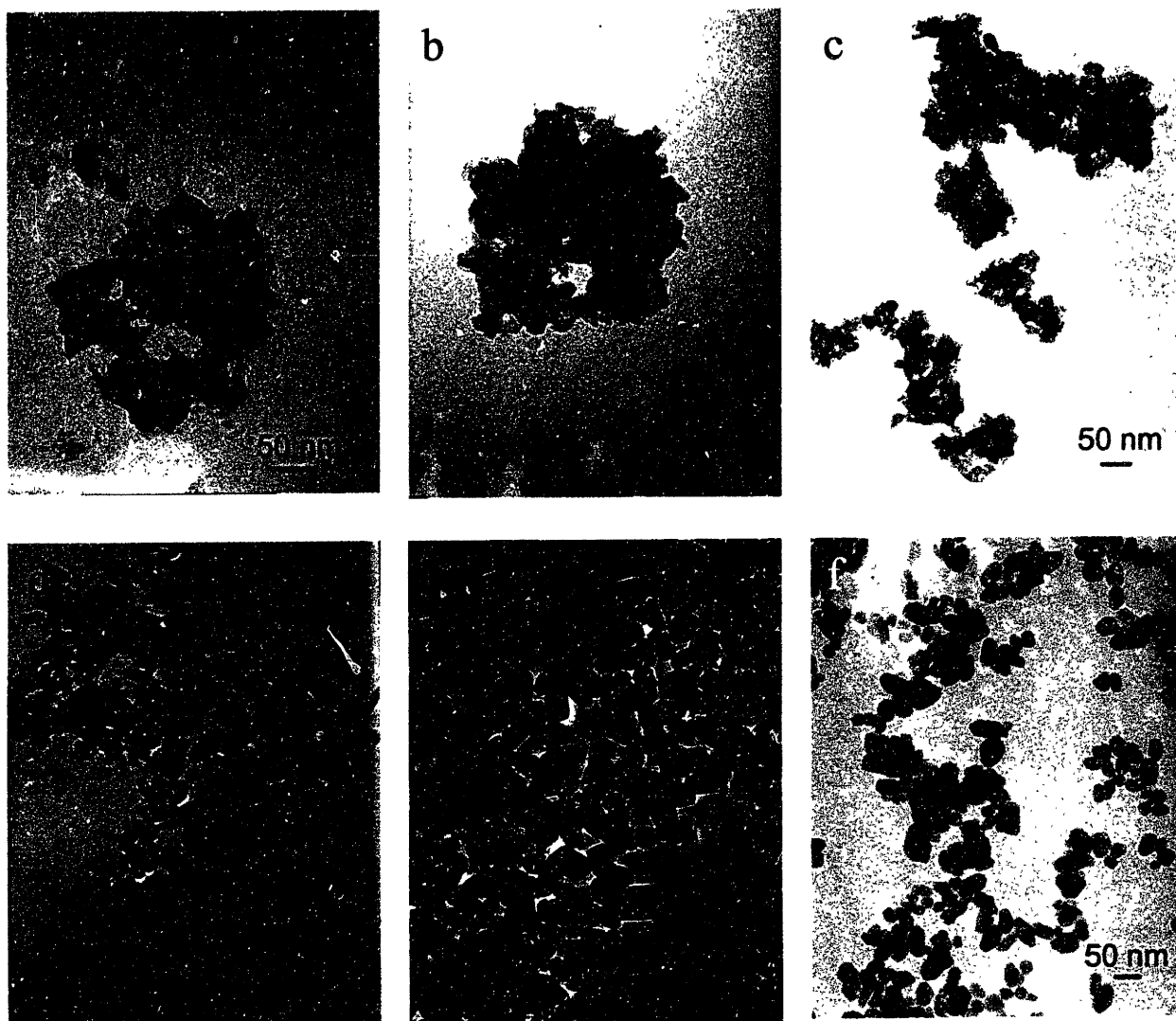


Figure 4.9. TEM micrographs of carbonated apatites prepared with a precursor Ca/P ratio of 1.67, and (a) 0, (b) 0.3 and (c) 2.0 M NHC with aging at 25°C for 24 hr, and (d) 0, (e) 0.3 and (f) 0.9 M NHC with hydrothermal aging at 120°C for 100 hr.

Infrared spectroscopy was used to examine the extent of apatite structural development and the site(s) of carbonate substitution. PA-FTIR spectrum of the poorly crystalline apatite synthesized in the absence of NHC showed that the microenvironment around the phosphate groups was not well-defined (Figure 4.10(a)). In a crystalline apatite, the ν_3 phosphate band is a triplet located at 1056, 1085 and 1096 cm^{-1} [15, 22]. However, only two peaks of the ν_3 band were resolved at 1056 and 1096 cm^{-1} in Figure 4.10(a), indicating the poor crystallinity of this sample derived from aging at 25°C for 24 hr. Furthermore, a phosphate ν_4 band would be present as a triplet at 566, 574, and 602 cm^{-1} for well-ordered apatites [22]. The spectrum in Figure 4.10(a) showed two strong peaks at 566 and 574 cm^{-1} , and a weak peak at 602 cm^{-1} . The

non-hydrogen-bonded hydroxyl peak associated with apatites was observed at 3560 cm^{-1} [15]. In addition, hydrogen-bonded water and hydroxyl species gave rise to a broad band at $2800\text{--}3600\text{ cm}^{-1}$. For poorly crystalline apatites formed with 0.3 and 2.0 M NHC, the ν_3 phosphate band appeared as a single intense band [22], the ν_4 band was poorly defined, and the sharp hydroxyl peak at 3560 cm^{-1} was absent in the PA-FTIR spectra (Figures 4.10(b) and (c)). Thus, the apatite crystallinity was further reduced with carbonation for samples synthesized at 25°C for 24 hr.

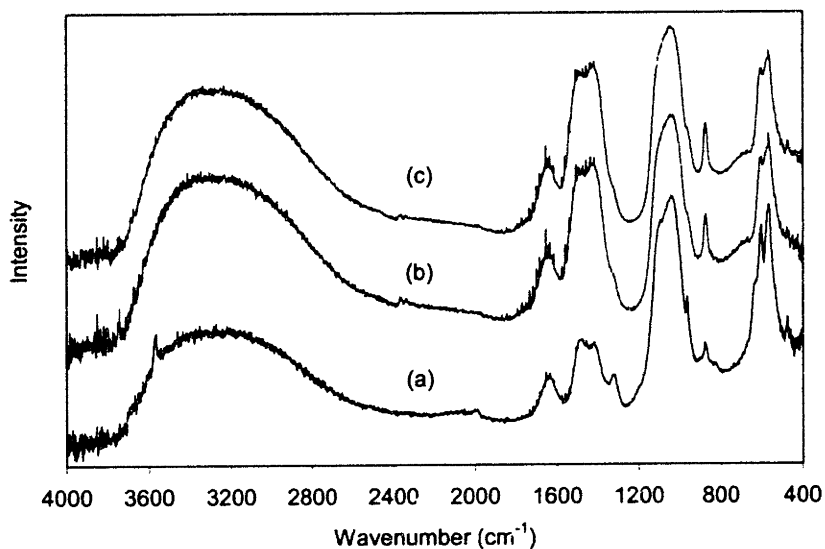


Figure 4.10. PA-FTIR spectra of poorly crystalline carbonated apatites synthesized with a precursor Ca/P ratio of 1.67 and (a) 0, (b) 0.3 and (c) 2.0 M NHC, with aging at 25°C for 24 hr.

In contrast, apatites prepared by hydrothermal treatment at 120°C for 100 hr possessed a well-developed structure (Figure 4.11). The highly crystalline apatite formed in the absence of NHC had a well-defined ν_3 phosphate band at $1056, 1085$ and 1096 cm^{-1} , a well-defined ν_4 phosphate band at $566, 574$ and 602 cm^{-1} , and a strong non-hydrogen bonded hydroxyl peak at 3560 cm^{-1} . As NHC was introduced into the reaction medium, ν_3 phosphate band became a single intense band, and the intensities of the ν_4 phosphate band at 602 cm^{-1} and the non-hydrogen-bonded hydroxyl peak at 3560 cm^{-1} were noticeably reduced. The significant loss in the hydroxyl peak intensity might be due to carbonate substitution into the hydroxyl sites, yielding some type A carbonated apatites.

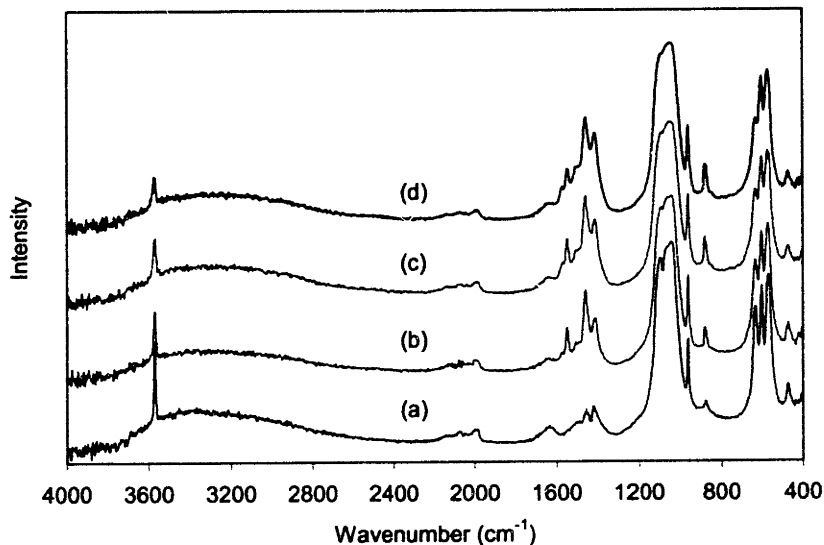


Figure 4.11. PA-FTIR spectra of highly crystalline carbonated apatites synthesized with a precursor Ca/P ratio of 1.67 and (a) 0, (b) 0.1, (c) 0.3 and (d) 0.9 M NHC, with aging at 120°C for 100 hr.

To determine if the carbonate species were substituting for the hydroxyl groups or phosphate groups in the apatitic structure, detailed analysis of the carbonate peaks was performed. Peaks in the regions of 873–875 cm^{-1} and 1300–1650 cm^{-1} are associated with the ν_2 and ν_3 vibrational modes of carbonate ions, respectively [15, 22]. The peaks at 873, 1415 and 1465 cm^{-1} have been assigned to carbonates substituted for the phosphate (type B) sites [14, 23-26]. The peaks at 880, 1450 and 1545 cm^{-1} have been attributed to carbonates substituted into the hydroxyl (type A) sites [14, 23-26].

Figure 4.12 shows that the poorly crystalline apatites derived from aging at 25°C for 24 hr possessed infrared peaks at 875, 1415 and 1465 cm^{-1} , indicating that the samples are of a type B carbonated apatite. For these samples, the carbonates appeared to substitute only for the phosphate sites in the apatitic structure, regardless of the NHC concentrations in the reaction medium.

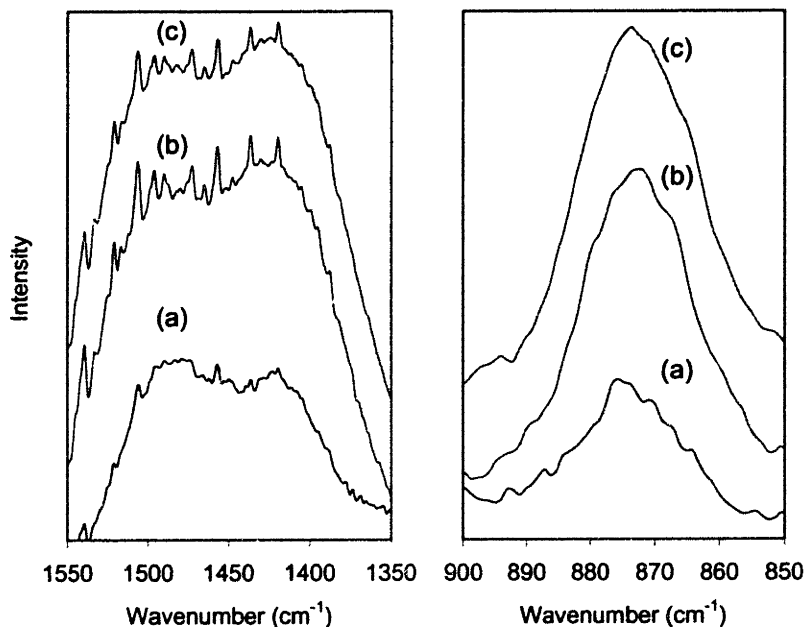


Figure 4.12. PA-FTIR spectra of poorly crystalline carbonated apatites synthesized with a precursor Ca/P ratio of 1.67 and (a) 0, (b) 0.3 and (c) 2.0 M NHC, with aging at 25°C for 24 hr.

Table 4.6. Chemical formulas of carbonated apatites prepared with a precursor Ca/P ratio of 1.67 and aged at 25°C for 24 hr.

| NHC Conc. (M) | Ca [†] (wt%) | P [†] (wt%) | C [‡] (wt%) | Proposed Chemical Formula |
|------------------|--------------------------|-------------------------|-------------------------|---|
| 0.0 | 37.7 | 16.5 | 0.5 | Ca _{9.7} (CO ₃) _{0.4} (PO ₄) _{5.5} (OH) ₂ |
| 0.3 | 42.1 | 17.6 | 1.9 | Ca _{9.5} (CO ₃) _{1.4} (PO ₄) _{5.2} (OH) _{0.7} |
| 2.0 | 39.6 | 14.2 | 2.9 | Ca _{8.9} (CO ₃) _{1.7} (PO ₄) _{4.1} (OH) ₂ |

[†] Derived from elemental analysis.

[‡] Derived from CHN analysis.

Thus, by processing carbonated apatites with a poorly developed crystal structure, substitution in the more desirable phosphate site could be attained. In Table 4.6, chemical formulas were proposed for the poorly crystalline carbonated apatites using results from elemental and CHN analyses, assuming that all carbonates were substituted in the phosphate (type B) sites and that the charge balance was maintained with the hydroxyl groups. For the carbonated apatite prepared in the absence of NHC, residual carbonates in the water were incorporated and substituted in the phosphate sites. The ~1:1 carbonate substitution for the phosphate group was in reasonable agreement with both equations 4.2 and 4.3. For the carbonated apatite prepared in the presence of 0.3 M NHC, carbonates were found to substitute

for phosphates at a molar ratio of $\sim 4:3$ based on the proposed chemical formula in Table 4.6, which agreed quite well with equation 4.4. For the carbonated apatite prepared in 2.0 M NHC, the proposed chemical formula showed an approximate 1:1 substitution of the carbonates for the phosphate groups, and was in fair agreement with equations 4.2 and 4.3.

The highly crystalline apatites synthesized by hydrothermal treatment at 120°C for 100 hr possessed more and sharper infrared peaks (Figure 4.13) than the poorly crystalline carbonated apatites. The peaks at 875 , 1415 and 1465 cm^{-1} were indicative of type B carbonate substitution, and those at 880 , 1450 and 1545 cm^{-1} were indicative of type A carbonate substitution. We note that for the sample prepared at 0 M NHC, the peaks observed corresponded to type B carbonate substitution. The materials produced with NHC in the reaction medium showed stronger carbonate peak intensities, indicating a greater degree of carbonation. They possessed infrared peaks that corresponded to both type A and type B carbonate substitution. In fact, the peak intensities were stronger for the former, suggesting that carbonates were substituted preferentially into the hydroxyl sites when NHC was used in producing the highly crystalline samples.

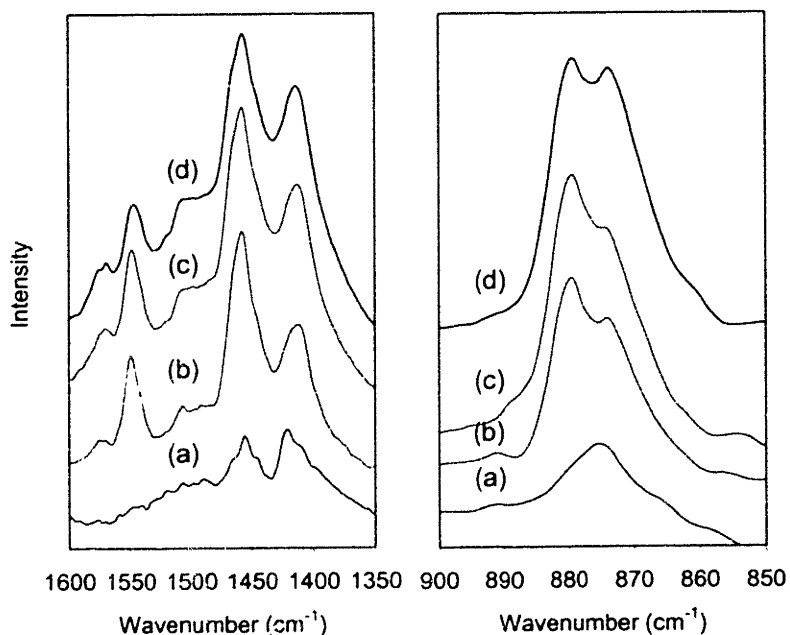


Figure 4.13. PA-FTIR spectra of highly crystalline carbonated apatites synthesized with a precursor Ca/P ratio of 1.67 and (a) 0, (b) 0.1 (c) 0.3 and (d) 0.9 M NHC, with aging at 120°C for 100 hr.

Since the poorly crystalline apatites do not have a well-defined structure, a large amount of carbonates could be incorporated into the apatitic structure without the loss of phase stability. Figure 4.14(a) showed that the poorly crystalline apatites synthesized with 0.1 and 2.0 M NHC lost ~15 and ~20 wt% when heated to 1000°C. Thus, TGA confirmed that more carbonates were incorporated in this system with increasing NHC concentrations. Furthermore, the stability of carbonate species could be determined from the TGA-MS analysis. Carbon dioxide evolved from sample treatments below 200°C might correspond to the removal of surface adsorbed carbonates. Carbon dioxide evolved from heat treatments at higher temperatures might be attributed to carbonates incorporated in the apatitic lattice at the hydroxyl and/or phosphate sites. Since carbonates were released from the apatitic lattice through a wide range of temperatures (Figure 4.14(b)), the carbonates were likely located at a variety of microenvironments within the apatite lattice. From this study, it was clear that significant amounts of carbonates (attributed to type B by PA-FTIR) were incorporated into the poorly crystalline apatites synthesized at 25°C for 24 hr. It was also noted that the use of NHC in the reaction medium significantly increased the carbonation level in this system.

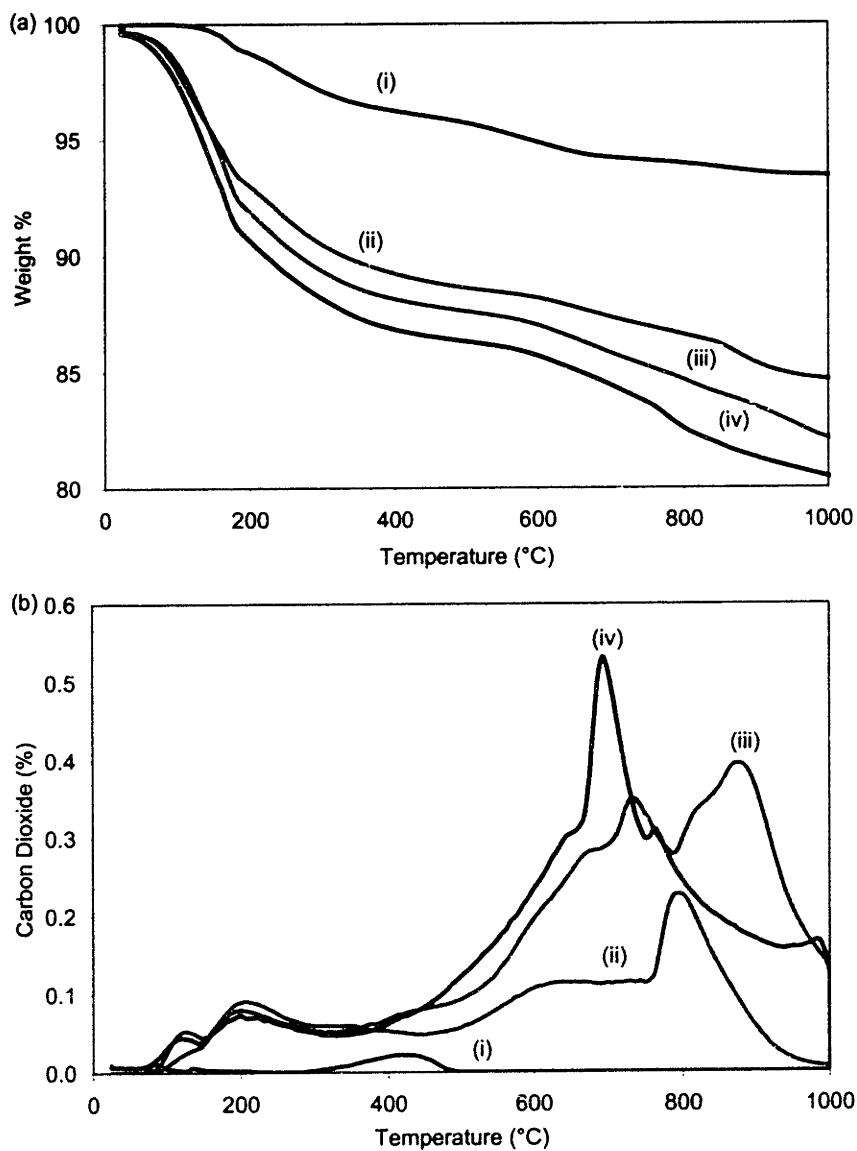


Figure 4.14. TGA-MS analysis showing (a) weight loss and (b) CO₂ concentration evolved during the heat treatment of poorly crystalline carbonated apatites synthesized with a precursor Ca/P ratio of 1.67 and (i) 0, (ii) 0.1, (iii) 0.3 and (iv) 2.0 M NHC with aging at 25°C for 24 hr.

For the samples produced hydrothermally at 120°C for 100 hr, higher crystallinity was achieved with a substantially lower amount of lattice incorporation of carbonates (Figure 4.15). When no NHC was present in the reaction medium, a small amount of carbonates (attributed to type B by PA-FTIR) was found in the sample (see Figure 4.13(a)). The presence of 0.3 M NHC in the reaction medium yielded a carbonated apatite that evolved carbonates at lower temperatures than the carbonated apatite prepared with 0.9 M NHC (Figure 4.15(a)). Furthermore, carbonates evolved from apatites prepared at 120°C occurred within a similar range of high temperatures, indicating that the carbonates were lattice incorporated rather than surface adsorbed species. With the use of increasing amounts of NHC, greater amounts of carbonates were incorporated at the lattice sites (see Figure 4.13). From total C analysis and amount of CO₂ evolved below 200°C (from surface adsorbed carbonates), we could estimate the amount of carbonates that were substituted into the apatitic lattice. This lattice carbonate amount could be further attributed to type A or type B carbonate through quantitative analysis of the PA-FTIR carbonate peaks located at 850–900 cm⁻¹ (Table 4.7). At NHC concentrations of 0.3 and 0.9 M, both type A and type B carbonate substitutions were observed. In the absence of NHC, only type B carbonate substitution was noted in the PA-FTIR spectrum.

Table 4.7. Quantitative analysis of PA-FTIR carbonate peak areas located at 850–900 cm⁻¹ for carbonated apatites prepared with a precursor Ca/P ratio of 1.67 and aged at 120°C for 100 hr.

| NHC (M) | Peak Area (%) | | Total CO ₃ ²⁻ * (wt%) | Type A Carbonate (wt%) | Type B Carbonate (wt%) |
|------------|----------------------|----------------------|--|---------------------------|---------------------------|
| | 880 cm ⁻¹ | 875 cm ⁻¹ | | | |
| 0 | 0 | 100 | 0.8 | - | 1.6 |
| 0.3 | 43 | 57 | 1.8 | 0.86 | 1.14 |
| 0.9 | 23 | 77 | 4.7 | 0.81 | 2.70 |

* Measured by CHN analysis

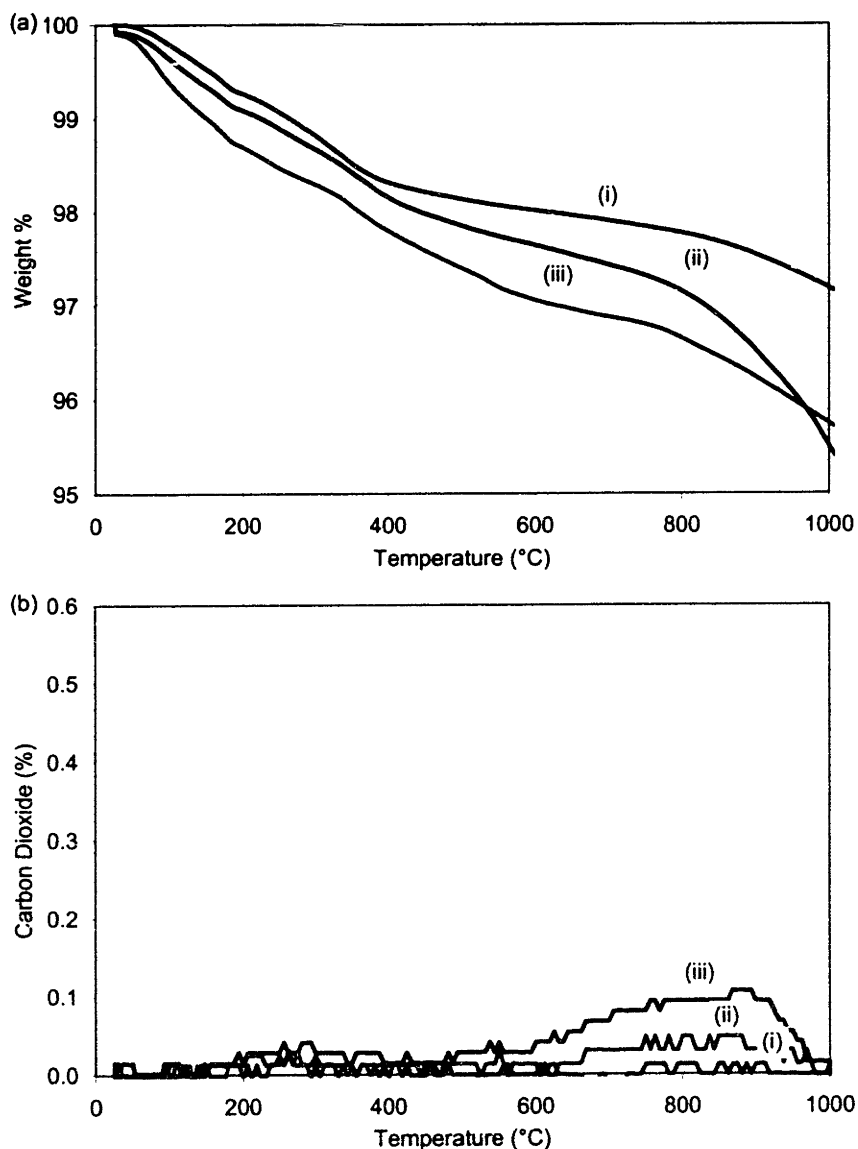


Figure 4.15. TGA-MS analysis showing (a) weight loss and (b) CO₂ concentration evolved during the heat treatment of highly crystalline carbonated apatites synthesized with a precursor Ca/P ratio of 1.67 and (i) 0, (ii) 0.1 and (iii) 0.9 M NHC, with aging at 120°C for 100 hr.

4.4. Conclusions

While the composition and structure of carbonated apatites depended on the preparation conditions, such as the precursor Ca/P ratio and the NHC concentration in the reaction medium, aging time and temperature strongly influenced the site and extent of carbonate substitution by dictating the crystallinity of the carbonated apatite. Poorly crystalline apatite systems could incorporate large amount of carbonates substituted at the phosphate sites. Highly crystalline

carbonated apatites, on the other hand, were less tolerant of carbonate substitution. They could only incorporate a small amount of carbonates into their well-defined crystal structure, which possessed a near-stoichiometric Ca/P ratio. Thus, nanostructure processing provided a means of controlling the structural characteristics of carbonated apatites at the molecular level. Poorly crystalline apatites with a high level of type B carbonate substitution might act as synthetic bone minerals with high resorption rates for future implant applications.

4.5. References

- [1] J. C. Merry, I. R. Gibson, S. M. Best, W. Bobfield, *J. Mater. Sci. Mater. Med.* **9**, 779 (1998).
- [2] E. F. Morgan, D. N. Yetkinler, B. R. Constantz, R. H. Dauskardt, *J. Mater. Sci. Mater. Med.* **8**, 559 (1997).
- [3] G. Vaes, *Clin. Orthopaed. Rel. Res.* **231**, 239 (1988).
- [4] R. Pacifici, *et al.*, *J. Clin. Invest.* **87**, 221 (1991).
- [5] J. Glowacki, C. Rey, M. J. Glimcher, K. A. Cox, J. Lian, *J. Cell. Biochem.* **45**, 292 (1991).
- [6] I. C. Ison, M. T. Fulmer, B. M. Barr, B. R. Constantz, in *Hydroxyapatite and Related Materials*, P. W. Brown, P. Wenzil, B. Constantz, Eds. (CRC Press, Boca Raton, 1994), p. 215.
- [7] K. A. Hing, *et al.*, *Bioceram.* **10**, 19 (1997).
- [8] L. G. Ellies, J. M. Carter, R. J. Natiela, J. D. B. Featherstone, D. G. A. Nelson, *J. Biomed. Mater. Res.* **42**, 137 (1988).
- [9] Y. Doi, T. Shibusani, Y. Moriwaki, T. Kajimoto, Y. Iwayama, *J. Biomed. Mater. Res.* **39**, 603 (1998).
- [10] J. C. Elliot, *Studies in Inorganic Chemistry 18: Structure and Chemistry of the Apatites and Other Calcium Orthophosphates* (Elsevier Science, New York, 1994).
- [11] D. E. C. Corbridge, *Studies in Inorganic Chemistry 10: Phosphorous, An Outline of Its Chemistry, Biochemistry, and Technology* (Elsevier Science, New York, 1990).
- [12] A. Slosarczyk, E. Stobierska, Z. Pazkiewicz, M. Gawlicki, *J. Am. Ceram. Soc.* **79**, 2539 (1996).

- [13] M. T. Fulmer, R. I. Martin, P. W. Brown, *J. Mater. Sci. Mater. Med.* **79**, 2539 (1992).
- [14] M. Vignoles, G. Bonel, D. W. Holcomb, R. A. Young, *Calcif. Tiss. Int.* **43**, 33 (1988).
- [15] D. G. A. Nelson, J. D. B. Featherstone, *Calcif. Tiss. Int.* **34**, 569 (1982).
- [16] Y. Doi, *et al.*, *J. Biomed. Mater. Res.* **29**, 1451 (1995).
- [17] A. L. Boskey, A. S. Posner, *J. Phys. Chem.* **77**, 2313 (1973).
- [18] E. D. Eanes, I. H. Gillessen, A. S. Posner, *Nature* **208**, 365 (1965).
- [19] E. D. Eanes, A. S. Posner, *Trans. N. Y. Acad. Sci.* **28**, 233 (1965).
- [20] E. D. Eanes, J. L. Meyer, *Calcif. Tiss. Res.* **23**, 259 (1977).
- [21] J. D. Termine, R. A. Peckauskas, A. S. Posner, *Arch. Biochem. Biophys.* **140**, 318 (1970).
- [22] I. Rehman, W. Bonfield, *J. Mater. Sci. Mater. Med.* **8**, 1 (1997).
- [23] F. Apfelbaum, H. Diab, I. Mayer, J. D. B. Featherstone, *J. Inorg. Biochem.* **45**, 277 (1992).
- [24] C. Rey, V. Renugopalakrishnan, B. Collins, M. J. Glimcher, *Calcif. Tiss. Int.* **49**, 251 (1991).
- [25] S. Shinoda, T. Aoba, E. C. Moreno, Y. Miake, *J. Dent. Res.* **69**, 1731 (1990).
- [26] L. Kuhn-Spearing, C. Rey, H. M. Kim, M. J. Glimcher, Carbonated Apatite Nanocrystals from Bone, TMS Annual Meeting (1996).

Chapter 5 – Recommendations for Future Work

In this thesis, nanostructured apatites were developed as orthopedic biomaterials. By applying nanostructure processing to the precipitation of apatites, the chemical stability and thermal stability were varied by controlling the composition and crystallinity of the precipitate. When consolidated, highly crystalline and thermally stable hydroxyapatite nanocrystals yielded mechanically strong and bioactive monoliths. While the *in vitro* attachment, adhesion, proliferation and mineralization assays applied in this thesis can be used to screen orthopedic biomaterials for bone bonding, sample size and number are inherent limitations associated with these approaches. As a result, standard biochemical assays that can quantify cell number, collagen synthesis, proteoglycan synthesis, or protein expression cannot be used. Consequently, evaluation of the osteoblast-material interaction is limited to analytical techniques using microscopy. Since the mechanical and *in vitro* testing of nanocrystalline hydroxyapatite monoliths yielded positive results, it would be worthwhile to devote further efforts on this research to investigate the detailed bone-bonding behavior of nanocrystalline hydroxyapatite in an animal model.

This thesis has successfully created an interesting class of nanostructured carbonated apatites that have potential applications as a resorbable implant material. Nanostructure processing of carbonated apatites was shown to dictate the extent and site of carbonate substitution into the apatitic lattice. By controlling the composition and crystallinity of carbonated apatites, the rate of resorption can be tuned for resorbable implant applications. Future research may be directed towards developing an *in vitro* resorption assay using osteoclasts to determine the relationship between osteoclast-mediated resorption and the crystal structure of nanostructured carbonated apatites.

Ceramic-ceramic and ceramic-metal nanocomposites were also successfully developed to improve the mechanical properties of nanocrystalline hydroxyapatite monoliths. For the most demanding orthopedic applications such as total joint replacement, orthopedic biomaterials need to be established with higher fracture toughness and a lower elastic modulus. Future research on hydroxyapatite-polymer nanocomposites can potentially satisfy these requirements for mechanical strength. In addition to increased toughness, polymer systems can be used to actively stimulate osteoblast. Future research may be devoted to the development of magnetic

field sensitive hydrogel systems to stimulate osteoblast mineralization. An applied magnetic field would cause the hydrogel to deform, transmitting mechanical strain to osteoblasts attached to the surface. This would stimulate the osteoblasts to synthesize extracellular matrix to stiffen the hydrogel. Such a magnetic field sensitive hydrogel biomaterial could be implanted where the localized induced strain would accelerate the healing process.

Chapter 6 – Conclusions

As the nanostructure processing of chemically precipitated apatitic systems allows for materials design from the molecular level, it offers great flexibility in controlling characteristics such as stoichiometry, composition, crystallinity, particle morphology, and grain size. In this thesis, the properties of the four different apatite-based systems were investigated and tailored in chemical and thermal stability for load-bearing and resorbable orthopedic implant applications.

Processing conditions were optimized to yield hydroxyapatite nanocrystals with superior phase purity and chemical homogeneity so that excellent thermal stability and sinterability were attained. The optimized process yielded a fully dense, transparent, nanocrystalline hydroxyapatite bioceramic that exhibited superb mechanical properties and *in vitro* mineralization. The excellent mechanical strengths of nanocrystalline hydroxyapatite were attributed to its ultrafine microstructure and phase purity. The high grain boundary volume fraction associated with nanocrystalline hydroxyapatite also gave rise to enhanced osteoblast attachment, proliferation and mineralization compared to polycrystalline hydroxyapatite.

To further increase the strength of the hydroxyapatite systems, zirconia and silver were introduced as a secondary reinforcing phase. Nanostructure processing allowed for the intimate mixing between hydroxyapatite nanocrystals and the additives. These highly dispersed nanocomposites were successfully densified to yield uniform, ultrafine microstructures with excellent mechanical reinforcement.

Lastly, nanostructure processing was successfully utilized to alter the apatite crystal structure to more closely resemble bone mineral. The carbonated apatite nanocrystals should lead to enhanced resorption through the judicious control of the site and extent of carbonate substitution during materials processing.

THESIS PROCESSING SLIP

FIXED FIELD: ill. _____ name _____

index _____ biblio _____

► COPIES: Archives Aero Dewey ~~Baker~~ Hum
Lindgren Music Rotch Science Sche-Plough

TITLE VARIES: ► _____

NAME VARIES: ► _____

IMPRINT: (COPYRIGHT) _____

► COLLATION: _____

► ADD: DEGREE: _____ ► DEPT.: _____

► ADD: DEGREE: _____ ► DEPT.: _____

SUPERVISORS: _____

NOTES:

cat'r:

date:

page:

► DEPT: _____

► YEAR: _____ ► DEGREE: _____

► NAME: _____